



저작자표시-비영리-변경금지 2.0 대한민국

이용자는 아래의 조건을 따르는 경우에 한하여 자유롭게

- 이 저작물을 복제, 배포, 전송, 전시, 공연 및 방송할 수 있습니다.

다음과 같은 조건을 따라야 합니다:



저작자표시. 귀하는 원저작자를 표시하여야 합니다.



비영리. 귀하는 이 저작물을 영리 목적으로 이용할 수 없습니다.



변경금지. 귀하는 이 저작물을 개작, 변형 또는 가공할 수 없습니다.

- 귀하는, 이 저작물의 재이용이나 배포의 경우, 이 저작물에 적용된 이용허락조건을 명확하게 나타내어야 합니다.
- 저작권자로부터 별도의 허가를 받으면 이러한 조건들은 적용되지 않습니다.

저작권법에 따른 이용자의 권리는 위의 내용에 의하여 영향을 받지 않습니다.

이것은 [이용허락규약\(Legal Code\)](#)을 이해하기 쉽게 요약한 것입니다.

[Disclaimer](#)

공학박사 학위논문

**Exciplex Dynamics and
Emitting Dipole Orientation of
Organic Light-Emitting Diodes**

유기발광소자의 엑시플렉스 동역학과
발광 쌍극자 배향 연구

2016년 8월

서울대학교 대학원
재료공학부 하이브리드재료 전공
김 권 현

Abstract

Exciplex Dynamics and Emitting Dipole Orientation of Organic Light-Emitting Diodes

Kwon-Hyeon Kim

Department of Materials Science and Engineering

The Graduate School

Seoul National University

Organic light-emitting diodes (OLEDs) are particularly promising organic semiconductor devices for applications in lighting and displays. However, OLEDs exhibit lower power efficiencies than other light sources. Recently reported external quantum efficiencies (EQEs) of 29–30% for phosphorescent OLEDs (PhOLEDs) are close to the theoretical limit for isotropically oriented iridium complexes. The preferred orientation of the transition dipole moments has not been considered for PhOLEDs because of the lack of an apparent driving force for the molecular arrangement, even though horizontally oriented transition dipoles can result in efficiencies of > 30%. The origin of preferred orientation of the emitting dipoles of Ir complexes, and the design of a horizontal orientation for the emitting dipoles of

the Ir complexes has not been studied in detail. Furthermore, EQEs in excess of 30% for horizontal emitting dipoles have not previously been reported.

Recent investigations of triplet harvesting in pure organic phosphors via reverse intersystem crossing (RISC) have used charge-transfer complexes. Intramolecular charge transfer complexes reduce the energy gap between singlet and triplet states, ΔE_{ST} , resulting in more efficient triplet harvesting, as well as an internal quantum efficiency (IQE) of almost 100%, and an EQE of 30%. The excited state intermolecular charge transfer complex (or exciplex) can result in very small values of ΔE_{ST} , and highly efficient triplet harvesting via RISC. However, fluorescent OLEDs (FOLEDs) using exciplex emission still exhibit lower efficiencies than FOLEDs based on single molecule thermally activated delayed fluorescent (TADF) emitters; furthermore, there are no clear strategies for improving the efficiency of FOLEDs using exciplex emission.

This thesis concerns two research topics: (1) exciplex dynamics for efficient triplet harvesting of FOLEDs, and (2) the emitting dipole orientation of phosphors for PhOLEDs. Our analysis shows that we could achieve unprecedented efficiency for both fluorescent and PhOLEDs.

In Chapter 2, the exciplex dynamics that determine the IQE of FOLEDs are analyzed quantitatively using temperature-dependent transient photoluminescence (PL) and electroluminescence (EL) measurements. To date, most researchers have concentrated on reducing ΔE_{ST} to obtain high RISC rates, resulting in efficient triplet harvesting; however, this study shows that a high RISC rate does not necessarily lead

to efficient triplet harvesting in exciplex emitters if there is a high non-radiative transition rate (k_{nr}). Not only efficient RISC, but also low non-radiative losses in both singlet and triplet exciplex emitters is required for efficient triplet harvesting. Triplet harvesting from exciplex emission can be increased by using exciplex emitters with a low k_{nr} ; furthermore, suppressing k_{nr} by cooling the exciplex can result in an IQE of 100%. As a result, FOLEDs using exciplex emission were achieved that exhibited an IQE of 100% and an EQE of 25.2% at 150 K; this compares with an IQE of 48.3% and an EQE of 11.0% at room temperature, and is due to a reduction in the non-radiative transition rate.

TADF and exciplex-based FOLEDs have disadvantages compared with conventional FOLEDs in terms of the broad emission spectra and low device stability. In **Chapter 3**, rather than using exciplex emission, an exciplex system was used as a host for a conventional fluorescent dopant without delayed fluorescence. By exploiting the narrow emission spectra and stability of fluorescent molecules, we use exciplex triplet harvesting via the Förster energy transfer mechanism from the exciplex to the conventional fluorescent dopant. As a result, red FOLED with conventional fluorescent dopant was obtained with an unprecedented EQE of 10.6%. A fraction of radiative excitons greater than 35% was achieved using the exciplex host, which is clearly indicative of triplet harvesting in the system.

In **Chapters 4–8**, we discuss the emitting dipole orientation of the phosphorescent emitter for highly efficient PhOLEDs. Origin of the preferred orientation of phosphorescent emitting dipoles and relationships between the

molecular structures of the phosphorescent emitter and the orientation of the emitting dipoles are discussed. OLEDs with unprecedented efficiencies are demonstrated using horizontally emitting dipoles. The orientation of the emitting dipoles of Ir complexes is influenced significantly by the ancillary ligand (**Chapter 4**) and the main ligand of the Ir complex (**Chapter 5**). Homoleptic Ir complexes exhibit almost isotropic orientation of the emitting dipoles; by contrast, heteroleptic Ir complexes (HICs) exhibit preferred orientations of emitting dipoles, despite their globular shape. The preferred orientation of the emitting dipole moments of HICs in amorphous host films results from the preferred direction of the triplet transition dipole moments of the HICs and the strong supramolecular arrangement within the co-host environment. This study shows that the C_2 axis of HICs preferentially aligns normal to the substrate with some distribution and triplet transition dipole moments in the HICs direct from Ir to *N*-heterocycles. This results in horizontally emitting dipoles of HICs in the amorphous emitting layer. Furthermore, OLEDs with an EQE of 35.6% (red HICs) and 32.3% (green HICs) are demonstrated, with phosphorescent transition dipole moments oriented in the horizontal (in-plane) direction (**Chapters 4 and 5**).

Based on these observations, HICs with a high fraction of horizontally oriented dipoles (Θ) were designed and synthesized by substituting the main ligand of the HICs. This design strategy includes two strategies: the substituents induce (1) triplet transition dipole moments in HICs located normal to the C_2 axis of HICs (**Chapter 6**), and (2) the doubly degenerated transition dipole moments are parallel to the substrate (**Chapter 7**). Cyclometalated ligands of HICs were systematically substituted by methyl groups to control the direction of transition dipole moments of

HICs. This methyl substitution resulted in different directions of the transition dipole moments in the iridium complexes, giving molecules with larger angles between the C_2 axis and the transition dipole moments (Φ) in the molecules, resulting in a larger Θ in the emitting layer. As a consequence, a bis(2-(3,5-dimethylphenyl)-4-methylpyridine) Ir (III) (2,2,6,6-tetramethylheptane-3,5-diketonate) ($Ir(3',5',4\text{-mppy})_2\text{tmd}$) with a high Θ of 80% (which is 6% higher than that of HICs without methyl substituents) was developed, and green OLEDs exhibiting a high EQE of 34.1% were demonstrated using the new emitter (**Chapter 6**).

In **Chapter 7**, various functional groups were substituted on the 4-position of the pyridine ring of the HICs to align Ir-N bonds of HICs and transition dipole moments parallel to the substrate. These HICs exhibited Θ in the range 80–86.5%, which is 1–7.5% greater than that of the reference HIC ($Ir(3',5',4\text{-mppy})_2\text{tmd}$), coming from different molecular orientation in the emitting layer. Consequently, we demonstrated unprecedented high EQE of 38% for yellow OLED and 36% for green OLED with new HICs in iridium-based PhOLEDs.

An amorphous emission layer can have orientational ordering, as with a liquid crystal; however, the orientation of molecules exhibits some distribution around an average orientation. Thus, it will be difficult to increase Θ due to the amorphous nature of typical emitting layers. In this regard, organic crystals would be the better emitters because of the orientational and positional ordering; however, organic crystals have been rarely used in OLEDs due to low PL quantum yield that results from concentration quenching, and the low device stability that results from the

rough surface. In **Chapter 8**, an unprecedented Θ of 93% and an EQE of 39% were realized for red OLEDs using a crystalline emission layer with perfectly oriented platinum complexes. The relationship between the orientation of the emitting dipole and the crystalline properties of the undoped Pt complex thin film are discussed based on grazing incident wide angle X-ray diffraction analysis and quantum chemical calculations. The orientation of the emitting dipole of the crystalline emission layers was affected not only by the crystallinity of the layer, but also by the molecular arrangement of the crystal, which are both influenced by the symmetry and position of the CF₃-substituted pyrazolate units in Pt complexes.

Keywords: Organic light-emitting diodes, exciplex, delayed fluorescence, triplet harvesting, emitting dipole orientation, crystalline emitting layer, iridium complex, platinum complex

Student Number: 2011 - 20621

Contents

Abstract	i
Contents	vii
List of Tables	xi
List of Figures	xiii
Chapter 1. Introduction	1
1.1. Brief history of organic light-emitting diodes	1
1.2. Efficiency of OLEDs	5
1.3. Emitting dipole orientation of OLEDs	6
1.3.1. Effects of emitting dipole orientation	6
1.3.2. Analysis of the emitting (or transition) dipole orientation.....	9
1.4. Exciplex OLEDs.....	15
1.5. Outline of the thesis.....	18
Chapter 2. Boosting triplet harvest by reducing non-radiative transition of exciplex toward fluorescent organic light-emitting diodes with 100% internal quantum efficiency.....	21
2.1. Introduction	21
2.2. Experimental.....	23
2.3. Result and discussion	24

2.4. Conclusion.....	38
----------------------	----

Chapter 3. Triplet harvesting by a conventional fluorescent emitter using reverse intersystem crossing of host triplet exciplex39

3.1. Introduction	39
3.2. Experimental.....	42
3.3. Result and discussion	44
3.4. Conclusion.....	53

Chapter 4. Highly efficient organic light-emitting diodes with phosphorescent emitters having high quantum yield and horizontal orientation of transition dipole moments54

4.1. Introduction	54
4.2. Experimental.....	55
4.3. Result and discussion	57
4.4. Conclusion.....	67

Chapter 5. Phosphorescent dye-based supramolecules for high-efficiency organic light-emitting diodes68

5.1. Introduction	68
5.2. Experimental.....	70
5.3. Result and discussion	75
5.3.1. Materials for OLEDs	75
5.3.2. Orientations of transition dipole moments of the phosphorescent dyes	77
5.3.3. Fabrication and performance of the OLEDs.....	89
5.3.4. Optical simulation of the EQE of devices	92
5.4. Conclusion.....	98

Chapter 6. Controlling emitting dipole orientation with methyl substituents on main ligand of iridium complexes for highly efficient phosphorescent organic light-emitting diodes 99

6.1. Introduction	99
6.2. Experimental.....	102
6.3. Result and discussion	104
6.4. Conclusion.....	118

Chapter 7. Design of heteroleptic Ir complex with horizontal emitting dipoles for organic light-emitting diodes 119

7.1. Introduction	119
7.2. Experimental.....	122

7.3. Result and discussion	125
7.4. Conclusion.....	138
Chapter 8. Crystal organic light-emitting diodes with perfectly oriented non-doped Pt-based emitting layer	139
8.1. Introduction	139
8.2. Experimental.....	143
8.3. Result and discussion	146
8.4. Conclusion.....	171
Chapter 9. Summary and Outlook	172
Bibliography	176
초록	188
CURRICULUM VITAE	194
List of Publications.....	197
List of Presentations.....	202
List of Patents	216

List of Tables

Table 2.1 k_r^S , k_p , k_d , k_{ISC} , k_{RISC} , k_{nr}^S , k_{nr}^T at various temperatures. The unit of transition rates is s^{-1}	31
Table 4.1 Photoluminescence quantum yield and horizontal portion of transition dipole moments of three different phosphorescent dyes, and experimentally obtained EQEs of the OLEDs doped with three different phosphorescent dyes compared with the calculated EQEs using the classical dipole model under the assumption of perfect electron and hole balance in the devices.....	66
Table 5.1 Dipole moment ($M_\alpha(T^k)$) of the S_0 - T_1 transition for the T_1 geometry. A represents the direction of the transition dipole moment and k represents the Cartesian component of the ZFS triplet state spin sublevel. All values of the dipole moments are in a.u.	82
Table 5.2 Pairwise binding energies of the hosts (NPB, B3PYMPM) and the red dyes ($Ir(phq)_3$, $Ir(mphq)_2acac$, $Ir(MDQ)_2acac$, $Ir(mphmq)_2tmd$). All binding energies are in kcal/mol).	86
Table 6.1 Photophysical and electronic properties of the iridium complexes.	107
Table 6.2 Photophysical properties of iridium complexes and the device performances fabricated using the dyes.	117
Table 7.1 Photophysical properties and DFT results of Ir complexes.	128
Table 7.2 Calculated triplet transition properties of HICs using TD-DFT calculations to consider spin-orbit coupling.....	129
Table 7.3 Photophysical and electronic properties of HICs.....	133

Table 8.1 Crystal Data of single crystal and thin film for Pt(fppz) ₂ , Pt(f2bipz)(bpy) and Pt(fppz)(pic).	153
Table 8.2 Energy levels of HOMO and LUMO for Pt(fppz) ₂ , Pt(f2bipz)(bpy) and Pt(fppz)(pic).	166

List of Figures

Figure 1.1 Applications of OLEDs as flexible display (upper left; Samsung Electronics 2016), car back lighting (upper right; Audi 2013), OLED lighting (lower left; Philips), OLED TV (lower right; LG Electronics 2016).....	2
Figure 1.2 (a) Contour plot of theoretically maximum achievable EQE of green OLED as functions of thickness of organic layer and ITO layer assuming that the emitting dipole orientation is isotropic ¹¹ (b) Optimized geometry of Ir(ppy) ₃ at T ₁ geometry calculating from DFT calculation.	7
Figure 1.3 Contour plot of theoretically maximum achievable EQE of green OLED as functions of PL quantum yields and the ratio of horizontal dipoles of emitter. ⁷	8
Figure 1.4 Schematic description of variable angle spectroscopic ellipsometry (VASE). ^{16,22}	10
Figure 1.5 Schematic description of angle dependent PL spectra measurement setup. ²³	11
Figure 1.6 Calculated and measured exciton decay rate of dipoles as function of space thickness for (a) Ir(MDQ) ₂ acac and (b) Ir(ppy) ₃ . ²⁰	14
Figure 1.7 Potential energy diagram of the exciplex formation.	16
Figure 2.1 (a) Chemical structures and energy levels of TCTA and B4PYMPM. (b) PL spectra of TCTA, B4PYMPM, and TCTA:B4PYMPM.....	25
Figure 2.2 Time resolved PL spectra of the TCTA:B4PYMPM film at various times after excitation at (a) 300 K and (b) 50 K.	26

Figure 2.3 (a) Transient PL decay patterns of the TCTA:B4PYMPM film at various temperatures within long time range (0 – 450 μ s) (inset: normalized transient PL decay of the TCTA:B4PYMPM film at various temperatures within short time range (0 – 200 ns)). The transient PL intensities were obtained from the integration of the emission spectra from the wavelength of 350 nm to 750 nm. (b) Temperature dependence of PLQY for total (black square), prompt (red circle), and delayed (blue triangle) components of the TCTA:B4PYMPM exciplex..... 27

Figure 2.4 (a) The exciplex dynamics of the singlet and triplet has been analyzed based on the energy diagram and transition rates. (b) k_p , k_d , k_{ISC} , k_{RISC} , k_{nr}^S , and k_{nr}^T at various temperatures. (c) Arrhenius plot of the RISC rate in TCTA:B4PYMPM exciplex systems. The activation energy of the RISC rate is found to be 8.5 meV..... 29

Figure 2.5 (a) The J - V - L curves of the OLED at various temperatures. Solid scatter indicates current density and open scatter indicates luminance. (b) EL spectra of OLED with 0.1 mA/cm² at various temperatures. (c) The EQEs and CEs against current density at various temperatures. (d) Measured EQEs and theoretical EQEs at various temperatures. Outcoupling efficiencies of OLED were calculated with optical simulation based on the measured the ratio of horizontal emitting dipoles (61%), under the assumption of no electrical loss..... 34

Figure 2.6 PL spectra of TCTA:B4PYMPM 30 nm thick film at various temperature. 35

Figure 2.7 Φ_{RISC} and IQE against temperature. IQE was obtained with experimentally observable values using the Equation (2.7)..... 37

Figure 3.1 (a) Chemical structures of host and red fluorescent dopant and (b) PL spectra of TCTA, B4PYMPM, and TCTA:B4PYMPM at 295 K and delayed PL spectrum of TCTA:B4PYMPM after 10 μ s at 30 K. (c) Absorption spectra of TCTA, B4PYMPM, and mixed TCTA:B4PYMPM films. The absorption spectrum of the mixed TCTA:B4PYMPM film is the same as the weighted addition of the TCTA and B4PYMPM absorption spectra. (d) The molar extinction coefficient of the DCJTB and normalized PL spectra of TCTA:B4PYMPM film, exhibiting large spectral overlap between them..... 45

Figure 3.2 (a) Normalized intensity of transient PL of TCTA: B4PYMPM: 0.5 wt% DCJTB film and Alq₃:0.5 wt% DCJTB film (inset: PL spectrum of 0.5 wt% DCJTB doped in exciplex host). (b) Angle dependent PL intensity of the p-polarized light from the 30 nm thick TCTA: B4PYMPM: 0.5 wt% DCJTB film at 600 nm. (c) Top view of TDM on optimized structure of DCJTB. (d) Side view of TDM on optimized structure of DCJTB. 47

Figure 3.3 (a) The J - V - L curves of the OLEDs. (b) The normalized EL spectra of devices at 10 mA/cm². (c) The current efficiencies and power efficiencies against current density. (d) The EQEs against current density..... 49

Figure 3.4 (a) Transient EL intensity of device at various current level. The wavelength of detection is 605 nm. The voltage pulse width was 100 μ s, and the pulse was periodically applied to the devices with a frequency of 100 Hz. (b) Initial intensity of delayed emission against current density..... 52

Figure 4.1 Molecular structure of green phosphorescent dyes and (b) schematic diagram of the device structure and energy levels (eV) of the devices..... 58

Figure 4.2 (a) The PL spectra of the 8.4 mol% Ir(ppy)₃, Ir(ppy)₂acac, and Ir(ppy)₂tmd doped TCTA:B3PYMPM films. (b) Angle-dependent PL intensities of the p-polarized light from the 30-nm-thick films composed of TCTA:B3PYMPM:green dyes (0.46:0.46:0.08 molar ratio) at 520 nm. Solid lines represent theoretical fits to the experimental data..... 59

Figure 4.3 PL quantum yields at doping concentrations of 2, 4.2, and 8.4 mol % of dyes in TCTA:B3PYMPM (1:1) co-host..... 61

Figure 4.4 (a) The current density–voltage–luminance curves of the OLEDs. Inset: The angular distributions of the EL intensity of the OLEDs. The dashed line in the inset shows the Lambertian distribution. (b) The normalized EL spectra of the OLEDs. (c) Luminous efficiencies and power efficiencies against the luminance. (d) EQE’s against the luminance. The EQE’s and the power efficiencies of the devices were calibrated using the angle-dependent emission intensity profiles..... 63

Figure 5.1 Material characteristics. (a) Molecular structures of the red phosphorescent dyes and the host molecules. (b) Normalized PL spectra of the NPB, B3PYMPM and mixed NPB:B3PYMPM films..... 76

Figure 5.2 Analysis of the orientations of the transition dipole moments. (a) Angle-dependent PL intensities at 605nm and (b) angle-dependent PL spectra of p-polarized light from the 30-nm-thick NPB:B3PYMPM:red dye (0.5:0.5:0.035 molar ratio) film. The theoretical calculations fit the experimental data well. Potential energy diagram of the exciplex formation. 78

Figure 5.3 Quantum chemical calculations of the red dyes based on DFT. (a) Frontier molecular orbitals contributing to the lowest triplet transitions of Ir(phq)₃,

Ir(mphq)₂acac, Ir(MDQ)₂acac and Ir(mphmq)₂tmd. (b) The triplet transition dipole moments of Ir(phq)₃, Ir(mphq)₂acac, Ir(MDQ)₂acac and Ir(mphmq)₂tmd from three spin sublevels are shown as arrows. The transition dipole moments of the T_x, T_y and T_z sublevels correspond to the black, red and blue arrows respectively. Potential energy diagram of the exciplex formation 80

Figure 5.4 Refractive index of the undoped co-host layer (NPB:B3PYMPM, 1:1 molar ratio) film (50 nm thick) as measured by VASE. 83

Figure 5.5 Optimized binding geometries of the red dye co-host supramolecules. (a) B3PYMPM-Ir(mphq)₂acac-NPB, (b) B3PYMPM-Ir(MDQ)₂acac-NPB, (c) B3PYMPM-Ir(mphmq)₂tmd-NPB and (d) B3PYMPM-Ir(phq)₃-NPB..... 84

Figure 5.6 Isosurfaces of the molecular ESP. (a) Ir(phq)₃, (b) Ir(mphq)₂acac, (c) Ir(MDQ)₂acac, (d) Ir(mphmq)₂tmd, (e) NPB and (f) B3PYMPM. The numerals on the isosurfaces are in J/C. The electron-deficient nature of the *N*-heterocycles and the β -diketonate ancillary ligand interact strongly with the electron-rich region of the aromatic rings in the tail of the host molecules..... 87

Figure 5.7 Device structure and OLED performance for red dyes. (a) Schematic diagram of the device structure and the energy levels of the device. (b) *J-V-L* curves. Inset: the angular distribution of the EL intensity of the OLEDs. The dashed line in the inset shows the Lambertian distribution. (c) EL spectrum of the OLEDs. (d) EQEs and power efficiency as a function of the luminance..... 90

Figure 5.8 Optical simulation of the EQE of devices. (a) EQEs of the Ir(mphmq)₂tmd-based OLEDs with varying ETL thickness (circles with dots). The *J-V-L*, angle-dependent emission patterns, emission spectra, quantum efficiencies and

power efficiency data for these devices are shown in Figure 5.9-12. (b) Contour plot of the maximum EQEs achievable with Ir(mphmq)₂tmd possessing a certain PL quantum yield (q_{PL}) and ratio of the horizontal dipole (Θ). 93

Figure 5.9 Performance of OLEDs with different thicknesses of ETL (20, 25, 30, and 35 nm). (a) Current density–voltage–luminance curves. Inset: Angular distribution of the EL intensity of the OLEDs. The dashed line shows the Lambertian distribution. (b) EL spectra. (c) external quantum efficiencies and (d) power efficiencies versus luminance of the OLEDs..... 94

Figure 5.10 Performance of OLEDs with different thicknesses of ETL (50, 55, 60, and 65 nm). (a) Current density–voltage–luminance curves. Inset: Angular distribution of the EL intensity of the OLEDs. The dashed line shows the Lambertian distribution. (b) EL spectra. (c) external quantum efficiencies and (d) power efficiencies versus luminance of the OLEDs..... 95

Figure 5.11 Performance of OLEDs with different thicknesses of ETL (100, 105, 110, and 115 nm). (a) Current density–voltage–luminance curves. Inset: Angular distribution of the EL intensity of the OLEDs. The dashed line shows the Lambertian distribution. (b) EL spectra. (c) external quantum efficiencies and (d) power efficiencies versus luminance of the OLEDs. 96

Figure 5.12 Performance of OLEDs with different thicknesses of ETL (150, 155, 160, and 165 nm). (a) Current density–voltage–luminance curves. Inset: Angular distribution of the EL intensity of the OLEDs. The dashed line shows the Lambertian distribution. (b) EL spectra. (c) external quantum efficiencies and (d) power efficiencies versus luminance of the OLEDs. 97

Figure 6.1 (a) Molecular structures and (b) absorption and PL spectra of Ir(3-*mppy*)₂tmd, Ir(4-*mppy*)₂tmd, Ir(5-*mppy*)₂tmd, and Ir(3',5',4-*mppy*)₂tmd in chloroform..... 105

Figure 6.2 The triplet transition dipole moments of (a) Ir(3-*mppy*)₂tmd, (b) Ir(4-*mppy*)₂tmd, (c) Ir(5-*mppy*)₂tmd, and (d) Ir(3',5',4-*mppy*)₂tmd from the DFT calculations. Arrows represent the directions and relative magnitudes of the triplet transition dipole moments. 108

Figure 6.3 The triplet transition dipole moments of Ir(3-*mppy*)₂tmd, Ir(4-*mppy*)₂tmd, Ir(5-*mppy*)₂tmd, and Ir(3',4',5-*mppy*)₂tmd from three spin sublevels are shown as arrows. The transition dipole moments of the T_x, T_y and T_z sublevels correspond to the black, blue, red arrows respectively..... 109

Figure 6.4 Angle-dependent PL spectra of the p-polarized light from the 32 nm thick films composed of TCTA:B3PYMPM for (a) Ir(3-*mppy*)₂tmd, (b) Ir(4-*mppy*)₂tmd, (c) Ir(5-*mppy*)₂tmd, and (d) Ir(3',5',4-*mppy*)₂tmd, respectively. Dashed lines represent theoretical fits to the experimental data. (e) The ratio of horizontal emitting dipoles (Θ) in films against the angle between the C₂ axis and TDM (Φ) of the molecules..... 111

Figure 6.5 Electrostatic potential of iridium complexes. Unit of electrostatic potential is arbitrary unit. 113

Figure 6.6 (a) The current density–voltage–luminance curves of the OLEDs. Inset: the normalized EL spectra of the OLEDs and the angular distributions of the EL intensities of the OLEDs. The dashed line in the inset shows the Lambertian distribution. (b) EQEs and power efficiencies against luminance. (c) Contour plot of

the maximum achievable EQE possessing a certain PLQY and ratio of the horizontal dipoles compared with experimental EQE..... 115

Figure 7.1 (a) Chemical structures and (b) optimized geometries along with triplet transition dipole moments of Ir(3',5',4-mppy)₂tmd, Ir(dmppy-CF₃)₂tmd, Ir(dmppy-pro)₂tmd, and Ir(dmppy-ph)₂tmd from three sublevels are shown as bars based on the center of mass. The transition dipole moments of the T_x, T_y, T_z sublevels correspond to the blue, green, and red bars, respectively. Scaled TDMs were shown in inset of Figure 1(b)..... 126

Figure 7.2 The frontier molecular orbitals of the HICs at triplet state, calculated using the density functional theory with B3LYP/6-31+G(d) for C, H, N, O and LANL2DZ for Ir as basis set..... 130

Figure 7.3 (a) Absorption (close scatter) and PL spectra (open scatter) of Ir complexes in chloroform. (b) Angle-dependent PL intensities of the p-polarized light from the 30 nm thick films composed of TCTA:B3PYMPM: 4 wt% Ir complexes measured at 530 nm for Ir(3',5',4-mppy)₂tmd and Ir(dmppy-pro)₂tmd, 570 nm for Ir(dmppy-ph)₂tmd, and 590 nm for Ir(dmppy-CF₃)₂tmd, respectively..... 132

Figure 7.4 Angle-dependent PL spectra for (a) Ir(3',5',4-mppy)₂tmd, (b) Ir(dmppy-CF₃)₂tmd, (c) Ir(dmppy-pro)₂tmd, and (d) Ir(dmppy-ph)₂tmd, respectively. Dashed lines represent theoretical fits to the experimental data. 134

Figure 7.5 (a) Current density–voltage–luminance characteristics (b) EL spectra, (c) current efficiency and power efficiency as a function of the luminance of OLEDs, and (d) EQEs as a function of the current density with different Ir complexes as

dopants. Inset of (a) shows the angular distributions of the EL intensities of the OLEDs with the dashed line of the Lambertian distribution..... 136

Figure 8.1 Molecular structures of (a) Pt(fppz)₂, (b) Pt(f2bipz)(bpy) and (c) Pt(fppz)(pic). Isosurfaces of the molecular ESP for (d) Pt(fppz)₂, (e) Pt(f2bipz)(bpy), and (f) Pt(fppz)(pic). Optimized dimer geometries of (g) Pt(fppz)₂, (h) Pt(f2bipz)(bpy), and (i) Pt(fppz)(pic)..... 147

Figure 8.2 Optimized geometry of Pt(fppz)(pic) dimer at 180° rotational geometry. The binding energy of 180° rotational geometry (21.7 kcal/mol) is lower than that of 90° rotational geometry (29.5 kcal/mol). 149

Figure 8.3 GIWAXD images measured at 0.15° incident angle of 30 nm thick film (a) Pt(fppz)₂, (c) Pt(f2bipz)(bpy), (e) Pt(fppz)(pic) on silicon substrate. AFM images of 30 nm thick (b) Pt(fppz)₂, (d) Pt(f2bipz)(bpy), (f) Pt(fppz)(pic). 150

Figure 8.4 Unit cells of (a) Pt(fppz)₂ crystal in the film, (b) Pt(f2bipz)(bpy) crystal in the film, (c) Pt(fppz)₂ single crystal, (d) Pt(f2bipz)(bpy) single crystal. Orange arrows in (a) and (b) indicate the direction of transition dipole moments of MMLCT. (e) Angular volume fractions of Pt(fppz)₂, Pt(f2bipz)(bpy), and Pt(fppz)(pic) crystals in the film (f) Schematic drawing of Pt(fppz)₂ crystals in thin film..... 152

Figure 8.5 Projection view of thin film unit cell of Pt(f2bipz)(bpy). Y and Z axis are parallel to the substrate..... 154

Figure 8.6 GIWAXD images at various azimuthal angle with 30 nm thick film for (a) Pt(fppz)₂ at 0°, (b) Pt(fppz)₂ at 45°, (c) Pt(fppz)₂ at 90°, (d) Pt(f2bipz)(bpy) at 0°, (e) Pt(f2bipz)(bpy) at 45°, (f) Pt(f2bipz)(bpy) at 90°, (g) Pt(fppz)(pic) at 0°, (h) Pt(fppz)(pic) at 45°, (i) Pt(fppz)(pic) at 90°..... 155

Figure 8.7 Integration geometry of (200) 2D circular peak data in the spherical coordinate.....	157
Figure 8.8 GIWAX images of 30 nm thick Pt(fppz) ₂ neat film on (a) piranha treated Si substrate, (b) OTS treated Si substrate, (c) hole transporting materials deposited Si substrate.	159
Figure 8.9 (a) PL spectra of 10 ⁻⁵ M solution and thin film for Pt(fppz) ₂ , Pt(f2bipz)(bpy), and Pt(fppz)(pic). (b) Angle-dependent PL intensity of p-polarized light at 625 nm from platinum complex 30 nm thick film for Pt(fppz) ₂ , Pt(f2bipz)(bpy), and Pt(fppz)(pic).	160
Figure 8.10 Transient PLs of 30 nm thick films for Pt(fppz) ₂ , Pt(f2bipz)(bpy), and Pt(fppz)(pic).	162
Figure 8.11 Angle-dependent PL spectra of p-polarized light from platinum complex 30 nm thick film for (a) Pt(fppz) ₂ , (b) Pt(f2bipz)(bpy) and (c) Pt(fppz)(pic). Dashed lines represent theoretical fits to the experimental data.	163
Figure 8.12 Angle-dependent PL intensity of p-polarized light at 625 nm from 30 nm thick Pt(fppz) ₂ deposited on hole transporting material (fused silica/TCTA 5 nm/Pt(fppz) ₂ 30nm) and fused silica (fused silica/Pt(fppz) ₂ 30nm).	164
Figure 8.13 (a) <i>J-V-L</i> characteristics. (Inset: the angular distributions of the EL intensities of the OLEDs. The dashed line in the inset shows the Lambertian distribution.) (b) EL spectra of the OLEDs. (c) Current efficiency and power efficiency as a function of the luminance. (d) EQEs as a function of the current density.	167

Figure 8.14 A light emission image of a Pt(fppz)₂ based OLED at 0.75 mA/cm².
..... 169

Figure 8.15 Refractive indices of 30 nm thick (a) Pt(fppz)₂, (b) Pt(f2bipz)(bpy) and
(c) Pt(fppz)(pic) films..... 170

Chapter 1. Introduction

1.1 Brief history of organic light-emitting diodes

The optoelectronic properties of organic materials have been investigated actively for several decades, following the discovery of conducting polymers by A. J. Heeger *et al.*, for which he received the Nobel prize for chemistry in 2000. Organic semiconductor materials, due to their molecular diversity, offer multi-functionality in optoelectronic devices, and there is significant scope for economic and manufacturing advantages compared with inorganic semiconductor materials. The distinctive features of organic light-emitting diode (OLED) displays are high color purity, a large contrast ratio, and fast response times. OLEDs can be incorporated into a variety of substrates, including polymer films, metal foils, paper and glasses, and can form exceptionally thin and flexible layers, which can be transparent. OLEDs also represent a promising technology for lighting applications, with a number of advantages over fluorescent tubes and conventional LEDs. OLED lighting exhibits warm color temperatures and a high color rendering index, and can be used to create surface light sources, which can be flexible and transparent. The large potential markets have led many companies to develop OLED displays and OLED lighting products (see Figure. 1.1). However, OLEDs generally exhibit lower power efficiencies than conventional LED.

Electroluminescence from organic materials was first demonstrated by M. Pope *et al.* in 1963 using anthracene single crystals.¹ However, the operating voltage for these devices was high, and the efficiency was low. In 1987, C. W. Tang *et al.*

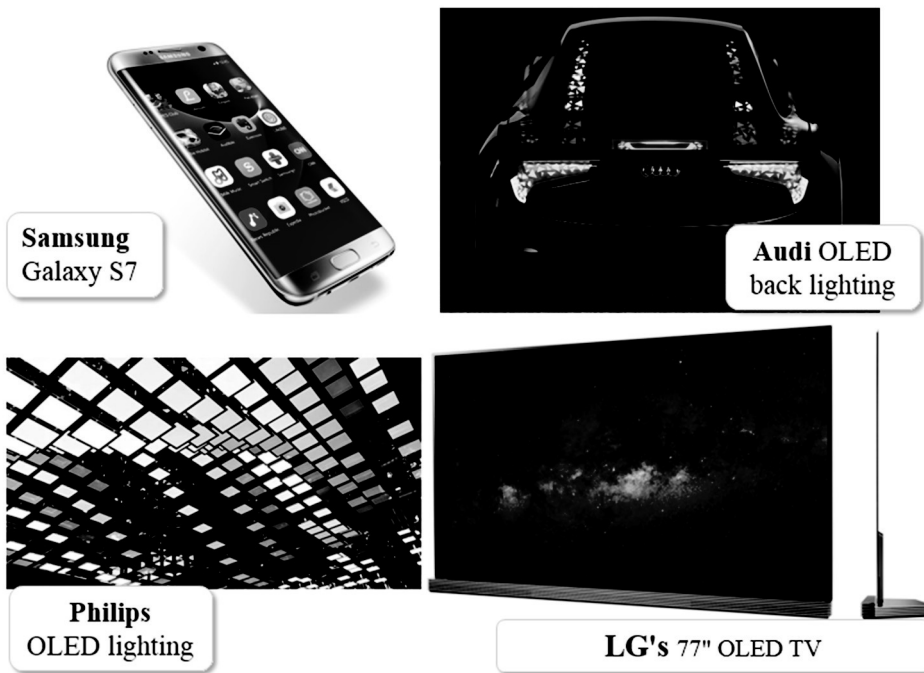


Figure 1.1 Applications of OLEDs as flexible display (upper left; Samsung Electronics 2016), car back lighting (upper right; Audi 2013), OLED lighting (lower left; Philips), OLED TV (lower right; LG Electronics 2016).

demonstrated OLEDs using a heterojunction consisting of a hole-transport layer (HTL) and an electron-transport layer (ETL).² They used Tris(8-hydroxyquinoline)aluminum(III) (Alq_3) as the ETL material, which acted not only as a charge-transport layer, but also as the light-emitting layer. In 1989, C. W. Tang *et al.* attempted to create an alternative color light source, and to improve on the efficiency of OLEDs, by developing a host–guest system, whereby red dye was used to dope an Alq_3 layer to transfer energy from Alq_3 to the red dye.³ However, the efficiency was low. The reasons for this were follows: 1) the exciton binding energy of organic emitters is high, 2) the exchange energy of the organic emitters is also high, and 3) the triplet excitons did not lead to efficient phosphorescence with only ~25% of the excitons leading to optical emission in those fluorescent light-emitting materials.

In 1998, M. A. Baldo *et al.* reported strong phosphorescence at room temperature using Pt-based organometallic compounds.⁴ Organometallic compounds with a heavy metal (Ir, Pt, Os, Ru) enabled triplet excitons to generate strong phosphorescence due to the strong spin-orbit coupling. The phosphorescent emitter with organometallic compounds exploited the excitons for optical emission. The development of the new phosphorescent emitters, leading to OLEDs with internal quantum efficiencies (IQEs) of 100%, was important in the commercialization of OLED devices.

Recently, C. Adachi *et al.* used triplet exciton harvesting via reverse intersystem crossing (RISC) to obtain a singlet state, without requiring heavy metal

compounds, demonstrating an IQE of 100%.⁵ The intramolecular charge transfer complexes and excited-state intermolecular charge transfer complexes (or exciplexes) reduce the energy gap between singlet and triplet states (ΔE_{ST}), resulting in efficient RISC from a triplet to singlet state.^{5,6} There has been much recent research interest in developing and synthesizing efficient thermally activated delayed fluorescence (TADF) materials and exciplex pairs with a small ΔE_{ST} to facilitate efficient RISC.

1.2 Efficiency of OLEDs

The external quantum efficiency (EQE) of OLEDs is one of the most important factors in evaluating the performance of emitting materials. The EQE, η_{EQE} , is defined as the number of photons per injected electron;⁷ i.e.,

$$\eta_{EQE} = \eta_{int} \times \eta_{out} = \gamma \times \eta_{S/T} \times q_{eff}(\phi_{PL}, \Gamma) \times \eta_{out}(\Theta, \Gamma) \quad (1)$$

where γ is the charge balance factor, $\eta_{S/T}$ is the fraction of radiative excitons ($\eta_{S/T}=0.25$ for fluorescent emitters and $\eta_{S/T}=1$ for phosphorescent emitters), and q_{eff} is the effective radiative quantum yield of the emitter in the cavity structure. Note that q_{eff} is a function of the PL quantum yield of the emitter in free space, ϕ_{PL} , as well as the structure of the microcavity, including the position of the emission zone represented by Γ (a factor related to the device structure). The out-coupling efficiency η_{out} depends on Γ and the proportion of horizontally oriented dipoles, $\Theta = (p_{\parallel} / p_{\parallel} + p_{\perp})$, where p_{\parallel} and p_{\perp} are the fractions of horizontal and vertical dipoles, respectively. The IQE of OLEDs can be improved significantly by exploiting triplet excitons in the emission process,^{4,5} by doping with *n*- or *p*-type dopants in the transport layers,^{8,9} or by the use of a charge injection layer¹⁰ to improve the charge injection and transport properties, resulting in an IQE of 100%. However, η_{out} of OLEDs is always much smaller than the IQE due to the large difference in the refractive index between the different layers in the structure.

1.3 Emitting dipole orientation of OLEDs

1.3.1 Effects of emitting dipole orientation

The orientation of the dipoles of the emitters is one of the most important material properties determining the efficiency of OLEDs. Horizontally oriented emitting dipoles in OLEDs lead to less losses from surface plasmon mode, and waveguide modes; thus, horizontally emitting dipoles increase the η_{out} of OLED. The theoretical limit of η_{out} for conventional bottom-emission OLEDs is approximately 30% under the assumption of isotropically oriented emitting dipoles (see Figure 1.2a).¹¹ In theory, EQEs in excess of 45% can be achieved using horizontally oriented emitting dipoles, without requiring a light extraction layer (see Figure. 1.3).⁷ Horizontally oriented transition dipole moments within the emitter have been demonstrated in polymer-based and vacuum-evaporated fluorescent OLEDs (FOLEDs).¹²⁻¹⁷ The orientation of the emitting dipoles of phosphorescent emitters based on iridium complexes in the emitting layer is considered to be isotropic due to the octahedral globular geometry (see Figure 1.2b); therefore, it is believed that the theoretical limit for the EQE of phosphorescent OLEDs (PhOLEDs) is 30%.¹¹ It has recently been reported that heteroleptic Ir complexes (HICs) exhibit preferential orientation of the emitting dipoles in the horizontal direction, implying that an EQE greater than 30% should be possible.^{7,18-20} However, the origin of the horizontal orientation of HICs has not previously been reported, and neither has an OLED with an EQE in excess of than 30%.

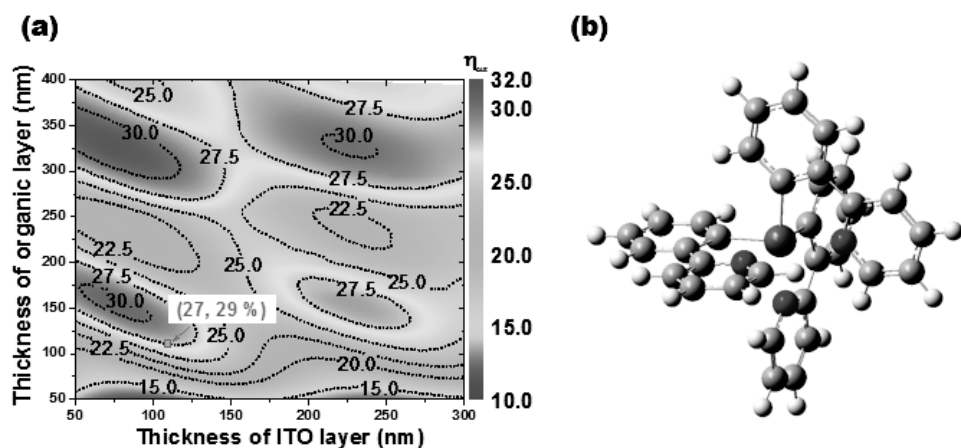


Figure 1.2 (a) Contour plot of theoretically maximum achievable EQE of green OLED as functions of thickness of organic layer and ITO layer assuming that the emitting dipole orientation is isotropic¹¹ (b) Optimized geometry of Ir(ppy)₃ at T₁ geometry calculating from DFT calculation.

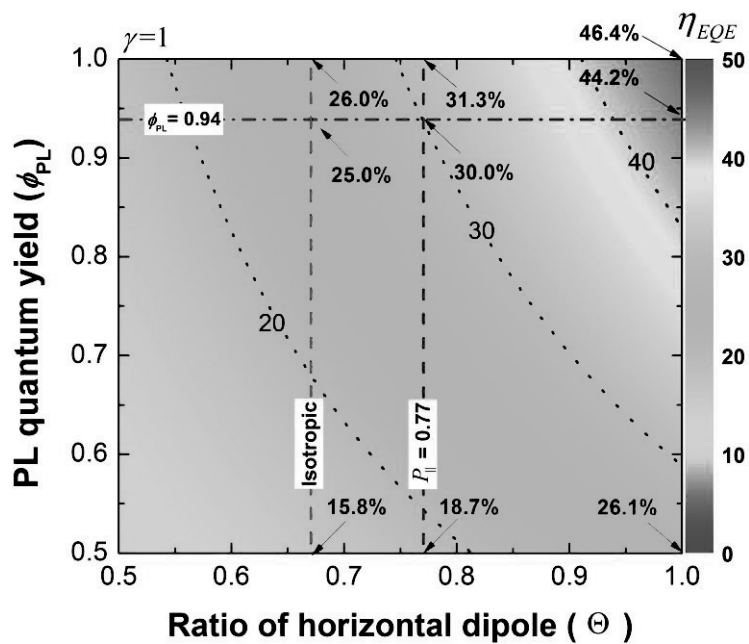


Figure 1.3 Contour plot of theoretically maximum achievable EQE of green OLED as functions of PL quantum yields and the ratio of horizontal dipoles of emitter.⁷

1.3.2 Analysis of the emitting (or transition) dipole orientation

The orientation of transition dipoles can be investigated using (1) variable angle spectroscopic ellipsometry (VASE) (2) angle dependent PL or EL analysis, and (3) exciton decay rate analysis. VASE is a well-known method of characterizing the optical anisotropy of amorphous layers (see Figure 1.4).^{21,22} Linearly polarized light with the same amplitude and phase angle for p- and s-polarized light was used as an incident light source, and differences in the amplitude and phase between the p- and s-polarized light were analyzed to obtain the refractive index n and the extinction coefficient k . These values were characterized by measuring reflected elliptically polarized light that underwent multiple reflections within the film, generating interference patterns. D. Yokoyama *et al.* reported transition dipole orientations of organic layers using VASE.¹⁶ VASE analysis can provide information on the orientation of the transition dipoles of a pristine film, but not on the orientation of the transition dipoles of dopants in a doped film. This is because the quantity of dopants in the host matrix is too small to detect using ellipsometry. Angle-dependent PL or EL spectroscopy can be used to analyze the orientation of transition dipoles of dopants.

W. Brütting *et al.* determined the orientation of emitting dipoles using angle-dependent PL and EL spectra (see Figure 1.5).^{17,18} Angle-dependent PL analysis has several advantages for characterizing the orientation of emitting dipoles in dye-doped films because the material properties (including the PL spectra and refractive indices) of the dye are not required to determine the orientation of the emitting dipoles. The emitting dipoles consist of p_x , p_y and p_z components, where p_x and p_y

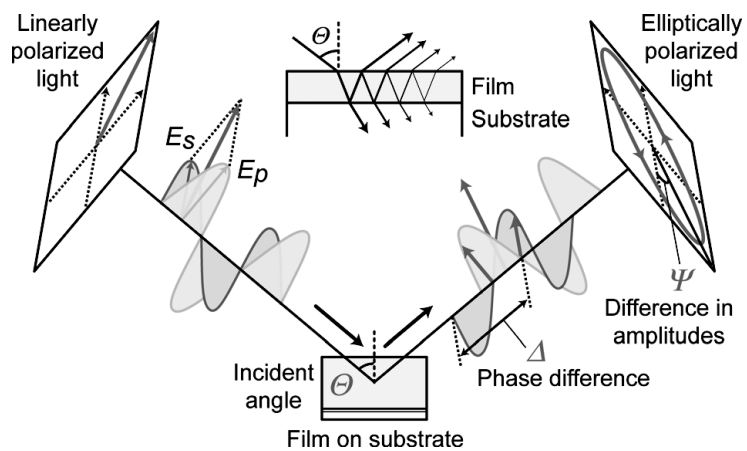


Figure 1.4 Schematic description of variable angle spectroscopic ellipsometry (VASE).^{16,22}

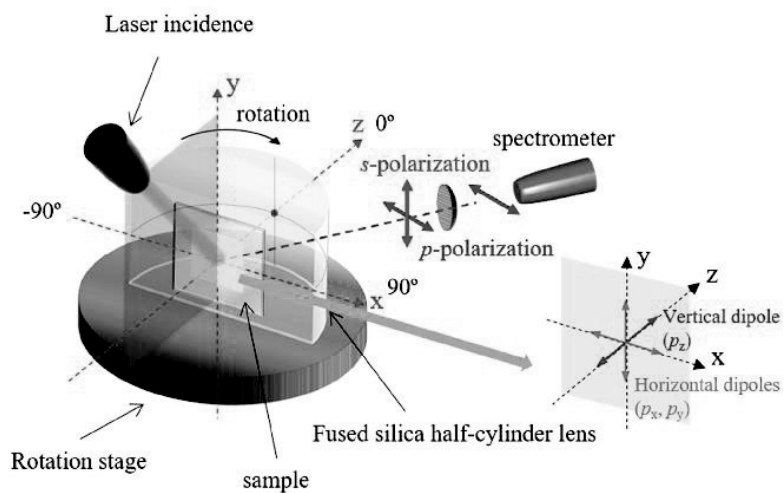


Figure 1.5 Schematic description of angle dependent PL spectra measurement setup.²³

are parallel to the plane of the substrate. The p_y dipoles radiate s-polarized light, whereas the p_x and p_z dipoles radiate p-polarized light. Thus, the orientation of the emitting dipoles can be determined by measuring the p-polarized light (comprising vertical dipole components) as a function of the detection angle. Angle-dependent PL spectra can be fitted based on the calculated angle-dependent spectra obtained from the classical dipole model developed by Chance, Prock and Silbey.²⁴ Using this model, the p- and s-polarized emission can be calculated separately from the horizontally and vertically oriented dipoles in a non-absorbing anisotropic medium. Since p_x and p_z exhibit significant differences in the intensity of the angle-dependent emission of the p-polarized light, simulating the p-polarized intensity with different ratios of p_x and p_z , and fitting the resulting experimental data, makes it possible to determine the fraction of horizontal dipoles. Using this method, the ratio of horizontal ($p_{\parallel} = p_x + p_y$) to vertical ($p_{\perp} = p_z$) dipoles can be determined. Either PL or EL analysis can be used to make the required measurements.

Neys *et al.* determined the orientation of emitting dipoles by analyzing the exciton decay rate Γ_{tot} .²⁰ The exciton decay rate in a microcavity structure is determined by the Purcell factor F , which depends on the optical environment and orientation of emitting dipoles.^{25,26} The total exciton decay rate Γ_{tot} can be expressed as follows:

$$\Gamma_{tot} = \Gamma_r + \Gamma_{nr} \quad (1.1)$$

where Γ_r is the radiative decay rate and Γ_{nr} is the non-radiative decay rate. The

Purcell factor of dipoles tilted by a given angle with respect to the substrate can be calculated from

$$F = (1 - \Theta)F_{\perp} + \Theta \cdot F_{\parallel} \quad (1.2)$$

where F_{\parallel} is the parallel component and F_{\perp} is the perpendicular component. These relations allow us to express the total exciton decay rate as

$$\Gamma_{tot} = F \cdot \Gamma_{r,0} + \Gamma_{nr} = [(1 - \Theta)F_{\perp} + \Theta \cdot F_{\parallel}] \cdot \Gamma_{r,0} + \Gamma_{nr} \quad (1.3)$$

where $\Gamma_{r,0}$ is the radiative decay rate in an infinite medium of constant refractive index. The decay rates can be measured using PL with samples consisting of an organic layer and an aluminum layer deposited on a glass substrate. The measured decay rates were fitted using simulated decay rates to determine the orientation of the emitting dipoles (see Figure 1.6).

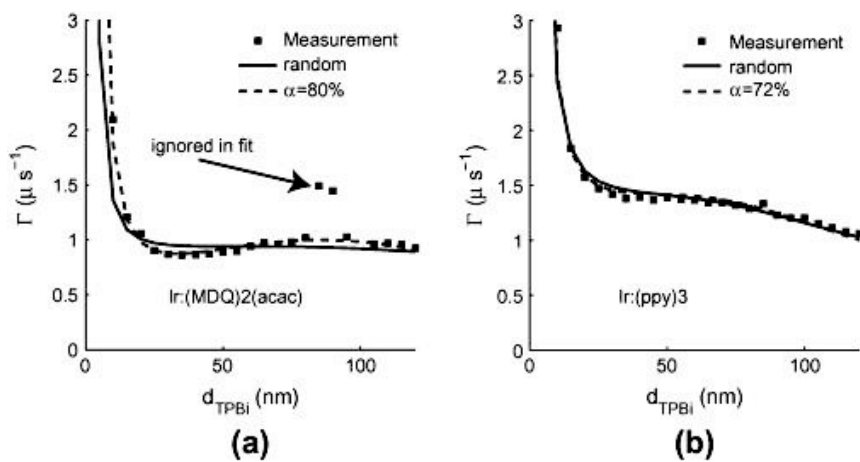


Figure 1.6 Calculated and measured exciton decay rate of dipoles as function of space thickness for (a) Ir(MDQ)₂acac and (b) Ir(ppy)₃.²⁰

1.4 Exciplex OLEDs

An exciplex is an excited charge transfer complex whereby the molecules are planar organic molecules forming a “sandwiched” structure. Interactions between electronically excited species M^* and ground-state molecules N lead to charge transfer interactions and excitation exchange interactions, and hence to the formation of stabilized complexes M^*N .²⁷ These complexes can be categorized into two types depending on their constituents: complexes consisting of the same molecules are referred to as excimers, and those consisting of differing molecules are referred to as exciplexes. Exciplexes have a large binding energy between molecules ($\sim 5\text{--}20$ kcal/mol), and exhibit partial charge character on each molecule.^{28,29}

Figure 1.7 shows a potential energy diagram of exciplex formation and emission. Here, monomer M^* is located far from monomer N , and the transition energy is the same as for monomer M^* . Monomer M^* is then located close to monomer N , and the binding energy between M^* and N increases due to charge-transfer interactions, resulting in a U-shaped potential (upper surface). The ground state energy increases as the distance between the molecules decreases due to the lack of substantial attractions between M and N (lower surface). Thus, there are a few MN ground state complexes and no associated optical absorption due to instabilities of the ground state complexes. Exciplex emission occurs vertically, according to the Franck–Condon principle, from the excited state minimum to the repulsive ground state. Thus, ground state MN complexes dissociate rapidly following emission, resulting in a short lifetime. For this reason, exciplex emission is red-shifted with a long decay

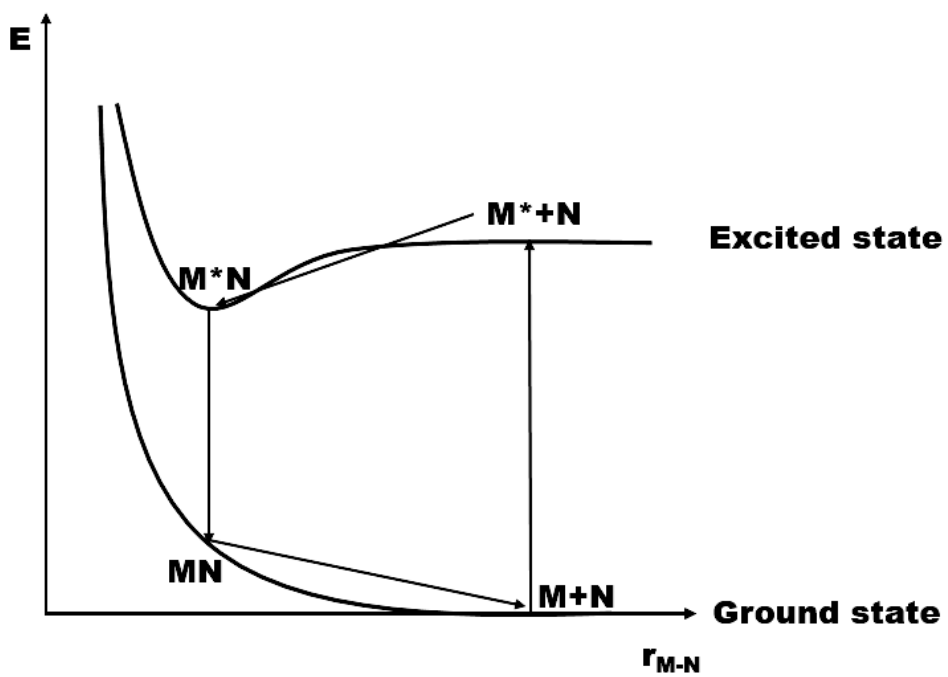


Figure 1.7 Potential energy diagram of the exciplex formation and emission.

lifetime, and is featureless because of the short lifetime and indefinite vibrational character of the ground state.²⁷

In recent years, highly efficient phosphorescent OLEDs (PhOLEDs) and Fluorescent OLEDs (FOLEDs) have been reported using exciplex hosts or emitters. Doping of phosphorescent emitters in exciplex-forming co-hosts has been reported to exhibit EQEs of greater than 30%, leading to devices with a low driving voltage and low efficiency roll-off due to perfect charge balance, a lack of an injection barrier from the charge-transport layers to the emitting layer, and a reduction in the quenching processes associated with the carrier and exciton densities in the emitting layer.³⁰⁻³⁵ The exciplex itself has also been explored for emission in OLEDs, and EQEs of 5–15% have been reported without dopants, utilizing RISC of the triplet exciplex.^{6,36-43} This is because of the very small ΔE_{ST} of exciplex, which facilitates efficient RISC.^{6,36} These results appear to indicate that the exciplex is a platform for efficient phosphorescent and FOLEDs. However, the efficiencies of FOLEDs formed using exciplex hosts or exciplex emitters are lower than FOLEDs based on single molecular TADF emitters, even though exciplex can, in principle, be used to achieve 100% IQE. In addition, there are no clear strategies for improving the efficiency of exciplex-based FOLEDs.

1.5 Outline of the thesis

In this thesis, we investigate the exciplex dynamics for triplet harvesting in FOLEDs and the orientation of the emitting dipoles of phosphorescent dye molecules for applications in high-efficiency PhOLEDs. Following on from this analysis, we demonstrate FOLEDs and PhOLEDs with unprecedented efficiencies.

The exciton dynamics that influence IQE exciplex emission in FOLEDs are quantitatively analyzed using temperature-dependent current density–voltage–luminance (*J-V-L*) measurements, as well as transient PL measurements. We show that a high RISC rate does not necessarily lead to efficient exciplex triplet harvesting if it occurs with a high non-radiative transition rate. A fluorescent OLED with IQE of 100% and an EQE of 25.2% at 150 K was demonstrated, which exhibited an IQE of 48.3% and EQE of 11.0% at room temperature; the increase in efficiency is attributed to a reduction in the non-radiative transition rate (Chapter 2).

In contrast to using the exciplex as an emitter, conventional fluorescent emission does not exhibit delayed fluorescence, and doped exciplex hosts can be exploited for RISC. A red fluorescent OLED with an unprecedented EQE of 10.6% was demonstrated using an exciplex system as a host with a conventional fluorescent emitter. The fraction of the radiative excitons was greater than 35%, which is clearly indicative of triplet harvesting in the system (Chapter 3).

The relationships between the orientation of the emitting dipoles and the molecular structure of the Ir complex were investigated using angle-dependent PL analysis. Homoleptic Ir complexes exhibit isotropic orientation of the emitting

dipoles; by contrast, heteroleptic iridium complexes (HICs) exhibit horizontally oriented emitting dipoles. Not only the ancillary ligand but also the main ligand of HICs are significantly influenced by the orientation of the emitting dipole of the HICs in an OLED. The origin of the preferred orientation of the transition dipole moments was investigated using quantum chemical calculations. This work shows that the preferred orientation of the transition dipole moments of HICs in OLEDs originates from the preferred direction of the HIC triplet transition dipole moments, as well as the strong supramolecular arrangement within the co-host environment. OLEDs with an EQE of 35.6% (red HICs) and 32.3% (green HICs) were demonstrated, with phosphorescent transition dipole moments oriented in the horizontal direction (Chapters 4 and 5).

The effects of the main ligands of HICs on the emitting dipole orientation in doped films were investigated to inform the design and synthesis of iridium complexes whereby the hydrogen atom(s) at different positions in the cyclometalated ligands of HIC were systematically replaced with methyl group(s). Molecules with a larger angle between the C_2 axis and the transition dipole moment in the molecules resulted in a larger fraction of horizontally oriented emitting dipoles in the emission layer. Based on this observation, a new green emitter with a large Θ of 80% and a PL quantum yield of 97% was developed, resulting in a green OLED exhibiting an unprecedented EQE of 34.1%, with a power efficiency of 157.6 lm/W and a current efficiency of 120.5 cd/A (Chapter 6).

Various substituents were investigated on the 4-position of the pyridine ring

of the HICs to improve the molecular orientation factor, as described in Chapter 5. We have shown that HICs can be aligned with the Ir-N bonds and TDMs parallel to the surface of doped films if the molecules have an elongated structure with a high aspect ratio, and exhibit strong intermolecular interactions between the donor and the host molecules. The Θ of the resulting HICs was in the range 80–86.5%, which is 1–7.5% greater than that of the reference HICs. This suggests that substituents on the 4-position of the pyridine ring significantly affect the molecular orientation factor, and hence also affect Θ . Consequently, a yellow phosphorescent OLED with an unprecedented EQE of 38% was demonstrated, as well as a green OLED with an EQE of 36% (Chapter 7).

The orientation of the emitting dipole and the crystal properties of thin films formed of undoped platinum complexes were investigated. The molecular orientation of the Pt complex in the film was analyzed using grazing incident wide-angle X-ray diffraction. Thin film crystals that were perfectly oriented along the (100) direction were obtained, resulting in a very large Θ of 93%. The orientation of the emitting dipoles of the crystalline emission layer was affected not only by the crystallinity of the layer, but also by the molecular arrangement within the crystal, which was determined by the symmetry and position of the CF₃-substituted pyrazolate units in the Pt complexes. An OLED with an unprecedented EQE of 39% was demonstrated using a crystalline emission layer (Chapter 8).

Chapter 2. Boosting triplet harvest by reducing non-radiative transition of exciplex toward fluorescent organic light-emitting diodes with 100% internal quantum efficiency

2.1 Introduction

The efficiency of fluorescent organic light-emitting diodes (OLEDs) based on thermally activated delayed fluorescent (TADF) emitters has been improved drastically by harvesting triplet excitons via reverse intersystem crossing (RISC), demonstrating internal quantum efficiency (IQE) of nearly 100% and external quantum efficiency (EQE) of 30% exhibiting intra-molecular charge transfer in recent years.^{5,44-54} Efficient RISC from triplet to singlet state is available using the intra-molecular charge transfer complexes to reduce the energy gap between singlet and triplet states (ΔE_{ST}). There are large research activities to synthesize efficient TADF materials with small ΔE_{ST} to facilitate efficient RISC.

Excited state inter-molecular charge transfer complexes (exciplexes) have also been used to reduce the singlet-triplet energy gap for efficient RISC.^{6,36-43} In recent years, high efficiency phosphorescent and fluorescent OLEDs were reported using exciplex as hosts or emitters. Doping of phosphorescent emitters in exciplex forming co-hosts has been reported to exhibit EQEs over 30%, low driving voltage and low efficiency roll-off, coming from perfect charge balance, no injection barriers for the charges from the charge transporting layers to the emitting layer and reducing quenching process by lowering the carrier and exciton densities in the emitting layer.³⁰⁻³⁵ Moreover, doping of conventional fluorescent emitters in exciplex forming

co-hosts resulted in the EQE of 10~15%.⁵⁵⁻⁵⁷ Exciplex itself has also been explored as emitters in OLEDs exhibiting EQEs of 5~15% without dopant by utilizing RISC of triplet exciplex.^{6,36-43} These results seem to indicate that exciplex is a platform for efficient phosphorescent and fluorescent OLEDs. Unfortunately, however, the efficiencies of the fluorescent OLEDs using exciplex hosts or exciplex as emitters are still lower than fluorescent OLEDs based on single molecular TADF emitters even though exciplex can, in principle, realize 100% IQE because of very low ΔE_{ST} facilitating efficient RISC.^{6,36} In addition to that there are no clear guidelines to improve the efficiency in exciplex based fluorescent OLEDs.

In this work, we quantitatively analyze the exciton dynamics influencing IQE of exciplex and demonstrate a fluorescent OLED with IQE of 100% and EQE of 25.2% at 150 K, which are improved from IQE of 48.3% and EQE of 11.0% at room temperature by reducing non-radiative transition of exciplex. This study shows that high RISC rate (k_{RISC}) does not necessarily lead to efficient harvesting of triplet exciplex if it occurs with high non-radiative transition rate (k_{nr}). High IQE requires not only efficient RISC but also low non-radiative loss in both singlet and triplet exciplexes for sufficient triplet harvesting. We harvested more triplet exciplex by adopting exciplex with low k_{nr} and further suppressed the k_{nr} by freezing the exciplex, to achieve IQE of 100%.

2.2 Experimental

Organic materials were purchased from Nichem Fine Technology. The OLEDs were fabricated on clean glass substrates pre-patterned with 70-nm-thick ITO under the pressure of 5×10^{-7} Torr by thermal evaporation without breaking the vacuum. Before the deposition of organic layers the ITO substrates were pre-cleaned with isopropyl alcohol and acetone, and then exposed to ultraviolet-ozone for 10 min. Each layer was deposited at a rate of 1 Å/s and the deposition rate of the co-deposited layers was 1 Å/s in total.

Current density, luminance, and EL spectra were measured using a programmable source meter (Keithley 2400) and a spectrophotometer (Spectrascan PR650, Photo Research) which measures power per unit steradian per unit wavelength per unit area ($\text{W}/\text{nm} \cdot \text{sr} \cdot \text{m}^2$) at normal direction. Luminance of an OLED was calculated from power of light considering the CIE luminosity function. The angular distribution of the EL was measured with a programmable source meter (Keithley 2400), goniometer, and fiber optic spectrometer (Ocean Optics S2000). The EQE and the power efficiency of the OLEDs were calculated from current density–voltage–luminance characteristics, EL spectra, and the angular distribution of the EL intensity.

Transient photoluminescence (PL) was measured by using a pulsed N2 laser (KEN-2X, USHO) as the excitation light source and a streak camera (C10627, Hamamatsu) as the optical detection system.

2.3 Result and discussion

Chemical structures of the materials used in this study are shown in Figure 2.1a. We used 4,4',4''-tris(N-carbazolyl)-triphenylamine (TCTA) as the donor and 4,6-bis[3,5-(dipyrid-4-yl)phenyl]-2-methylpyrimidine (B4PYMPM)⁵⁸ as the acceptor. PL spectra of TCTA, B4PYMPM and TCTA:B4PYMPM co-host films at 300 K. The molar ratio of TCTA to B4PYMPM in the TCTA:B4PYMPM co-deposited film was 1:1. The peak wavelengths of the PL spectra were 393 nm for TCTA, 420 nm for B4PYMPM, and 509 nm for the TCTA:B4PYMPM co-host film, respectively (Figure 2.1b). The PL spectrum of the co-deposited film showed red shifted featureless emission from the PL spectra of the consisting materials, indicating that the mixed film forms exciplex whose energy is similar to the difference between the lowest unoccupied molecular orbital (LUMO) level of B4PYMPM and the highest occupied molecular orbital (HOMO) level of TCTA. The time resolved PL spectra showed that the exciplex emission shifts to longer wavelengths with increasing delay time probably due to broad distributions of the singlet and the triplet energies of the exciplex (Figure 2.2).³⁶ The PL quantum yield (PLQY) of the TCTA:B4PYMPM exciplex was $60 \pm 2\%$ at 300 K.

The transient PL intensities of the exciplex emission at various temperatures are shown in Figure 2.3a, where the transient PL intensity was integrated from 350 nm to 750 nm. The transient PL decays showed significant delayed emission along with prompt emission, indicating that triplet exciplex participates in the emission. The rate constants of the prompt emission (k_p) extracted from the slope of the decay

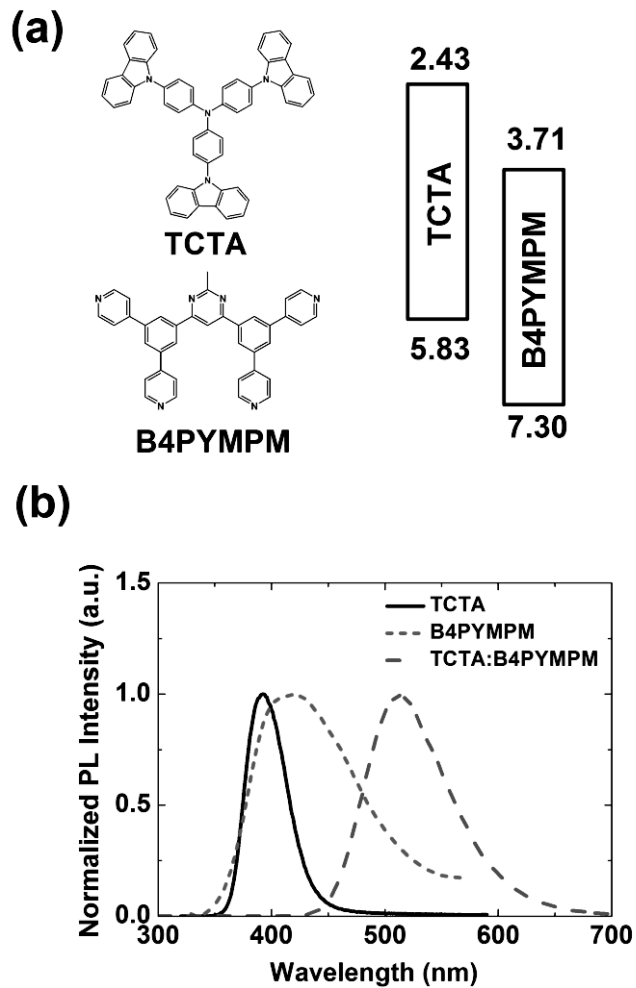


Figure 2.1 (a) Chemical structures and energy levels of TCTA and B4PYMPM. (b) PL spectra of TCTA, B4PYMPM, and TCTA:B4PYMPM.

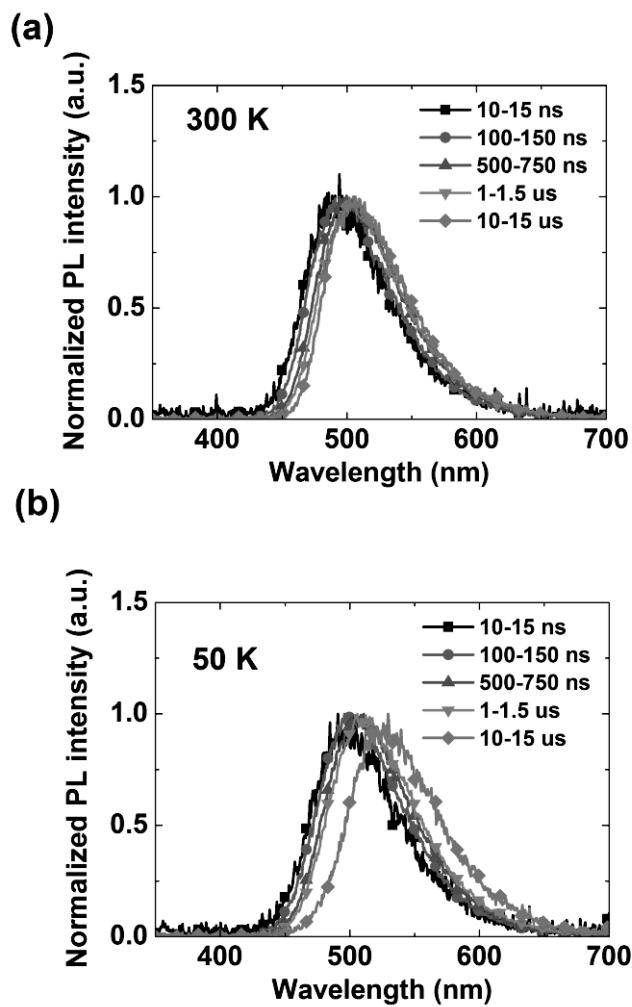


Figure 2.2 Time resolved PL spectra of the TCTA:B4PYMPM film at various times after excitation at (a) 300 K and (b) 50 K.

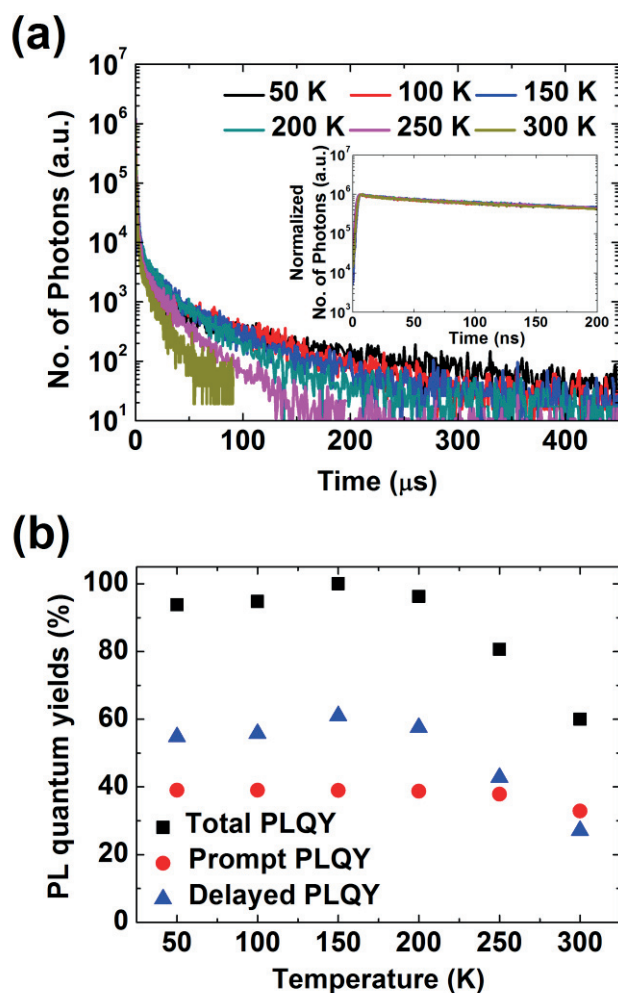


Figure 2.3 (a) Transient PL decay patterns of the TCTA:B4PYMPM film at various temperatures within long time range (0 – 450 μs) (inset: normalized transient PL decay of the TCTA:B4PYMPM film at various temperatures within short time range (0 – 200 ns)). The transient PL intensities were obtained from the integration of the emission spectra from the wavelength of 350 nm to 750 nm. (b) Temperature dependence of PLQY for total (black square), prompt (red circle), and delayed (blue triangle) components of the TCTA:B4PYMPM exciplex.

curves are almost the same as $4.0 \times 10^6 \text{ s}^{-1}$ regardless of temperature (inset of Figure 2.3a). However the delayed emission showed multi-exponential decays, supporting the existence of a broad distribution of the energy level of the exciplex described before. Low bound of the rate constant of the delayed emission (k_d) decreases as the temperature is reduced. The PLQYs of the prompt (Φ_p) and the delayed components (Φ_d) at various temperatures were calculated by the integration of the prompt and delayed transient PL intensities and calibrated with the PLQY of the exciplex emission measured at room temperature using an integration sphere and are shown in Figure 2.3b. The PLQY of the exciplex reaches 100% at 150 K due to large increment of Φ_d , indicating 100% harvest of triplet exciplex.

The exciplex dynamics of the singlet and triplet has been analyzed based on the energy diagram and transition rates shown in Figure 2.4a. In the presence of the intersystem crossing (ISC) and the RISC between singlet and triplet states, the k_p and k_d can be expressed as follows under the assumption that the radiative (k_r^S) and non-radiative (k_{nr}^S) transition rate of the singlet and the rate constant of ISC (k_{ISC}) are significantly faster than those of non-radiative transition rate of the triplet exciplex (k_{nr}^T) and the rate constant of RISC (k_{RISC}).^{6,36}

$$k_p = k_r^S + k_{nr}^S + k_{ISC} \quad (2.1)$$

$$k_d = k_{nr}^T + \left(1 - \frac{k_{ISC}}{k_r^S + k_{nr}^S + k_{ISC}} \right) \cdot k_{RISC} \quad (2.2)$$

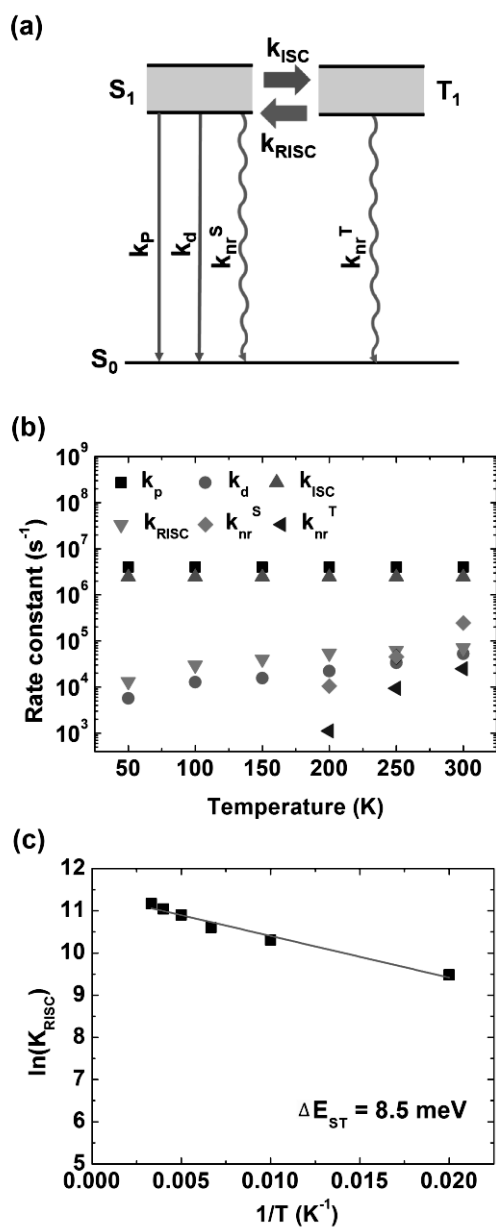


Figure 2.4 (a) The exciplex dynamics of the singlet and triplet has been analyzed based on the energy diagram and transition rates. (b) k_p , k_d , k_{ISC} , k_{RISC} , k_{nr}^S , and k_{nr}^T at various temperatures. (c) Arrhenius plot of the RISC rate in TCTA:B4PYMPM exciplex systems. The activation energy of the RISC rate is found to be 8.5 meV.

The PLQY of 100% at 150 K indicates that k_{nr}^S and k_{nr}^T are negligibly small at the temperature. Thus, k_{ISC} can be expressed as $k_p(1-\Phi_p)$ at 150 K using Equation (2.1) and k_{ISC} is $2.44 \times 10^6 \text{ s}^{-1}$. Assuming that k_{ISC} is independent of temperature because the ISC process is considered as an adiabatic process, k_{RISC} is obtained from the following equation^{6,36}:

$$k_{RISC} = \frac{k_p k_d \Phi_d}{k_{ISC} \Phi_p} \quad (2.3)$$

k_{nr}^S and k_{nr}^T above the temperature of 150 K were obtained from Equation (2.1) and Equation (2.2) from experimentally obtained rate constant's. All the transition rates at various temperatures are displayed in Figure 2.4b and summarized in Table 2.1. k_{nr}^S and k_{nr}^T are exponentially reduced as the temperature is reduced and becomes zero at 150 K. Non-radiative transitions could be coming from phonon mediated process as well as dissociation of exciplex to free charge carriers because both of them are activated by environmental thermal energy. Origin of the non-radiative decay of exciplex has not fully understood yet and further study is required to clarify it. k_{RISC} was reduced but with much slower rate than the reduction rate of the nonradiative rate constants as the temperature was decreased, indicating that the activation energy is very small. The activation energy of 8.5 meV was estimated from the Arrhenius plot of k_{RISC} shown in Figure 2.4c, manifesting that ΔE_{ST} is indeed much smaller than the thermal energy at room temperature in this system and most the single molecular TADF emitters. However, the PLQY stays at 60% even

Table 2.1 k_r^S , k_p , k_d , k_{ISC} , k_{RISC} , k_{nr}^S , k_{nr}^T at various temperatures. The unit of transition rates is s^{-1} .

	k_r^S	k_p	k_d	k_{ISC}	k_{RISC}	k_{nr}^S	k_{nr}^T
300 K	1.32×10^6	4.00×10^6	5.26×10^4	2.44×10^6	7.11×10^4	2.44×10^5	2.49×10^4
250 K	1.51×10^6	4.00×10^6	3.38×10^4	2.44×10^6	6.27×10^4	4.54×10^4	9.40×10^3
200 K	1.55×10^6	4.00×10^6	2.23×10^4	2.44×10^6	5.43×10^4	1.05×10^4	1.12×10^3
150 K	1.56×10^6	4.00×10^6	1.57×10^4	2.44×10^6	4.03×10^4	-	-
100 K	1.56×10^6	4.00×10^6	1.28×10^4	2.44×10^6	2.99×10^4	-	-
50 K	1.56×10^6	4.00×10^6	5.71×10^3	2.44×10^6	1.31×10^4	-	-

with such a low activation energy and high RISC rate as a result of a large nonradiative loss at room temperature. At 150 K, on the contrary, the PLQY reaches 100% because k_{nr}^S or k_{nr}^T decreases to a larger extent than it does for other transition rates. At the temperature lower than 150 K, PLQY goes down because Φ_d decreases with the reduced k_{RISC} . This analysis clearly demonstrate that high k_{RISC} with low ΔE_{ST} does not necessarily lead to efficient harvest of triplet exciplex if k_{nr} is high. High IQE requires not only efficient RISC but also low nonradiative loss.

Similar behavior was observed in the TCTA: bis-4,6-(3,5-di-3-pyridylphenyl)-2-methylpyrimidine (B3PYMPM) mixed film which exhibited the PLQY of 36% at 300 K and reached PLQY of 99% at 35 K.³⁶ However, the PLQY of the TCTA:B4PYMPM exciplex was 1.7 times higher at room temperature and reached 100% at higher temperature of 150 K than that of TCTA:B3PYMPM exciplex even though k_r^S of TCTA:B4PYMPM ($1.3 \times 10^6 \text{ s}^{-1}$) is lower than that of TCTA:B3PYMPM ($7.0 \times 10^6 \text{ s}^{-1}$) at room temperature. Higher PLQY of TCTA:B4PYMPM at room temperature does not come from higher k_{RISC} value but from smaller nonradiative transition rate than TCTA:B3PYMPM. k_{RISC} of TCTA:B4PYMPM ($7.11 \times 10^4 \text{ s}^{-1}$) is only slightly higher than that of TCTA:B3PYMPM ($5 \times 10^4 \text{ s}^{-1}$) but the k_{nr}^S of TCTA:B3PYMPM ($1.27 \times 10^7 \text{ s}^{-1}$) is fifty times higher than that of TCTA:B4PYMPM ($2.44 \times 10^5 \text{ s}^{-1}$). The lower value of

k_{nr}^S resulted in the higher Φ_p of TCTA:B4PYMPM (33%) which is 1.4 times higher than that of TCTA:B3PYMPM (23%), and higher Φ_d at room temperature.

An OLED was fabricated using the exciplex emitter. The device structure of the OLED was as follows; indium tin oxide (ITO) (70 nm)/1,1-bis((di-4-tolylamino)phenyl)cyclohexane (TAPC) (75 nm)/TCTA (10 nm)/TCTA:B4PYMPM (1:1, 30 nm)/B4PYMPM (40 nm)/LiF (0.7 nm)/Al (100 nm). The current density–voltage–luminance (J – V – L) characteristics of the exciplex OLED (Figure 2.5a) at various temperatures show the low turn-on voltage of 2.5 V at room temperature and 7 V at 150 K, due to the reduction of the mobility of charge carriers with decreasing temperature. The electroluminescent (EL) spectra of the device (Figure 2.5b) are almost the same as the PL spectra of the exciplex (Figure 2.6). The EQEs and current efficiencies (CEs) of the devices at various temperatures are displayed in Figure 2.5c. The EQE of the device was calibrated using the angle-dependent emission intensity profile. The maximum efficiencies of the OLED were EQE of 11.0% and CE of 28.9 cd/A, but the efficiency were drastically improved to EQE of 25.2% and CE of 63.5 cd/A as temperature was decreased to 150 K. The EQE of the TCTA:B4PYMPM device (11.0%) at room temperature is 3.5 times higher than that of TCTA:B3PYMPM's (3.1%), indicating that low nonradiative transition rate results in higher efficiency in the TCTA:B4PYMPM OLED. The nonradiative transition in the TCTA:B4PYMPM device was further suppressed by decreasing temperature to get EQE of 25.2% at 150 K.

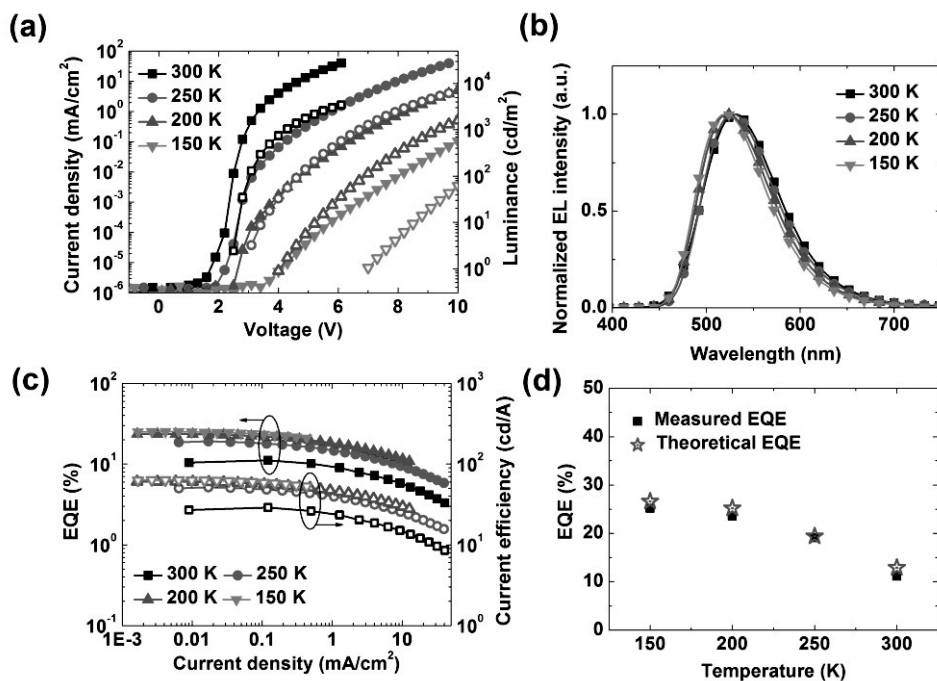


Figure 2.5 (a) The $J-V-L$ curves of the OLED at various temperatures. Solid scatter indicates current density and open scatter indicates luminance. (b) EL spectra of OLED with 0.1 mA/cm² at various temperatures. (c) The EQEs and CEs against current density at various temperatures. (d) Measured EQEs and theoretical EQEs at various temperatures. Outcoupling efficiencies of OLED were calculated with optical simulation based on the measured the ratio of horizontal emitting dipoles (61%), under the assumption of no electrical loss.

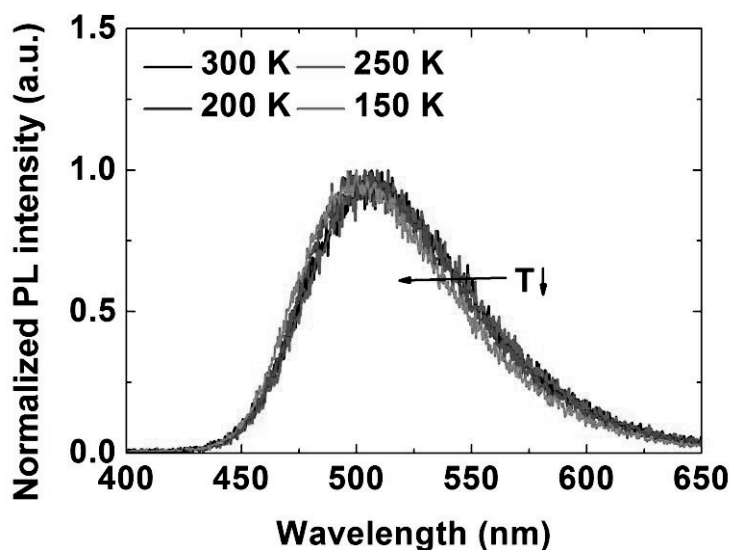


Figure 2.6 PL spectra of TCTA:B4PYMPM 30 nm thick film at various temperature.

The RISC efficiency (Φ_{RISC}) and IQEs of the OLED were analyzed using the experimentally obtained values using the following equations, where Φ_{ISC} is the efficiency of ISC of singlet exciplex.^{6,36} Equation (2.6) is obtained from Equation (2.5).

$$\Phi_{ISC} = \frac{k_{ISC}}{k_p} \quad (2.4)$$

$$\Phi_d = \sum_{k=1}^{\infty} (\Phi_{ISC} \Phi_{RISC})^k \Phi_p \quad (2.5)$$

$$\Phi_{RISC} = \frac{\Phi_d}{\Phi_{ISC} \cdot (\Phi_p + \Phi_d)} \quad (2.6)$$

$$IQE = \sum_{k=0}^{\infty} 0.75 \cdot \Phi_p \Phi_{RISC} (\Phi_{ISC} \Phi_{RISC})^k + \sum_{k=0}^{\infty} 0.25 \cdot \Phi_p (\Phi_{ISC} \Phi_{RISC})^k \quad (2.7)$$

The results are shown in Figure 2.7. Φ_{RISC} and IQE were increased with decreasing temperature for both of them to reach 100% at 150 K.

Outcoupling efficiency of the OLED was calculated using the optical simulation based on the measured ratio of horizontal emitting dipoles (61%).^{24,59} Birefringence of the film of TCTA:B4PYMPM was considered to calculate the outcoupling efficiency. The outcoupling efficiency was 26.6% assuming that emission zone was located middle of emitting layer. The theoretical EQEs calculated using the calculated outcoupling efficiency and the IQEs were 12.9% at 300 K and 26.6% at 150 K. The experimentally obtained maximum EQEs at different temperatures are well consistent with theoretical EQEs as shown in Figure 2.5d, indicating that the electrical loss is almost zero in the device even at low temperature.

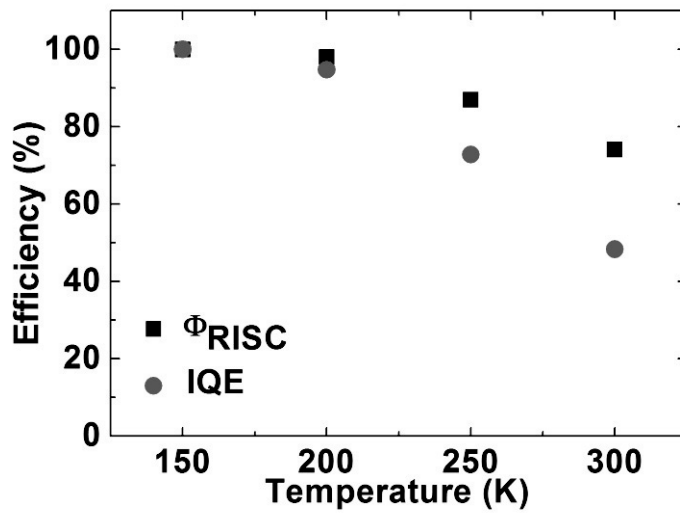


Figure 2.7 Φ_{RISC} and IQE against temperature. IQE was obtained with experimentally observable values using the Equation (2.7).

2.4 Conclusion

In conclusion, we realized a fluorescent OLED with IQE of 100% and EQE of 25.2% at 150 K by reducing the non-radiative transition of exciplex. Our results show that not only efficient RISC but also low nonradiative loss in both singlet and triplet exciplexes is required for efficient exciplex based OLEDs. Even though the high efficiency approaching the 25.2% EQE was obtained at low temperature, these results clearly demonstrate that OLEDs with 100% IQE harvesting all the triplets are possible using exciplex if an exciplex system is designed to have almost zero non-radiative process of triplet exciplex by clever design of molecules.

Chapter 3. Triplet harvesting by a conventional fluorescent emitter using reverse intersystem crossing of host triplet exciplex

3.1 Introduction

Fluorescent organic light-emitting diodes (FOLEDs) have advantages over phosphorescent OLEDs (PhOLEDs) in terms of flexibility of material design, low price, long device lifetime, and short exciton lifetime. One critical drawback of fluorescent OLEDs is the low efficiency because only singlet excitons can be harvested by fluorescent molecules.

Use of delayed fluorescence originated either from triplet–triplet annihilation^{60,61} (TTA) or thermally activated reverse intersystem crossing^{5,6,36-54} (RISC) from triplet to singlet excitons have been actively pursued to increase the efficiency of fluorescent OLEDs. Both intra- and intermolecular charge transfer complexes upon excitation have been used to reduce the singlet–triplet energy gap for efficient RISC.^{5,6,36-54} Among them, the intramolecular charge transfer materials exhibiting thermally activated delayed fluorescence (TADF) have been very successful in recent years, demonstrating the external quantum efficiency (EQE) over 20%.^{49,50} Performance of the OLEDs using the excited state intermolecular charge transfer complexes (exciplexes) have also been improved steadily, demonstrating EQE over 10%.^{6,36-41} One drawback of the TADF and exciplex

materials in OLEDs is their broad emission spectra compared to fluorescent molecules without delayed fluorescence. Device stability is an issue to be discussed further.

Instead of using the exciplex as an emitter, exciplex forming systems have been used as host for phosphorescent and TADF OLEDs in recent years.^{30-35,50} The exciplex host composed of an electron transporting material (ETM) and hole transporting material (HTM) behaves as a bipolar host and removes the charge injection barrier from the charge transporting layers to the emitting layer (EML). The host allows an efficient singlet and triplet energy transfer from the exciplex to the dopant because the singlet and triplet energy of the exciplex are almost identical. Using the characteristics of the exciplex systems, we have demonstrated highly efficient phosphorescent and TADF OLEDs with the EQEs over 30%, low turn on voltage and low efficiency roll-off.^{30-35,50}

Doping of conventional fluorescent molecules in TADF host or use of TADF molecules as assistant dopants in fluorescent host doped with fluorescent molecules have been reported to take advantage of narrow emission spectra and high stability of fluorescent molecules on the one hand, and efficient RISC of the triplet exciton to the singlet exciton in the TADF molecules on the other hand, to harvest both singlet and triplet excitons by the Förster energy transfer from the TADF molecules to the fluorescent dopant.^{62,63} This concept has been quite successful to reach the EQE over 10% using TADF materials as host or sensitizers recently in fluorescent OLEDs. Zhang et al. reported EQE of 10% using 2-biphenyl-4,6-bis(12-phenylindolo)-[2,3-a]carbazole-11-yl)-1,3,5-triazine as TADF host and 3,11-diphenylamino-7,14-

diphenylacenaphtho[1,2-k]fluoranthene as a conventional fluorescent emitter⁶² and Nakanotani et al. reported EQE of 18% using TADF materials as assistant dopant.⁶³ However, in order to utilize the RISC efficiently in a fluorescent dye doped OLEDs, it is desirable to form excitons on TADF materials rather than direct formation on the fluorescent dopant. In this regard, exciplex forming cohost systems are good candidates as host for fluorescent dopants because the bimolecular recombination on host molecules is dominant rather than the trap assisted recombination as reported in an exciplex host doped with a phosphorescent dye.³⁵

Here, we report a red fluorescent OLED with unprecedented high EQE of 10.6% using an exciplex system as host for a conventional fluorescent dopant not showing delayed fluorescence. The fraction of the radiative exciton is over 35% by using the exciplex host, clearly indicating the triplet harvesting in the system.

3.2 Experimental

Organic materials were purchased from Nichem Fine Technology. The OLEDs were fabricated on clean glass substrates prepatterned with 100-nm-thick ITO under a pressure of 5×10^{-7} Torr by thermal evaporation without breaking the vacuum. Before the deposition of organic layers the ITO substrates were precleaned with isopropyl alcohol and acetone, and then exposed to ultraviolet-ozone for 10 min. Each layer was deposited at a rate of 1 Å/s and the deposition rate of the codeposited layers was 1 Å/s in total.

Density functional theory (DFT) and time dependent-DFT calculations were performed using Gaussian09 program.⁶⁴ The optimization of geometry and TDM were calculated using B3LYP, 6-31g(d) basis set for all atoms.

Current density, luminance, and EL spectra were measured using a programmable source meter (Keithley 2400) and a spectrophotometer (Spectrascan PR650, Photo Research). The angular distribution of the EL was measured with a programmable source meter (Keithley 2400), goniometer, and fiber optic spectrometer (Ocean Optics S2000). The EQE and the PE of the OLEDs were calculated from $J-V-L$ characteristics, EL spectra, and the angular distribution of the EL intensity.

Orientation of TDMs was measured using a continuous wave laser (325 nm, melles Griot). The incident angle of the excitation source was fixed at 45°. *P*-polarized PL spectra were detected 600 nm by a fiber optic spectrometer (Ocean Optics Maya2000).

Transient PL was measured by using a pulsed ND:YAG laser (355 nm,

Continuum) as the excitation light source and intensified charge coupled device (PI-MAX, Princeton Instruments) as optical detection system.

3.3 Result and discussion

Figure 3.1a shows the chemical structures of the host and the red-emitting dopant used in this study. The red fluorescent dopant 4-(dicyanomethylene)-2-tert-butyl-6-(1,1,7,7-tetramethyljulolidyl-9-enyl)-4H-pyran (DCJTb) was used as the emitter which showed a high photoluminescence (PL) quantum yield and negligible delayed fluorescence with the EQEs of 3% – 6% in previous reports.⁶⁵⁻⁶⁸ 4,4',4''-tris(*N*-carbazolyl)-triphenylamine (TCTA) and 4,6-bis[3,5-(dipyrid-4-yl)phenyl]-2-methylpyrimidine (B4PYMPM)⁵⁸ were used as the exciplex host.

The PL spectra of TCTA, B4PYMPM and the mixed films with 1:1 ratio are shown in Figure 3.1b. The peak wavelengths were 393 nm for TCTA, 420 nm for B4PYMPM, and 509 nm for the mixed film, respectively. The mixed film showed a broad featureless emission red shifted from the consisting materials, indicating that the mixed film forms exciplex upon excitation. The delayed PL spectrum of the exciplex measured after 10 μ s at 30 K was almost the same as the one measured at room temperature, suggesting almost the same energy levels of the triplet and the singlet exciplexes. The PL quantum yield of TCTA:B4PYMPM exciplex measured using a 50 nm thick mixed film on a quartz substrate in an integrating sphere was $60 \pm 2\%$, which was much larger than that of Alq₃ (32%) widely used as host for red fluorescent emitters.⁶⁹ The absorption spectrum of the TCTA:B4PYMPM mixed film was fitted very well with the weighted linear combination of the absorption spectra of TCTA and B4PYMPM as presented in Figure 3.1c, indicating that aggregates or charge transfer complexes are not formed in the ground state of the

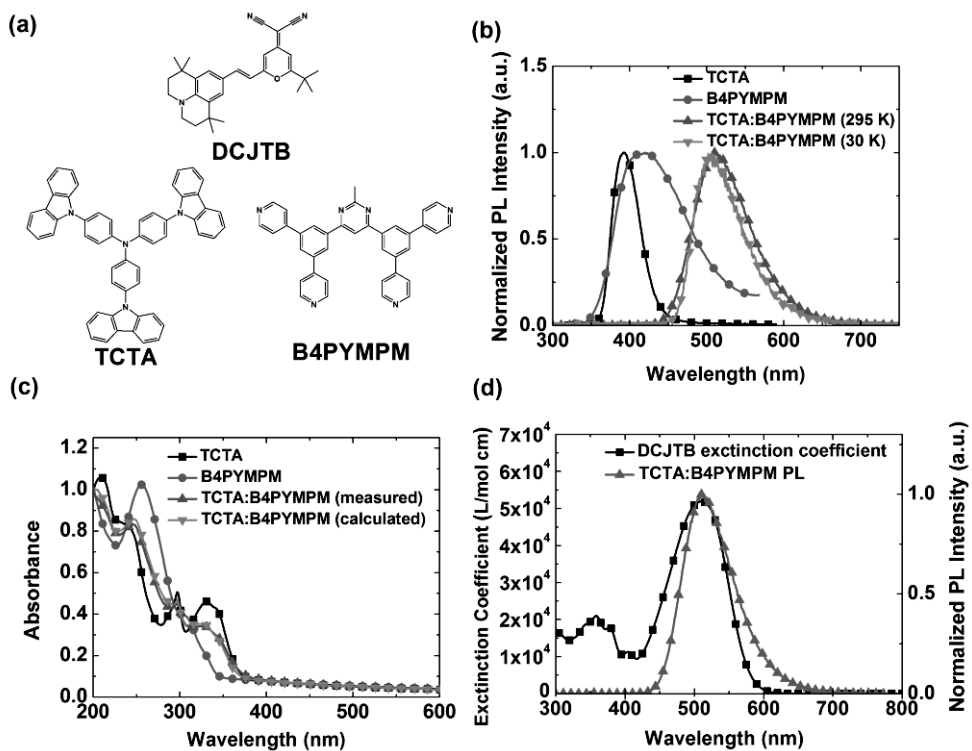


Figure 3.1 (a) Chemical structures of host and red fluorescent dopant and (b) PL spectra of TCTA, B4PYMPM, and TCTA:B4PYMPM at 295 K and delayed PL spectrum of TCTA:B4PYMPM after 10 μ s at 30 K. (c) Absorption spectra of TCTA, B4PYMPM, and mixed TCTA:B4PYMPM films. The absorption spectrum of the mixed TCTA:B4PYMPM film is the same as the weighted addition of the TCTA and B4PYMPM absorption spectra. (d) The molar extinction coefficient of the DCJTJTB and normalized PL spectra of TCTA:B4PYMPM film, exhibiting large spectral overlap between them.

mixed film. The extinction coefficient of the DCJTB in methylene chloride and the emission spectrum of the exciplex are displayed in Figure 3.1d, exhibiting excellent spectral overlap between them to allow efficient energy transfer from the exciplex to the dopant. The calculated Förster energy transfer radius from the exciplex to DCJTB was 4.5 nm.⁷⁰

The PL spectrum of the TCTA:B4PYMPM mixed film doped with DCJTB (0.5 wt%) is shown in the inset of Figure 3.2a. The peak wavelength was 596 nm and the PL quantum yield was $73 \pm 2\%$. The transient PL intensity at 600 nm (Figure 3.2a) exhibited long delayed emission with the PL lifetime of 190 ns. In contrast, DCJTB doped in Alq₃ host did not show the delayed PL. The difference in the transient behavior between the two systems clearly indicates that the delayed PL originates from the RISC of the triplet exciplex of the host, not from the TTA. The Förster energy transfer from the triplet exciplex to the singlet exciton of DCJTB was not considered as an origin of the delayed fluorescence because of the lack of the oscillator strength of the triplet exciplex.

Angle dependent PL intensity of the p-polarized light from the TCTA:B4PYMPM: 0.5 wt% DCJTB film was measured to determine the orientation of the emitting dipoles of the DCJTB in the exciplex host and the result is shown in Figure 3.2b.^{7,17,24,59} The angle dependent PL intensity at 600 nm was analyzed using the classical dipole model where the emission from excitons is considered as the dissipated (or radiating) power from oscillating dipoles. The experimental data were fitted very well with the ratio of horizontal dipoles (Θ) of 0.86 as shown in Figure 3.2b with the uncertainty of ± 0.02 , indicating that the emission dipoles of the red

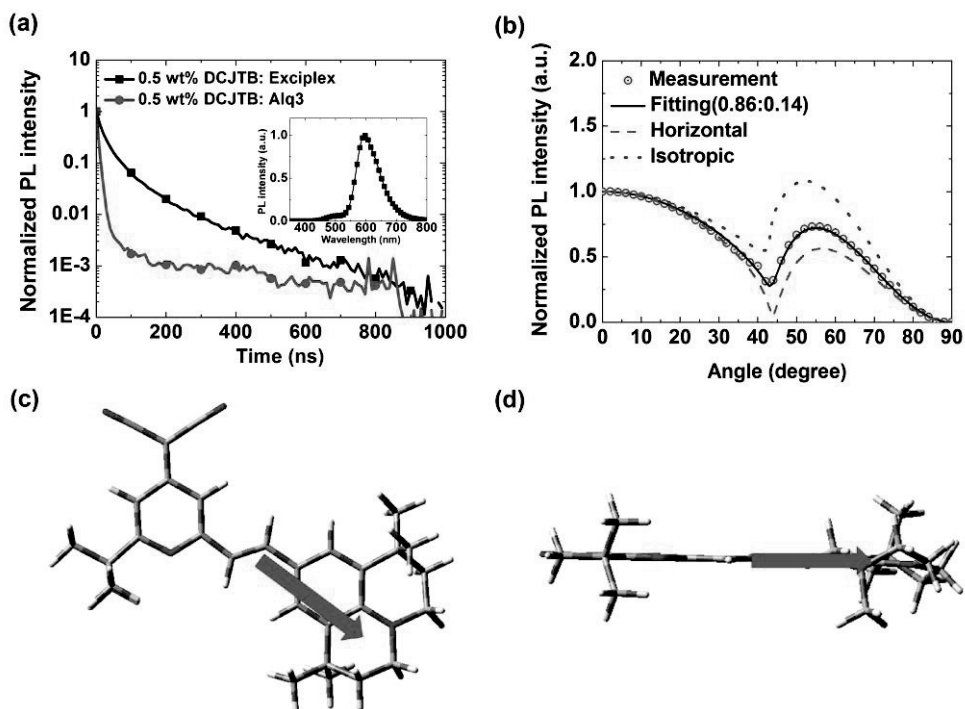


Figure 3.2 (a) Normalized intensity of transient PL of TCTA: B4PYMPM: 0.5 wt% DCJTB film and Alq₃:0.5 wt% DCJTB film (inset: PL spectrum of 0.5 wt% DCJTB doped in exciplex host). (b) Angle dependent PL intensity of the p-polarized light from the 30 nm thick TCTA: B4PYMPM: 0.5 wt% DCJTB film at 600 nm. (c) Top view of TDM on optimized structure of DCJTB. (d) Side view of TDM on optimized structure of DCJTB.

fluorescent dyes are preferentially oriented along the horizontal direction (parallel to the substrate). In order to identify the molecular orientation of DCJTB in EML, the direction of transition dipole moment (TDM) from the S_1 to S_0 state in DCJTB was calculated by using the time dependent DFT calculation (Figure 3.2c,d). The direction of TDM was toward julolidine (donor) from pyran (acceptor) in the plane of molecule. The high horizontal portion of the emission dipole and the inplane direction of the TDM in DCJTB indicates that DCJTB molecules are preferentially oriented along the horizontal direction in the film.

We fabricated the OLEDs using the DCJTB doped exciplex host as the EML. The structure of the OLED was as follows: indium tin oxide (ITO) (100 nm)/1,1-bis-(4-bis(4-methylphenyl)-amino-phenyl)-cyclohexane (75 nm)/TCTA (10 nm)/TCTA:B4PYMPM: x wt% DCJTB (30 nm)/B4PYMPM (50 nm)/LiF (0.7 nm)/Al (100 nm). TCTA and B4PYMPM were employed as the HTM and the ETM, respectively. The HTM and ETM were used as the cohost of the EML with the molar ratio of 1:1. The cohost facilitates the efficient charge injection from the electrodes to the EML due to absence of injection barrier of electrons (or holes) from the electron transporting layer (or hole transporting layer) to EML. The current density-voltage-luminance ($J-V-L$) characteristics of OLEDs for different DCJTB doping concentrations are shown in Figure 3.3a. All the devices exhibited the similar $J-V$ characteristics with the turn on voltage of 2.4 V, indicating that the bimolecular recombination on host molecules is dominant in this system rather than the direct exciton formation on DCJTB. The electroluminescent (EL) spectra are shown in Figure 3.3b. The peak wavelengths of the EL spectra were shifted from 600 nm for

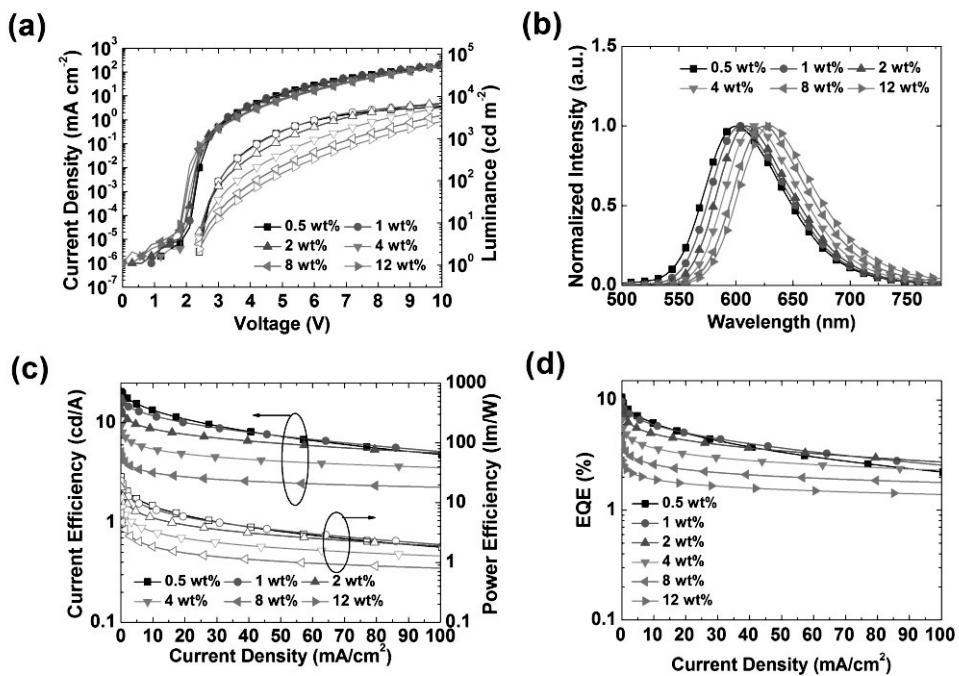


Figure 3.3 (a) The $J-V-L$ curves of the OLEDs. (b) The normalized EL spectra of devices at 10 mA/cm^2 . (c) The current efficiencies and power efficiencies against current density. (d) The EQEs against current density.

the doping concentration of 0.5 wt% to 632 nm for the doping concentration of 12 wt% due to the substantial aggregation of DCJTB.⁷¹ Less appearance of host emission in the EL spectrum of the 0.5 wt% DCJTB device than the PL spectrum indicates that direct exciton formation on DCJTB by trap-assisted recombination plays a role along with the energy transfer in the device. Further study is required to identify the exact mechanism. The EQE, power efficiency (PE), and current efficiency (CE) of the OLEDs are shown in Figure 3.3c,d. The EQE and PE of OLEDs were calibrated using the angle dependent emission profiles. The device with the doping concentration of 0.5 wt% exhibited the highest EQE of 10.6%, PE of 26.8 lm/W, and CE of 20.5 cd/A. To the best of our knowledge, the EQE of 10.6% is much higher than the fluorescent OLEDs (3%–6%) reported up to now using DCJTB as an emitter.⁶⁵⁻⁶⁸ Lower efficiency of the OLEDs at high doping concentrations might originate from the concentration quenching (low PL quantum yields) as well as increasing Dexter energy transfer from the triplet exciplex to the triplet state of dopant.

To understand the high EL efficiency of the device, the fraction of the radiative exciton of DCJTB was calculated using the measured Θ of 0.86 and PL quantum yield of 0.73 under the assumption of no electrical loss.^{7,24,59} The classical dipole model was employed for the calculation using the experimental parameters with the consideration of the modification of the radiative decay rate in the microcavity structure (the Purcell factor). The calculated fraction of the radiative exciton in the device was 35.1%, indicating that extra 10.1% of the excitons were converted from the triplet states to the singlet excitons through the RISC of the triplet

exciplex to the singlet exciplex in the device. Up-conversion from the triplet to singlet on DCJTB is hardly probable because of the large energy gap of 0.35 eV between T_1 state and S_1 state of DCJTB.⁷² To manifest the mechanism of the delayed emission of the OLED, the transient EL decays at various current densities were measured (Figure 3.4a). The intensity of the delayed EL emission of the OLED was linearly proportional to the current density, indicating that the delayed emission of the OLED originates from RISC not from TTA (Figure 3.4b).

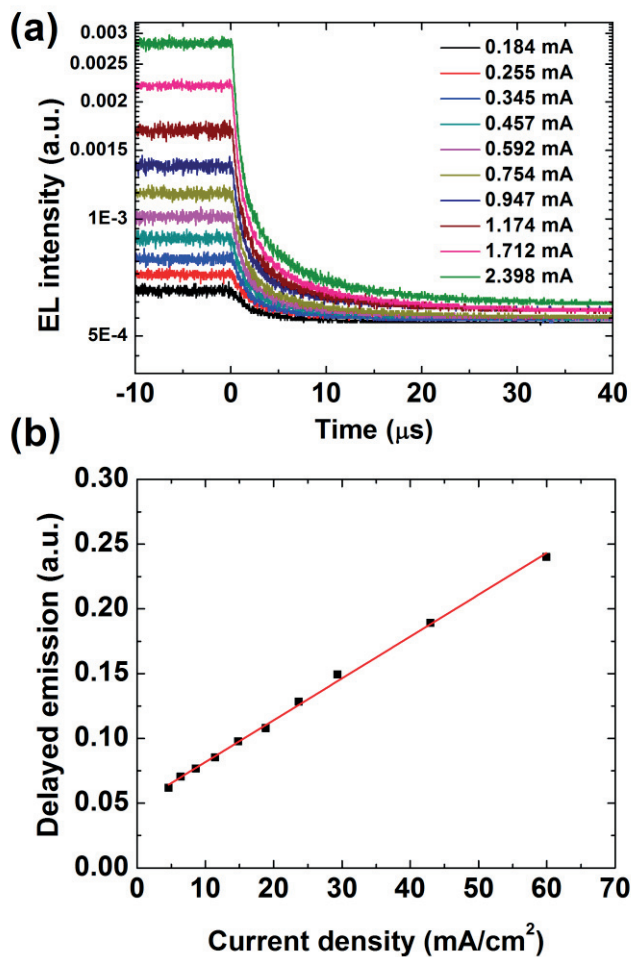


Figure 3.4 (a) Transient EL intensity of device at various current level. The wavelength of detection is 605 nm. The voltage pulse width was 100 μs , and the pulse was periodically applied to the devices with a frequency of 100 Hz. (b) Initial intensity of delayed emission against current density.

3.4 Conclusion

In conclusion, we report a red fluorescent OLED with unprecedented high EQE of 10.6% using DCJTB as an emitter doped in an exciplex forming host. Analysis indicated that the fraction of the radiative exciton formed on DCJTB was 35.1%, indicating that extra 10.1% of the singlet excitons were formed by the RISC of the triplet exciplex to the singlet exciplex followed by the energy transfer to DCJTB. Further study is required to identify the exact mechanism.

Chapter 4. Highly efficient organic light-emitting diodes with phosphorescent emitters having high quantum yield and horizontal orientation of transition dipole moments

4.1 Introduction

Orientation of the transition dipole moments of an emitter is an important factor influencing the effective quantum efficiency and the outcoupling efficiency in OLEDs. Horizontally oriented dipoles result in higher outcoupling efficiency than vertically oriented dipoles.^{12,13} Not only fluorescent molecules but also some phosphorescent molecules were reported to have preferred horizontal orientation in OLEDs to improve the outcoupling efficiency over the limit set under the assumption of the isotropic or random orientation of the molecules.^{7,17-20} However, the factors influencing the orientation of the phosphorescent dyes in phosphorescent OLEDs have not been reported yet. Here, we report that the ancillary ligands in heteroleptic iridium complexes significantly influence the orientation of the transition dipole moments. In addition, we demonstrate an unprecedented highly efficient green OLED exhibiting the external quantum efficiency (EQE) of 32.3% and power efficiency of 142.5 lm/W using an emitter with high quantum yield and horizontally oriented dipoles.

4.2 Experimental

Organic materials were purchased from Daejoo Electronic Materials and Luminescence Technology Corp., and LiF from Materion.

The OLEDs were fabricated on clean glass substrates pre-patterned with 70-nm-thick indium tin oxide (ITO) under a pressure of 5×10^{-7} Torr by thermal evaporation without breaking the vacuum. Before the deposition of organic layers the ITO substrates were pre-cleaned with isopropyl alcohol and acetone, and then exposed to ultraviolet-ozone for 10 min. The devices had the following structure: ITO (70 nm)/1,1-bis-(4-bis(4-methylphenyl)-amino-phenyl)-cyclohexane (TAPC) (75 nm)/4,4',4''-tris(N-carbazolyl)-triphenylamine (TCTA) (10 nm)/TCTA:bis-4,6-(3,5-di-3-pyridylphenyl)-2-methylpyrimidine (B3PYMPM): green dopants [tris(2-phenylpyridine) iridium(III) ($\text{Ir}(\text{ppy})_3$), bis(2-phenylpyridine)iridium(III)acetylacetonate ($\text{Ir}(\text{ppy})_2\text{acac}$), bis(2-phenylpyridine)iridium(III)(2,2,6,6-tetramethylheptane-3,5-diketonate) ($\text{Ir}(\text{ppy})_2\text{tmd}$)] (30 nm, 8.4 mol%)/B3PYMPM (45 nm)/LiF (0.7 nm)/Al (100 nm). Each layer was deposited at a rate of 1 Å/s and the deposition rate of the co-deposited layers was 1 Å/s in total.

Current density, luminance, and electroluminescent (EL) spectra were measured using a programmable source meter (Keithley 2400) and a spectrophotometer (Spectrascan PR650, Photo Research). The angular distribution of the EL was measured with a programmable source meter (Keithley 2400), goniometer, and fiber optic spectrometer (Ocean Optics S2000). The EQE and the

power efficiency of the OLEDs were calculated from current density–voltage–luminance characteristics, EL spectra, and the angular distribution of the EL intensity.

Orientation of transition dipole moments was measured using a continuous wave diode laser (405 nm, Edmund optics Inc.). The incident angle of the excitation source was fixed at 45°. P-polarized emitted light was detected at 520 nm that is close to the peak wavelength of the PL spectra of the phosphorescent dyes.

Permanent dipole moment of dyes was calculated using the density functional theory (DFT) with Gaussian09.⁶⁴ Ground state geometry optimization was performed using the B3LYP exchange-correlation functional, the LANL2DZ basis set for Ir atom, and the 6-311G(d) basis set for all other atoms.

4.3 Result and discussion

Chemical structures of green-emitting dopants used in this study are presented in Figure 4.1a. We used Ir(ppy)₃, Ir(ppy)₂acac, Ir(ppy)₂tmd as green-emitting dopants.⁷³ They have the same cyclometalated ligand but different ancillary ligands. Schematic diagram of the device structure of the OLEDs is shown in Figure 4.1b. The devices have a simple structure consisting of three organic materials and phosphorescent dopants.^{7,30,31} TAPC was used as the hole injection layer, TCTA as the hole transporting layer (HTL) and B3PYMPM as the electron transporting layer (ETL). TCTA and B3PYMPM were also used as the co-host of the emitting layer (EML) with the molar ratio of 1:1 to exploit the exciplex forming character for low driving voltage, and good electron-hole balance.^{7,30,31} The detailed structure of the OLEDs is; ITO (70 nm)/TAPC (75 nm)/TCTA (10 nm)/TCTA:B3PYMPM:8.4 mol% dye (30 nm)/B3PYMPM (45 nm)/LiF (0.7 nm)/Al (100 nm).

The photoluminescence (PL) spectra of the TCTA:B3PYMPM co-host films doped with the three dyes with the doping concentration of 8.4 mol% are shown in Figure 4.2a. The peak wavelength of the PL of Ir(ppy)₃, Ir(ppy)₂acac, and Ir(ppy)₂tmd were 513 nm, 520 nm, 524 nm, respectively. The orientations of the transition dipole moments of the dyes in the host were determined through the analysis of the angle dependent PL spectra of the films.^{7,17} Figure 4.2b shows the measured angle-dependent PL intensities of the p-polarized light emitted from the 30 nm-thick films composed of TCTA:B3PYMPM:green dyes (0.46:0.46:0.08 molar ratio) at 520 nm close to the PL maxima of the green dyes. The angle dependent PL

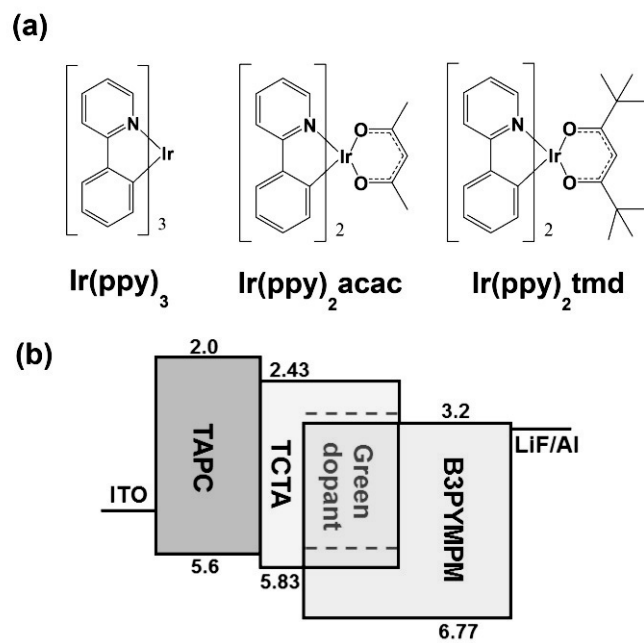


Figure 4.1 (a) Molecular structure of green phosphorescent dyes and (b) schematic diagram of the device structure and energy levels (eV) of the devices.

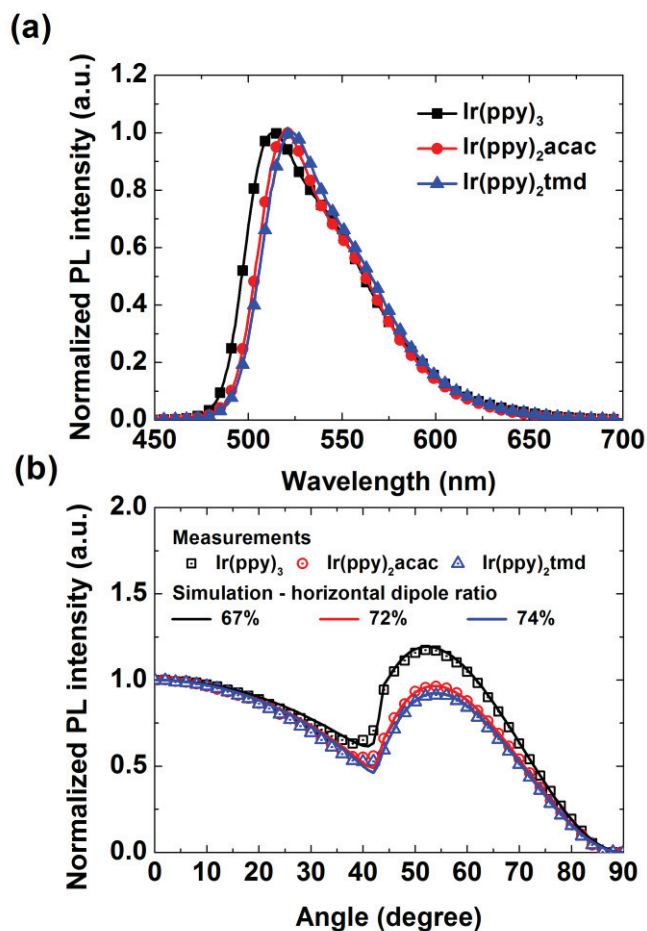


Figure 4.2 (a) The PL spectra of the 8.4 mol% Ir(ppy)₃, Ir(ppy)₂acac, and Ir(ppy)₂tmd doped TCTA:B3PYMPM films. (b) Angle-dependent PL intensities of the p-polarized light from the 30-nm-thick films composed of TCTA:B3PYMPM:green dyes (0.46:0.46:0.08 molar ratio) at 520 nm. Solid lines represent theoretical fits to the experimental data.

spectra were analyzed using the classical dipole model where the emission from excitons is considered as the dissipated power from oscillating dipoles.^{24,59} Birefringence of the films composed of TCTA:B3PYMPM:green dyes was considered in the theoretical fittings. The experimental data were well fitted by the horizontal-dipole ratios (Θ 's) of 0.67 for Ir(ppy)₃, 0.72 for Ir(ppy)₂acac, and 0.74 for Ir(ppy)₂tmd with an uncertainty of 0.02, where Θ was defined as the ratio of the horizontal dipoles to the total dipoles of an emitter. Ir(ppy)₃, a homoleptic Ir complex, exhibited isotropic dipole orientation, whereas, the heteroleptic Ir complexes of Ir(ppy)₂acac and Ir(ppy)₂tmd showed preferred dipole orientation in the horizontal direction, indicating that the structure of the ancillary ligands in the Ir complexes strongly affects the orientation of the transition dipole moment of the emitters. Different ancillary ligands will give rise to different molecular structures and resultantly different orientations of transition dipole moments which are related to the relative position of the Ir atom and the main ligands even though ancillary ligands are not involved in the transition. In contrast, the symmetry of homoleptic Ir complexes with three main ligands has an effect of randomization of the orientation of the transition dipole moments in the molecules.

The photoluminance quantum yields (q_{PL}) of the EMLs were directly measured by using 50 nm thick films on quartz substrates in an integration sphere. The q_{PL} 's of the TCTA:B3PYMPM co-hosts doped with 8.4 mol% Ir(ppy)₃, Ir(ppy)₂acac, and Ir(ppy)₂tmd were $92 \pm 1\%$, $94 \pm 1\%$, and $96 \pm 1\%$, respectively. The q_{PL} 's of the dopants in the low doping concentration of 2 mol% were almost 100% (Figure 4.3). Therefore the difference in the q_{PL} 's among the dopants at the doping

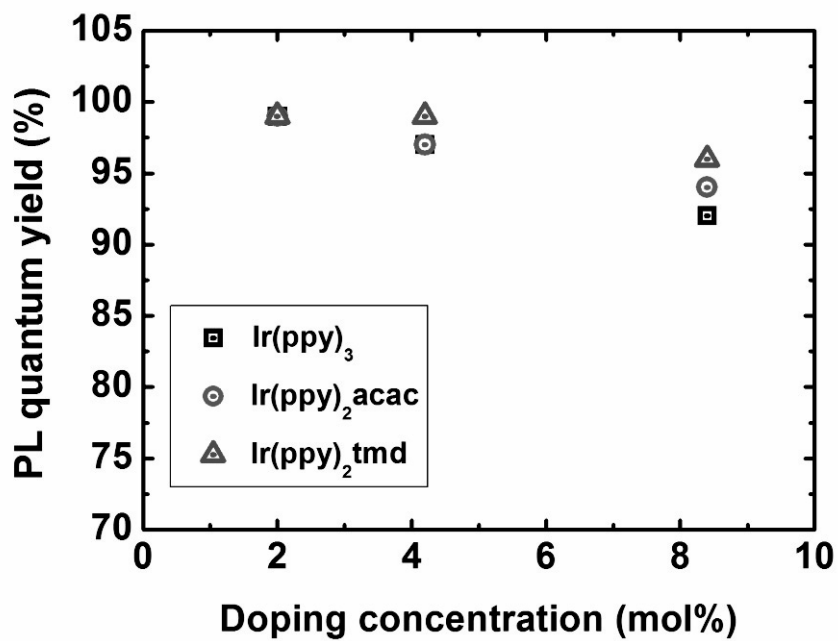


Figure 4.3 PL quantum yields at doping concentrations of 2, 4.2, and 8.4 mol % of dyes in TCTA:B3PYMPM (1:1) co-host.

concentration of 8.4 mol% must be related to concentration quenching.⁷⁴ Higher q_{PL} 's of the heteroleptic Ir complexes might originate from their lower permanent dipole moments (μ 's). Increase in μ seems to result in strengthening the intermolecular interaction and consequently increase in degree of aggregation and concentration quenching. DFT calculations of the ground state of the emitters showed the permanent dipole moment of 6.2, 1.8, and 1.4 debyes for Ir(ppy)₃, Ir(ppy)₂acac, and Ir(ppy)₂tmd, respectively. The molecule Ir(ppy)₃ with the highest μ showed the lowest q_{PL} and the molecule Ir(ppy)₂tmd with the lowest μ showed the highest q_{PL} among the three dyes, supporting the correlation between the PL quantum yield and the permanent dipole moments of the phosphorescent dyes. The high Θ combined with high q_{PL} of Ir(ppy)₂tmd is expected to give a high EQE from the OLED doped with the dye. Higher q_{PL} can be obtained if the doping concentration of the dyes is lowered in the EMLs. However, the energy transfer from the co-host molecules to the dopants becomes insufficient if the doping concentration is lowered too much so that we used the doping concentration of 8.4 mol% to maximize the EQEs as reported in our previous report.³⁰

The current density-voltage-luminance (J - V - L) characteristics of the OLEDs doped with Ir(ppy)₃, Ir(ppy)₂acac, and Ir(ppy)₂tmd are presented in Figure 4.4a. The OLEDs doped with the heteroleptic Ir complexes showed the same J - V characteristics with the turn on voltage of 2.4 V but the device doped with Ir(ppy)₃ showed higher turn on and driving voltages, indicating that the J - V characteristics are influenced not only by the host but also by the dopants. All the EL spectra of the OLEDs with green dyes in the EML were well consistent with the PL spectra of the

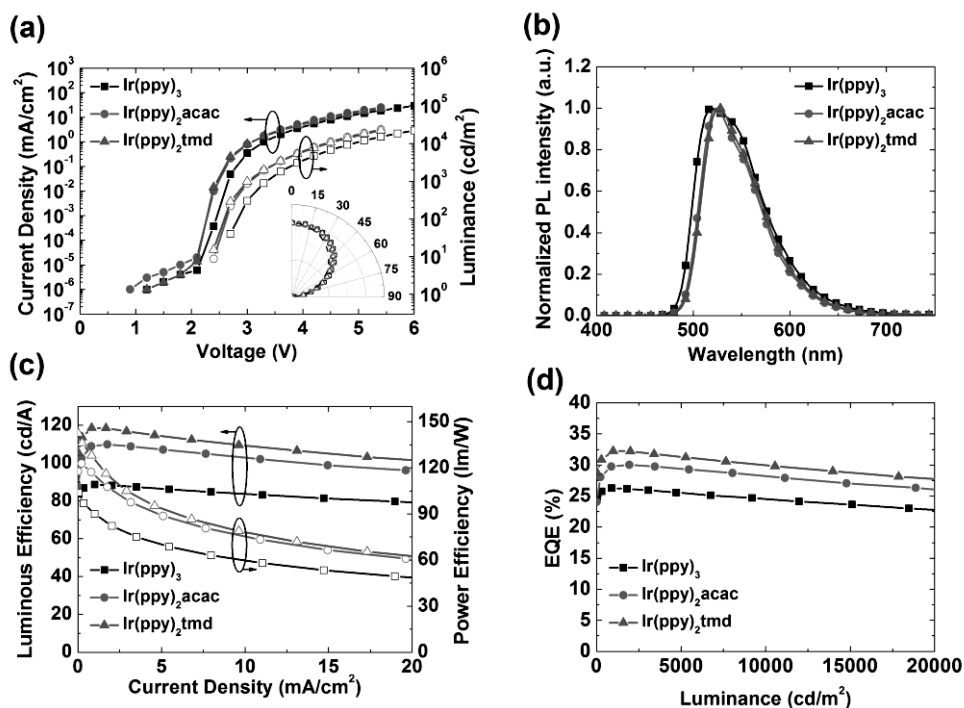


Figure 4.4 (a) The current density–voltage–luminance curves of the OLEDs. Inset: The angular distributions of the EL intensity of the OLEDs. The dashed line in the inset shows the Lambertian distribution. (b) The normalized EL spectra of the OLEDs. (c) Luminous efficiencies and power efficiencies against the luminance. (d) EQE's against the luminance. The EQE's and the power efficiencies of the devices were calibrated using the angle-dependent emission intensity profiles.

dyes doped in the co-host (Figure 4.4b). The EQE and the power efficiency of the devices calibrated using the angle-dependent emission intensity profiles are displayed in Figure 4.4c,d. The optimized device with an ETL with a thickness of 45 nm showed 26.3% for Ir(ppy)₃, 30% for Ir(ppy)₂acac, and 32.3% for Ir(ppy)₂tmd, respectively. The EQE of 32.3% is the highest efficiency reported to date for green OLEDs.^{7,30,75,76} The efficiency roll-off was also very small with the EQE of 32.3% at 1000 cd/m² and 30.0% at 10,000 cd/m² for the OLED doped with Ir(ppy)₂tmd. The high EQE combined with low driving voltage results in high power efficiency with the maximum of 104.0 lm/W for Ir(ppy)₃, 122.8 lm/W for Ir(ppy)₂acac, and 142.5 lm/W for Ir(ppy)₂tmd in the optimized devices, respectively. The larger difference in the power efficiencies than the EQEs among the devices comes from the difference in their emission spectra. The low driving voltage of the devices can be explained by the existence of no injection barriers for the charges from the charge transporting layers to the EML. The low efficiency roll-off comes from the exciplex forming co-host by lowering the carrier density in the EML to reduce the triplet-polaron quenching and by lowering the triplet-triplet annihilation due to the broad emission zone.³⁰

The maximum EQEs of the OLEDs achievable using the dyes were simulated using the classical dipole model based on the measured Θ and q_{PL} .^{7,24,59} We used the device structure shown in Figure 4.1b for the simulation, and the recombination zone was assumed to be located in the middle of the EML. The maximum EQE can be obtained by assuming the perfect electron and hole balance. The calculated maximum EQEs of the devices doped with Ir(ppy)₃, Ir(ppy)₂acac, and Ir(ppy)₂tmd

dyes were $25.9 \pm 1\%$, $30.5 \pm 1\%$, and $32.0 \pm 1\%$, respectively, and are well consistent with the measured maximum EQEs of the devices with Ir(ppy)_3 , $\text{Ir(ppy)}_2\text{acac}$, and $\text{Ir(ppy)}_2\text{tmd}$ indicating that all the injected charges form excitons in the device (Table 4.1).

Table 4.1 Photoluminescence quantum yield and horizontal portion of transition dipole moments of three different phosphorescent dyes, and experimentally obtained EQEs of the OLEDs doped with three different phosphorescent dyes compared with the calculated EQEs using the classical dipole model under the assumption of perfect electron and hole balance in the devices.

Dyes	PL quantum yield (q_{PL})	Horizontal dipole ratio (Θ)	EQE of device (%)	Calculated EQE (%)
Ir(ppy) ₃	0.92	0.67	26.3	25.9
Ir(ppy) ₂ acac	0.94	0.72	30.0	30.5
Ir(ppy) ₂ tmd	0.96	0.74	32.3	32.0

4.4 Conclusion

In summary, we found that the ancillary ligand of phosphorescent dyes significantly influences the dipole orientation and Ir(ppy)₂tmd with the ancillary ligand of 2,2,6,6-tetramethylheptane-3,5-diketonate resulted in high horizontal dipole ratio of 74% along with high q_{PL} of 96%. Using the Ir(ppy)₂tmd as the dopant, we could realize a bottom emission OLED with the maximum EQE of 32.3% and the maximum power efficiency of 142.5 lm/W, the highest values ever reported in literature. Furthermore we experimentally and theoretically correlated the EQE of OLEDs to the q_{PL} and the horizontal dipole ratio of phosphorescent dyes using three different dyes.

Chapter 5. Phosphorescent dye-based supramolecules for high-efficiency organic light-emitting diodes

5.1 Introduction

The efficiency of light emission from organic light-emitting diodes (OLEDs) is one of their most important characteristics, along with emission colour and lifetime, because it is directly related to power consumption and device longevity. External quantum efficiencies (EQEs) of 30% have been reported recently^{7,11,30,75-77}; this is considered to be the light-outcoupling efficiency limit of phosphorescent OLEDs under isotropically oriented transition dipole moments⁴. It has long been recognized that orienting the transition dipole moment of an emitter along the horizontal direction (parallel to the substrate) can enhance the outcoupling efficiency beyond that achieved under isotropic orientation, as demonstrated in polymer-based and vacuum evaporated fluorescent molecule-based OLEDs.^{12-17,22} Nonetheless, the orientation of the transition dipole moments of iridium complexes used as phosphorescent emitters in efficient OLEDs is typically considered to be isotropic because they are near-globular and small enough to have configurational diversity in their orientational states. Therefore, it is believed that the theoretical EQE limit of phosphorescent OLEDs is 30%. Recently, however, some heteroleptic iridium complexes (HICs) have been reported to have transition dipole moments oriented preferentially along the horizontal direction.^{7,18-20} This implies that it may be possible

to exceed the efficiency limit of 30% under isotropic orientations of the emitting dipoles. Unfortunately, the origin of the preferred orientation of some phosphorescent dyes is not fully understood, and OLEDs with an EQE over 30% have not yet been demonstrated using oriented phosphorescent dyes.

In this article, we use quantum chemical calculations to show that the heteroleptic structure and the strong intermolecular interactions between HICs and their host molecules lead to preferred dipole orientations in the HICs. We demonstrate an unprecedentedly high EQE of 35.6% for red-emitting HICs with triplet transition dipole moments oriented along the horizontal direction.

5.2 Experimental

Materials. Materials (>99%) were purchased from Furuya Metals (Tokyo, Japan) and Nichem Fine Technology Co., Ltd (Hsinchu County, Taiwan). The energy levels of the organic materials were obtained from the literature³⁰, except for those of N,N'-di(naphthalen-1-yl)-N,N'-diphenylbenzidine (NPB). The highest occupied molecular orbital (HOMO) level of NPB was measured using cyclic voltammetry. The lowest unoccupied molecular orbital (LUMO) level of NPB was estimated using the HOMO level and the optical band gap from its absorption spectrum.

Photoluminescence (PL) measurements. PL spectra of the organic materials were measured using samples thermally deposited on fused silica under a vacuum of $<5 \times 10^{-7}$ Torr. The samples were excited with a He/Cd laser (325 nm) to detect PL using a photomultiplier tube attached to a monochromator.

Device fabrication. The OLEDs were fabricated on clean glass substrates prepatterned with 100-nm-thick indium tin oxide (ITO) under a pressure of 5×10^{-7} Torr by thermal evaporation without breaking the vacuum. Before the deposition of the organic layers, the ITO substrates were pre-cleaned with isopropyl alcohol and acetone, then exposed to ultraviolet-ozone for 10 min. The devices had the following layer structure: ITO (100 nm)/1,1-bis((di-4-tolylamino)phenyl)cyclohexane (TAPC) (75nm)/NPB (10nm)/NPB:bis(4,6-(3,5-di-(3-pyridyl)phenyl))-2-methylpyrimidine (B3PYMPM): red dopants tris(2-phenylquinoline)iridium(III) $[\text{Ir}(\text{phq})_3]^{78}$, (bis(2-(3,5-dimethylphenyl)quinoline)Ir(III)(acetylacetonate) $[\text{Ir}(\text{mphq})_2\text{acac}]^{79}$, bis(2-methyldibenzo-[f,h]-quinoxaline)Ir(III)(acetylacetonate) $[\text{Ir}(\text{MDQ})_2\text{acac}]^{80}$, (bis(4-

methyl-2-(3,5-dimethylphenyl)quinoline))Ir(III)(tetramethylheptadionate)

[Ir(mphmq)₂tmd]⁷⁹ (30nm, 3.5 mol%)/B3PYMPM (10nm)/B3PYMPM:Rb₂CO₃ (45 nm, 2 wt%)/Al (100nm). Each layer was deposited at a rate of 1Å/s, and the deposition rate of the co-deposited layers was 1Å/s in total.

Device characterization. The current density-voltage-luminance (*J-V-L*) and electroluminescent (EL) spectra were measured using a programmable source meter (Keithley 2400) and a spectrophotometer (Spectrascan PR650, Photo Research). The angular distribution of the EL was measured with a programmable source meter (Keithley 2400), a goniometer, and a fiber optic spectrometer (Ocean Optics S2000). The EQE and the power efficiency of the OLEDs were calculated from their *J-V-L* characteristics, their EL spectra and the angular distribution of the EL intensity.

Measurement and calculation of angle-dependent PL spectra. The dipole orientations in the red dyes in the birefringent NPB:B3PYMPM co-host were determined by analysing the angle-dependent PL of the film using the classical dipole model.^{17,18,24,57,81} This model allows for the separate calculation of the p- and s-polarized light emission from horizontally and vertically oriented dipoles in a non-absorbing anisotropic medium. According to the dipole model, the horizontally and vertically oriented dipoles, p_x and p_z , emit p-polarized light, whereas the other horizontally oriented dipole, p_y , emits s-polarized light. The angle-dependent emission intensity of the p-polarized light is significantly different for the p_x and p_z dipoles, allowing the proportion of horizontal dipoles to be determined by fitting the simulated p-polarized intensity for various ratios of p_x and p_z to the experimental data. Using this method, the ratio of horizontal ($P_{\parallel} = p_x + p_y$) to vertical ($P_{\perp} = p_z$)

dipoles can be evaluated. The refractive index of the optically anisotropic NPB:B3PYMPM layer was measured by variable angle spectroscopic ellipsometry (VASE). The incident angle was varied from 45° to 75° in steps of 5°.

The experimental setup has been reported previously^{7,17} and was composed of a motorized rotation stage, a half cylinder lens with a sample holder, a dichroic mirror to filter the excitation beam, a polarizer to select the polarization of the emitted light and a fiber optic spectrometer (Ocean Optics Maya2000). A He-Cd continuous wave laser (325 nm) was used as the excitation source. NPB:B3PYMPM films (30-nm thick) doped with 3.5 mol% red dye, which were thermally deposited on a 1-mm-thick fused silica substrate and encapsulated under N₂ atmosphere before use, were used for the angle-dependent PL measurements. P-polarized light was used to analyse the orientation of the dipoles in the films.

Simulation of the outcoupling efficiency of the OLEDs. The outcoupling efficiency of the devices was evaluated using the obtained dipole orientations. The device structure used to calculate the outcoupling efficiency was ITO (100 nm)/TAPC (75 nm)/NPB (10 nm)/NPB:B3PYMPM:Ir(mphmq)₂tmd (30 nm)/B3PYMPM (x nm)/Al (100 nm). The thickness (x nm) of the B3PYMPM layer was varied from 0 to 200 nm. The method has been described in detail elsewhere.^{11,81} The refractive indices of the organic materials were measured by VASE, and those of ITO and Al were obtained from the literature.^{82,83} The refractive index of the glass substrates (Corning Incorporated Eagle 2000) was taken from the manufacturer. The influence of the dopant on the refractive index of the emitting layer (EML) was ignored because of the low doping concentration used.

Density functional theory (DFT)/time dependent-DFT (TD-DFT) calculations on the iridium phosphorescent dyes. Quantum chemical calculations based on DFT were carried out using Gaussian 09 program.⁶⁴ An *N,N*-trans structure was used as the starting geometry. The ground state and triplet-state geometry optimization were performed using Becke's three-parameter B3LYP exchange-correlation functional⁸⁴⁻⁸⁶, the 'double- ξ ' quality LANL2DZ basis set for the Ir atom, and the 6-311+G(d,p) basis set for all other atoms. A pseudo potential (LANL2DZ) was applied to replace the inner core electrons of the Ir atom, leaving the outer core [(5s)2(5p)6] electrons and the (5d)6 valence electrons. For the TD-DFT calculations, the unrestricted uB3LYP functional and the same basis sets used for geometry optimization were applied to the optimized geometry. The 20 lowest singlet and triplet states were calculated and analysed. The transition dipole moments of the triplet states were calculated using the Dalton 2011 program with a quadratic response function and the 6-31G(d) basis set for C, H; the 6-311G(d) basis set for N, O; and the Stuttgart ECP basis set for Ir in the TD-DFT calculations. Structure optimization and the Kohn-Sham orbitals were calculated using the Gaussian 09 program⁶⁴, while the triplet transition dipole moments were calculated using the Dalton 2011 programme.⁸⁷

To efficiently identify the binding geometry between the host and the dopant, the calculations for the electrostatic potential (ESP) map, which suggests plausible binding sites for the hosts and dopants by scanning the partial charge distributions on the molecular skeletons of each host and dopant molecule, were performed using the ESP method by Singh and Kollman.⁸⁸ The DFT geometry optimizations were

then performed with the initial geometries, where the host and dopant were placed near the binding space suggested by the ESP map of each molecule. For the DFT computations, the Perdew–Burke–Ernzerhof⁸⁹ exchange–correlation functional was used using DMol3 in Materials Studio.^{90,91} The electronic configurations were described by the double numerical basis set and the polarization basis set under an ECP. The optimization convergence thresholds for energy change, maximum force and maximum displacement were 0.00001 Ha, 0.002 Ha/Å and 0.005 Å, respectively.

5.3 Result and discussion

5.3.1 Materials for OLEDs

The red-emitting HICs Ir(mphq)₂acac⁷⁹, Ir(MDQ)₂acac⁸⁰ and Ir(mphmq)₂tmd⁷⁹ were used as phosphorescent emitters, and NPB and B3PYMPM were used as co-hosts for the fabrication of the OLEDs. A reference complex (fac-Ir(phq)₃)⁷⁸ with a homoleptic disposition of the ligands identical to those of Ir(mphq)₂acac was also prepared. The chemical structures of the red-emitting dyes and the host materials are presented in Figure 5.1a. The PL quantum yields (q_{PL} 's) of the EMLs were directly measured using 50-nm-thick films on quartz substrates in an integration sphere. The measured q_{PL} 's of the dyes were 0.71 for fac-Ir(phq)₃, 0.83 for Ir(mphq)₂acac, 0.82 for Ir(MDQ)₂acac and 0.96 for Ir(mphmq)₂tmd. The co-host system was selected to take advantage of its exciplex-forming characteristics because OLEDs containing an exciplex-forming co-host have an almost perfect electron-hole balance, low driving voltage and low efficiency rolloff.^{7,30,31,35} Figure 5.1b shows the PL spectra of vacuum-evaporated films of NPB and B3PYMPM and a co-evaporated film of NPB and B3PYMPM with a molar ratio of 1:1. The co-evaporated film exhibits featureless emission at 510nm that is red-shifted compared with those of its constituent materials. The peak wavelength is close to the energy difference between the energy levels of LUMO of B3PYMPM and HOMO of NPB, indicating that the co-host system efficiently forms exciplexes upon photoexcitation.

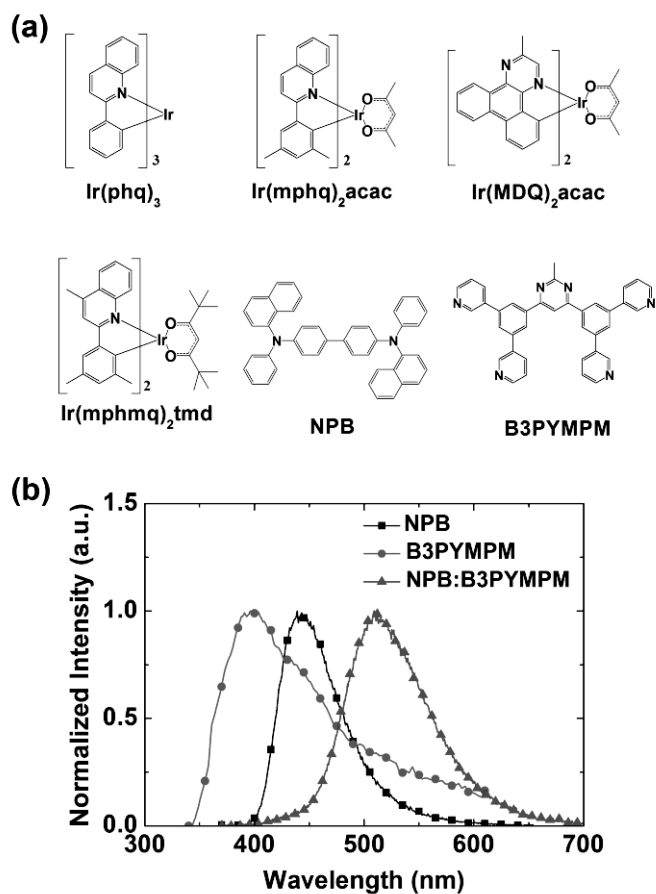


Figure 5.1 Material characteristics. (a) Molecular structures of the red phosphorescent dyes and the host molecules. (b) Normalized PL spectra of the NPB, B3PYMPM and mixed NPB:B3PYMPM films.

5.3.2 Orientations of transition dipole moments of the phosphorescent dyes

The orientations of the transition dipole moments of the red dyes in the mixed co-host films were determined by analysing the angle-dependent PL spectra of the films.^{7,17,18} The birefringence of the EML was considered in the theoretical fittings. Figure 5.2a shows the measured angle-dependent PL intensities of the p-polarized light emitted from the 30-nm-thick NPB:B3PYMPM:red dye (0.48:0.48:0.035 molar ratio) films at 605 nm, which are close to the PL maxima of the red emitters. The experimental data fit the horizontal transition dipole ratios (Θ 's) of 0.70 for fac-Ir(phq)₃, 0.77 for Ir(mphq)₂acac, 0.80 for Ir(MDQ)₂acac and 0.82 for Ir(mphmq)₂tmd with an uncertainty of $\pm 2\%$, where Y is defined as the ratio of the horizontal component of the transition dipole moments to the total transition dipole moments. Moreover, the angle-dependent PL spectra were well matched, with theoretical fittings at all wavelengths (Figure 5.2b). Fac-Ir(phq)₃, a homoleptic iridium complex, exhibited nearly isotropically oriented transition dipole moments, whereas the transition dipoles of the HICs were preferentially oriented along the horizontal direction, as manifested by the Θ values of over 0.75.

Two conditions should be satisfied to obtain transition dipole moments preferentially oriented in the horizontal direction in the red HIC-doped co-host films: (1) the HIC should have triplet transition dipole moments preferentially oriented along a specific direction and not have a combination of transition dipole moments with various orientations, and (2) the HIC molecule itself should have a preferred orientation with respect to the substrate, in such a way that the combination of both conditions leads to transition dipole moments that are parallel to the horizontal

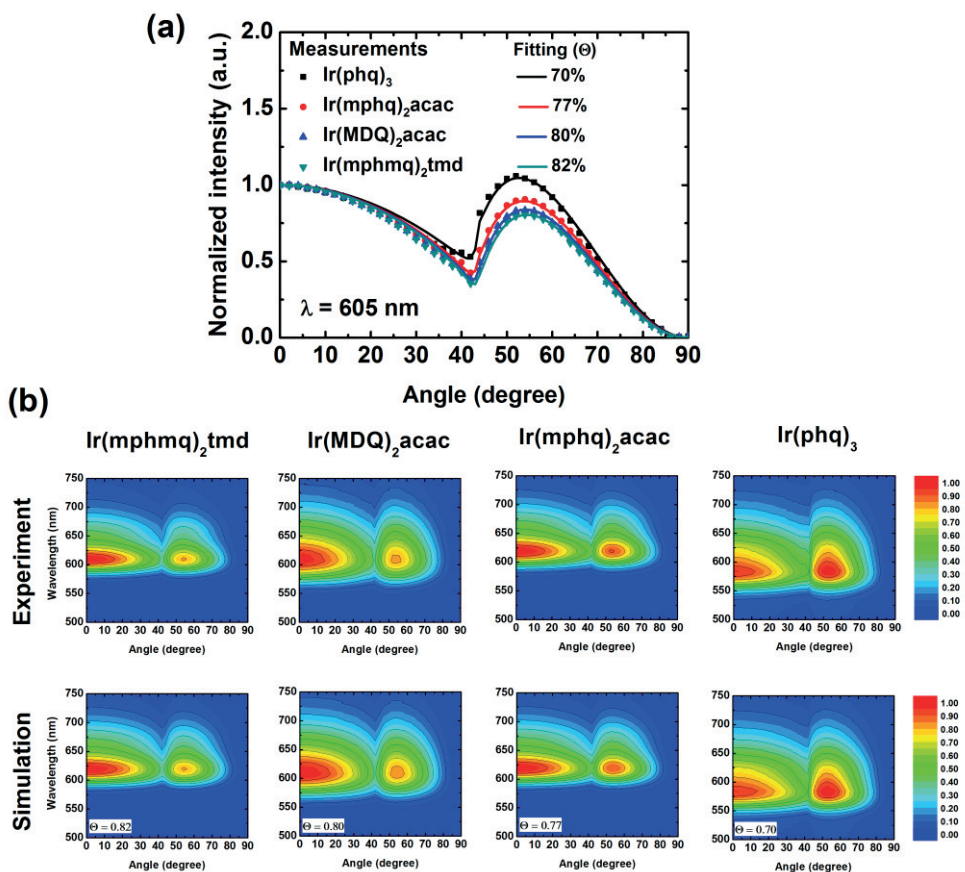


Figure 5.2 Analysis of the orientations of the transition dipole moments. (a) Angle-dependent PL intensities at 605nm and (b) angle-dependent PL spectra of p-polarized light from the 30-nm-thick NPB:B3PYMPM:red dye (0.5:0.5:0.035 molar ratio) film. The theoretical calculations fit the experimental data well.

direction. To determine the detailed mechanism for (1) and (2), molecular simulations were performed.

The triplet-state geometries of the red dyes were calculated using an unrestricted B3LYP level of theory without symmetry constraints. The triplet-state geometries of the HICs were found to possess a molecular C_2 axis that intersected the iridium core and the central carbon atom of the β -diketonate ancillary ligand. The pseudo octahedral geometry was completed by the remaining phenylato parts of the main ligands, which were located along the diagonal lines that cross the oxygen atom and the iridium core. In the case of fac-Ir(phq)₃, the triplet-state geometry adopted C_3 symmetry. Inspection of the Kohn–Sham orbitals revealed that the HOMO was distributed over the $d(t_{2g})$ -orbital of Ir(III) and the π -orbital of the phenylato moiety, whereas the LUMO was mainly localized in the π^* -orbital of the N-heterocycles (Figure 5.3a). Time-dependent DFT calculations were subsequently carried out for the optimized geometries to determine their adiabatic triplet transition energies, and these were found to be 1.81 eV for fac-Ir(phq)₃, 1.79 eV for Ir(mphq)₂acac, 1.86 eV for Ir(MDQ)₂acac and 1.83 eV for Ir(mphmq)₂tmd. In each case, the triplet transition mainly comprised an electronic transition from the HOMO to the LUMO with a configuration interaction coefficient larger than 0.62. The triplet transition dipole moment was calculated using the quadratic response function.^{87,92} Figure 5.3b shows the x, y, z directions of the dipole moment for the transition from three sublevels of the triplet state. The angles between the C_2 axis and the direction of the total triplet transition dipole moments of the HICs were found to be nearly right angles, with values of 89.02° for Ir(mphq)₂acac, 85.19° for Ir(MDQ)₂acac and

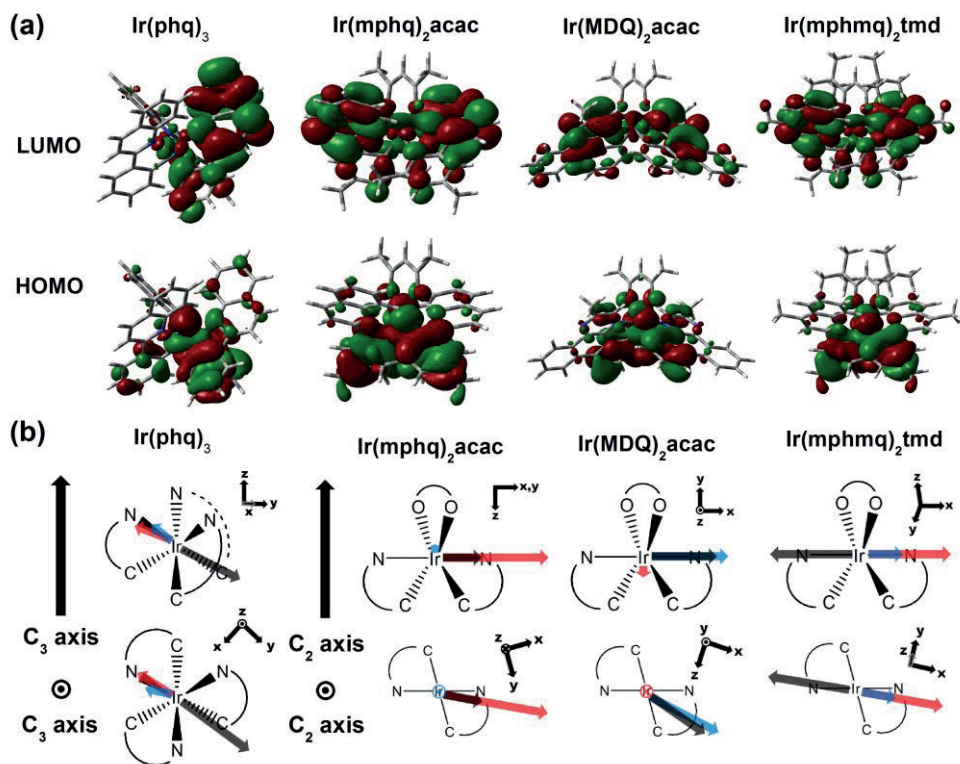


Figure 5.3 Quantum chemical calculations of the red dyes based on DFT. (a) Frontier molecular orbitals contributing to the lowest triplet transitions of Ir(phq)₃, Ir(mphq)₂acac, Ir(MDQ)₂acac and Ir(mphmq)₂tmd. (b) The triplet transition dipole moments of Ir(phq)₃, Ir(mphq)₂acac, Ir(MDQ)₂acac and Ir(mphmq)₂tmd from three spin sublevels are shown as arrows. The transition dipole moments of the T_x, T_y and T_z sublevels correspond to the black, red and blue arrows respectively.

90.45° for Ir(mphmq)₂tmd. In sharp contrast, the directions of the triplet transition dipole moments of fac-Ir(phq)₃ adopted a slant angle of 67.6° with respect to the C₃ axis. Therefore, the axial components (\perp) of the transition dipole moments along the C₃ axis were approximately half of the equatorial components (\parallel) in the molecule ($\perp : \parallel = 2.4:1$). The full calculation results, including the individual values of the transition dipole moments, are summarized in Table 5.1.

The molecular arrangements and orientations of the red emitters with respect to the underlying substrate in the EML also influenced the orientation of the transition dipole moments. The optical anisotropy with different ordinary and extraordinary refractive indices was measured by VASE, and the data indicated that the molecular long axes of the host molecules were parallel to the substrate (Figure 5.4).⁹³ Because the EML contains a small amount of red dyes (~0.035 mol fraction), the molecular orientations of the red dyes and their resultant electro-optic performance rely on the binding geometries of the red dyes with the host molecules. To computationally investigate the intermolecular interactions between the constituent molecules in the EML, geometry optimizations were performed on the NPB/B3PYMPM/red dye ternary systems using DFT with the Perdew–Burke–Ernzerhof functional⁸⁹ with a double numerical basis set and the polarization basis set under an effective core potential. Figure 5.5a-d shows the optimized geometries of the red dye/cohost molecular clusters (or supramolecules), revealing that the C₂ axis of the HICs (Ir(mphq)₂acac, Ir(MDQ)₂acac and Ir(mphmq)₂tmd), as well as the C₃ axis of fac-Ir(phq)₃ were almost perpendicular to the molecular long axes of the

Table 5.1 Dipole moment ($M_\alpha(T^k)$) of the S_0 - T_1 transition for the T_1 geometry. A represents the direction of the transition dipole moment and k represents the Cartesian component of the ZFS triplet state spin sublevel. All values of the dipole moments are in a.u.

Transition moment (sublevel)	Ir(phq) ₃	Ir(mphq) ₂ acac	Ir(MDQ) ₂ acac	Ir(mphmq) ₂ tmd
$M_x(T^x)$	-1.12×10^{-4}	7.95×10^{-4}	1.31×10^{-3}	-1.62×10^{-3}
$M_y(T^x)$	1.13×10^{-3}	3.18×10^{-4}	0	4.00×10^{-5}
$M_z(T^x)$	-7.86×10^{-4}	0	1.14×10^{-4}	1.10×10^{-5}
$M_x(T^y)$	4.9×10^{-5}	2.00×10^{-3}	0	1.63×10^{-3}
$M_y(T^y)$	-6.42×10^{-4}	7.19×10^{-4}	-2.38×10^{-4}	-9.00×10^{-6}
$M_z(T^y)$	2.09×10^{-4}	0	0	-2.00×10^{-6}
$M_x(T^z)$	1.83×10^{-4}	0	1.51×10^{-3}	6.82×10^{-4}
$M_y(T^z)$	-3.93×10^{-4}	0	0	-1.40×10^{-5}
$M_z(T^z)$	2.64×10^{-4}	-5.10×10^{-5}	-1.29×10^{-4}	1.80×10^{-5}

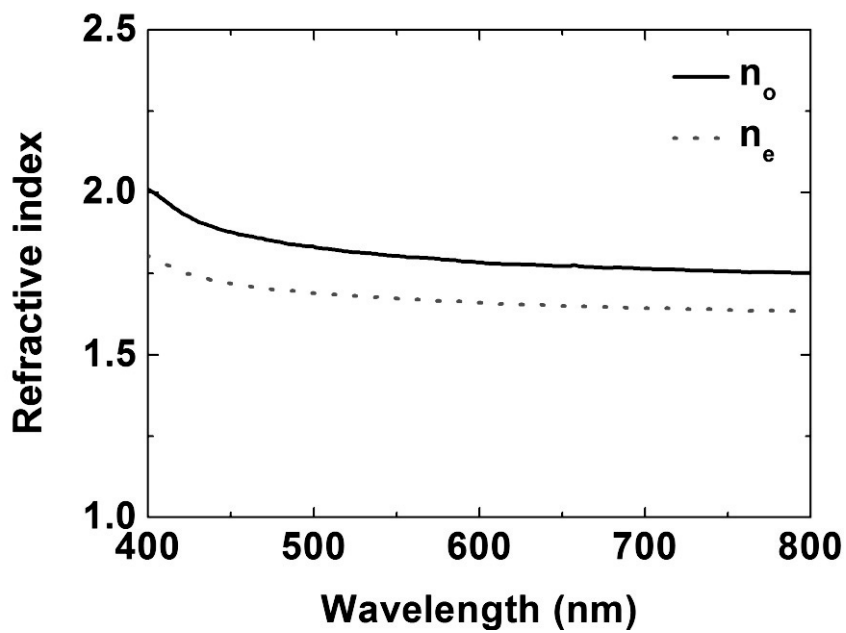


Figure 5.4 Refractive index of the undoped co-host layer (NPB:B3PYMPM, 1:1 molar ratio) film (50 nm thick) as measured by VASE.

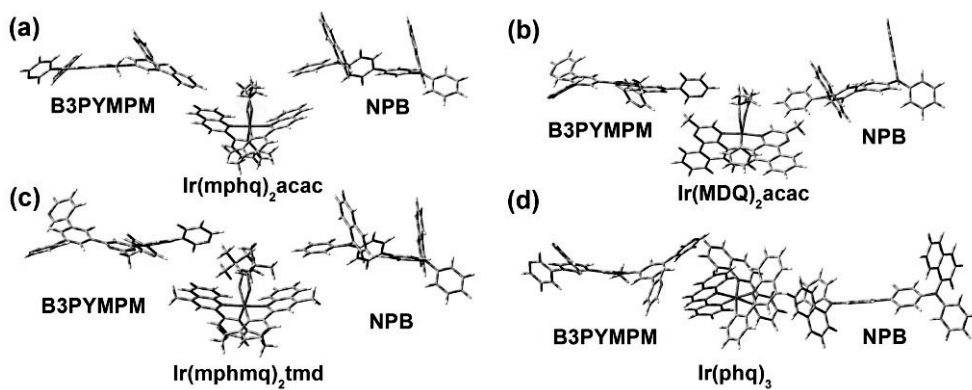


Figure 5.5 Optimized binding geometries of the red dye co-host supramolecules. (a) B3PYMPM-Ir(mphq)₂acac-NPB, (b) B3PYMPM-Ir(MDQ)₂acac-NPB, (c) B3PYMPM-Ir(mphmq)₂tmd-NPB and (d) B3PYMPM-Ir(phq)₃-NPB.

NPB and B3PYMPM molecules. The binding energies of the four red dye/co-host systems (that is, NPB-dye-B3PYMPM) were almost identical at ~ 70 kcal/mol. The pairwise binding energies of the NPB/B3PYMPM/dye systems are given in Table 5.2. Notably, the binding energies between the HICs and the host molecules (NPB or B3PYMPM) were $\sim 10 - 20$ times stronger than the binding energies between the other binding pairs (2 - 3 kcal/mol). The strong binding energies of the HICs with the host molecules can be attributed mainly to the electron-deficient nature of the *N*-heterocycles that interact strongly with the electron-rich region of the aromatic rings in the tail of the host molecules. Isosurfaces of the molecular ESP for the HICs and the host molecules are shown in Figure 5.6a-f. The isosurfaces suggest that the highly electropositive spots ($+ 0.1$ J/C) at the methyl groups (Ir(mphmq)₂tmd and Ir(MDQ)₂acac) or hydrogens (Ir(mphq)₂acac) belonging to the *N*-heterocycles of the HICs are responsible for the strong Coulomb interactions with the electronegative aromatic planes of the host molecules. From the optimized binding geometries in Figure 5.5a-c, the host molecules are docked in the space between these two spots (*N*-heterocycles and β -diketonate ancillary ligands), and these are almost perpendicular to the C₂ axes of the HICs. The spaces between the highly electropositive spots can thus be regarded as binding sites for the HIC molecules that lead to supramolecular assembly between the HICs and the host molecules. Because the NPB and B3PYMPM molecules are horizontally oriented in the co-host films, the C₂ axes of the HIC molecules tend to be more or less perpendicular to the film surface. Therefore, it is inferred from these calculations that the preferred orientation of the transition dipole moments of the HICs in the EMLs is along the horizontal

Table 5.2 Pairwise binding energies of the hosts (NPB, B3PYMPM) and the red dyes (Ir(phq)₃, Ir(mphq)₂acac, Ir(MDQ)₂acac, Ir(mphmq)₂tmd). All binding energies are in kcal/mol).

	NPB	B3PYMPM	Ir(phq) ₃	Ir(mphq) ₂ acac	Ir(MDQ) ₂ acac	Ir(mphmq) ₂ tmd
NPB	-3.5	-4.1	-37.2	-37.8	-37.1	-38.2
B3PYMPM		-3.3	-31.4	-30.9	-32.2	-30.8
Ir(phq) ₃			-1.6			
Ir(mphq) ₂ acac				-1.6		
Ir(MDQ) ₂ acac					-3.4	
Ir(mphmq) ₂ tmd						-2.1

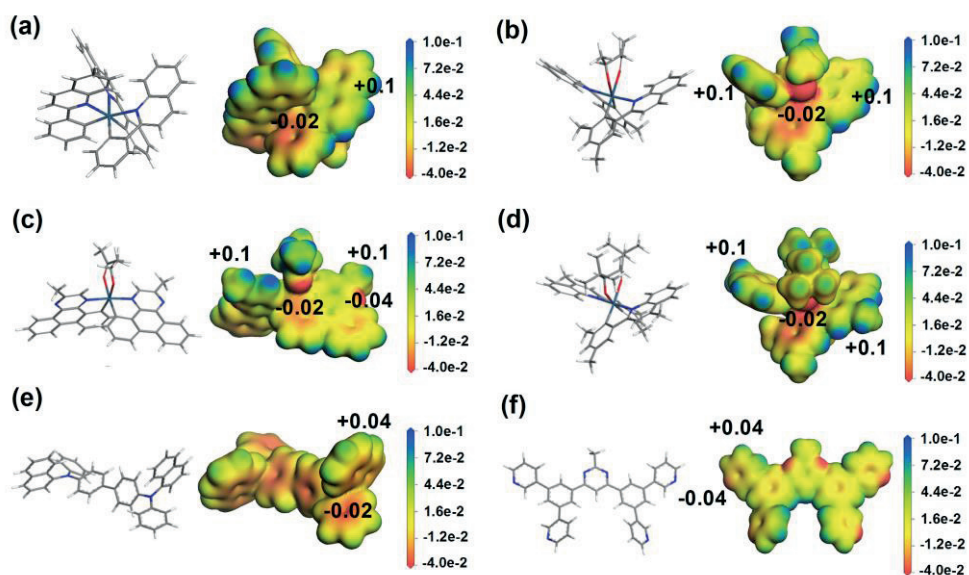


Figure 5.6 Isosurfaces of the molecular ESP. (a) Ir(phq)₃, (b) Ir(mphq)₂acac, (c) Ir(MDQ)₂acac, (d) Ir(mphmq)₂tmd, (e) NPB and (f) B3PYMPM. The numerals on the isosurfaces are in J/C. The electron-deficient nature of the *N*-heterocycles and the β -diketonate ancillary ligand interact strongly with the electron-rich region of the aromatic rings in the tail of the host molecules.

direction because of the almost perpendicular direction of the transition dipole moments to the C_2 axis in the HICs. However, a smaller horizontal transition dipole moment is predicted for fac-Ir(phq)₃ because the molecule has a horizontal-to-vertical transition dipole moment ratio of $\sim 0.705:0.295$ from the $\perp:\parallel = 2.4:1$ because the C_3 axis is perpendicular to the substrate. The ratio is very close to the experimentally obtained $\Theta = 0.70$. Notably, the rotation of the homoleptic molecule does not significantly change the orientational factor Θ because of the molecular symmetry.

It is worth commenting that our simulations of the binding geometries were based only on the optimization of three molecules, consisting of one emitter molecule and two host molecules. Nonetheless, because the content of emitters in this amorphous mixture is quite small, and because the emitters investigated in this study have only two binding sites with extremely high binding energies to the host molecules (10-20 times those of the emitter–emitter and host–host interactions), we presume that the host–emitter–host supramolecule is a unit pseudo-molecule comprising the emission layer with excessive host molecules and that its internal geometry is little affected by neighboring pseudo-molecular units or host molecules.

5.3.3 Fabrication and performance of the OLEDs

Having verified the preferred horizontal orientation of the HIC transition dipoles, we fabricated OLEDs to examine the influence of the anisotropic dipole alignment. Figure 5.7a schematically shows the configuration of the device and the energy levels of the layers that were incorporated into the devices. The multilayer OLEDs were prepared with the following layers: ITO (100 nm)/ TAPC (75 nm)/NPB (10 nm)/NPB:B3PYMPM: 3.5 mol% red dyes (30 nm)/B3PYMPM (10 nm)/B3PYMPM: 2 wt% Rb₂CO₃ (45 nm)/Al (100 nm). The NPB and B3PYMPM were used as the hole transport material and the electron transport material, respectively. The hole transport material and electron transport material were also used as co-hosts of the EML at a molar ratio of 1:1. This co-host system facilitates efficient charge injection from the electrodes to the EML because it removes the injection barrier for electrons (or holes) from the electron transport layer (ETL or hole transport layer) to the EML.

The current density–voltage–luminance (J - V - L) characteristics of the OLEDs containing fac-Ir(phq)₃, Ir(mphq)₂acac, Ir(MDQ)₂acac or Ir(mphmq)₂tmd are shown in Figure 5.7b. The devices showed identical J - V characteristics but different L - V characteristics because of the differences in their emission spectra and EQEs. The EL spectra (Figure 5.7c) of the OLEDs matched the PL spectra of the dyes doped in the co-host film well. The EQEs and power efficiencies of the devices calibrated using the profiles of the angle-dependent number of emitted photons (inset of Figure 5.7b) are shown in Figure 5.7d. The EQE of the Ir(mphmq)₂tmd device was higher than that of the devices containing Ir(MDQ)₂acac, Ir(mphq)₂acac or fac-Ir(phq)₃.

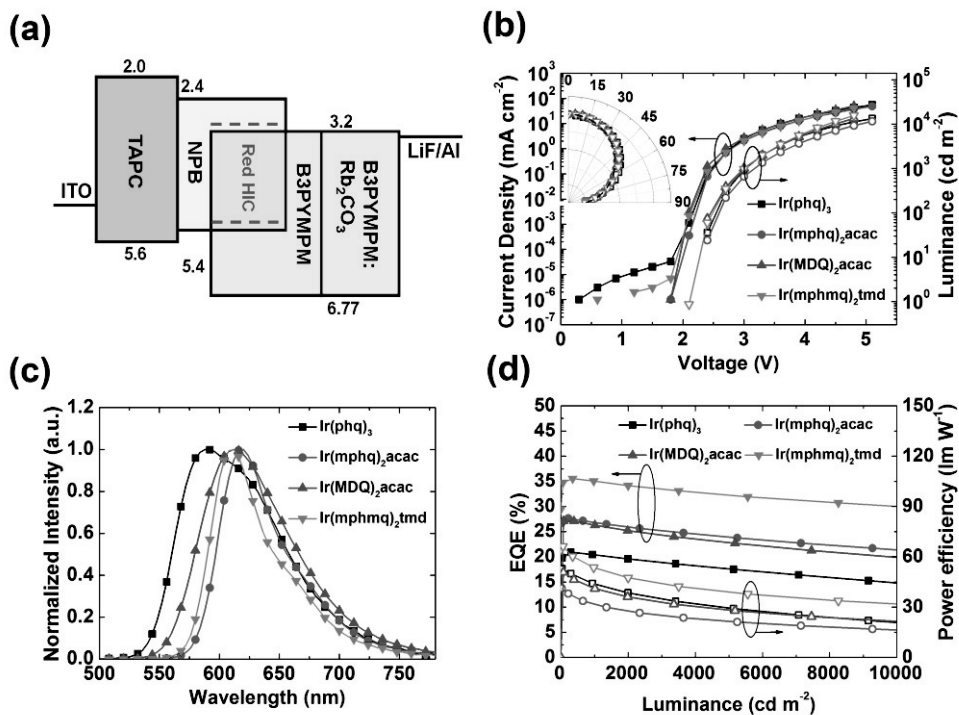


Figure 5.7 Device structure and OLED performance for red dyes. (a) Schematic diagram of the device structure and the energy levels of the device. (b) $J-V-L$ curves. Inset: the angular distribution of the EL intensity of the OLEDs. The dashed line in the inset shows the Lambertian distribution. (c) EL spectrum of the OLEDs. (d) EQEs and power efficiency as a function of the luminance.

Specifically, the Ir(mphmq)₂tmd device showed a very high EQE of 35.6% at a luminance of 350 cd/m², which is 1.5 times higher than the highest efficiency reported to date for red OLEDs and even higher than that of green OLEDs.^{30,75,76,79,94,95} The efficiency roll-off was also very small, as the EQE was 35.1% at 1,000 cd/m² and 30.0% at 10,000 cd/m². If one considers the sensitivity of human eyes, red emission with a luminance of 10,000 cd/m² corresponds to a radiative intensity 2 - 3 times higher than that of green emission at the same luminance. The high EQE combined with a low turn-on voltage (2.1 V) and a low driving voltage resulted in a high power efficiency with a maximum value of 66.2 lm/W (53.6 lm/W at 1,000 cd/m²) in the optimized device.

5.3.4 Optical simulation of the EQE of devices

To explain the high EQE, the maximum EQE for the Ir(mphmq)₂tmd device was simulated as a function of the total thickness of the ETL (t_{ETL}) using $q_{\text{PL}} = 0.96$ and $\Theta = 0.82$.²⁴ As shown in Figure 5.8a, the calculated profiles exhibit a sinusoidal variation in the EQE with increasing t_{ETL} and match the experimental data very well over a wide t_{ETL} range. The J - V - L data, angle-dependent emission patterns, emission spectrum, quantum efficiency and power efficiency data for the devices in Figure 5.8a are shown in Figure 5.9-12. We repeated the calculation of the maximum EQEs of the optimized devices with red dyes using (q_{PL} , Θ) values of (0.71, 0.70) for fac-Ir(phq)₃, (0.83, 0.77) for Ir(mphq)₂acac, (0.82, 0.80) for Ir(MDQ)₂acac and (0.96, 0.82) for Ir(mphmq)₂tmd. We assumed a perfect electron-hole balance in these devices. The predicted maximum EQE values for the devices based on fac-Ir(phq)₃, Ir(mphq)₂acac, Ir(MDQ)₂acac and Ir(mphmq)₂tmd were 22.2%, 29.1%, 29.6% and 34.9%, respectively. These values are in excellent agreement with the measured maximum EQEs of the fac-Ir(phq)₃ (20.9%), Ir(mphq)₂acac (27.6%), Ir(MDQ)₂acac (27.1%) and Ir(mphmq)₂tmd (35.6%) containing devices. The unprecedented value of EQE 35.6% is originated from high Θ combined with high q_{PL} of Ir(mphmq)₂tmd.

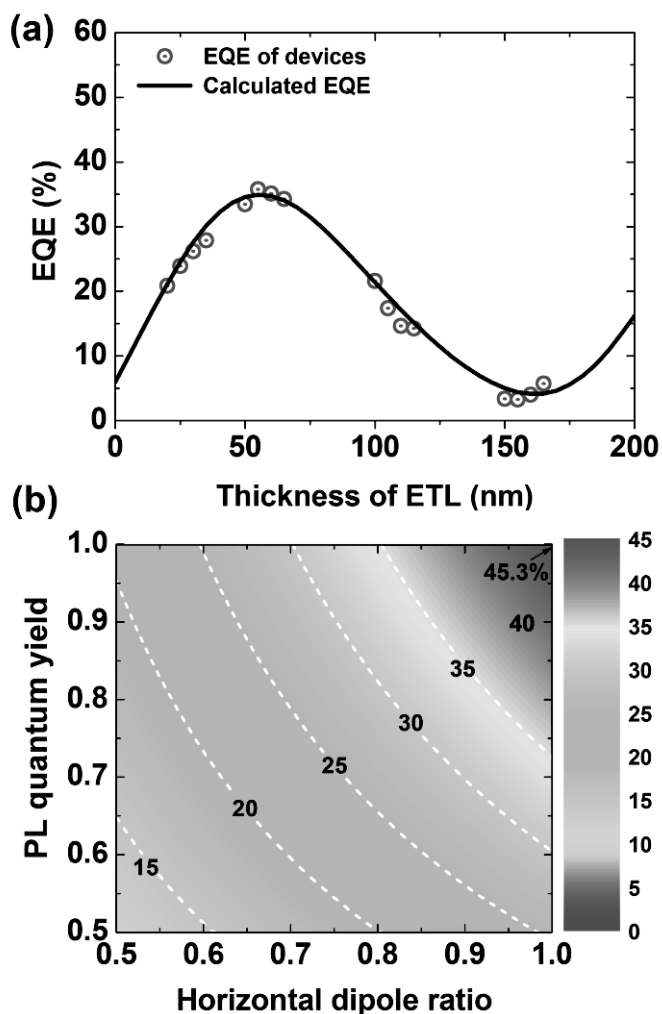


Figure 5.8 Optical simulation of the EQE of devices. (a) EQEs of the Ir(mphmq)₂tmd-based OLEDs with varying ETL thickness (circles with dots). The J - V - L , angle-dependent emission patterns, emission spectra, quantum efficiencies and power efficiency data for these devices are shown in Figure 5.9-12. (b) Contour plot of the maximum EQEs achievable with Ir(mphmq)₂tmd possessing a certain PL quantum yield (q_{PL}) and ratio of the horizontal dipole (Θ).

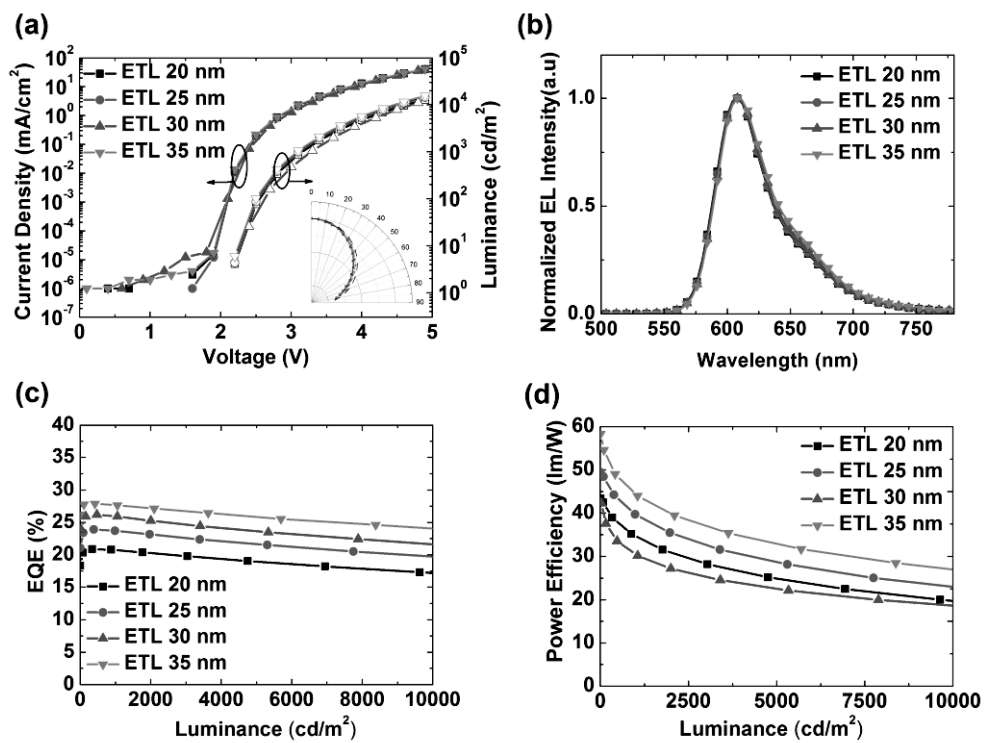


Figure 5.9 Performance of OLEDs with different thicknesses of ETL (20, 25, 30, and 35 nm). (a) Current density–voltage–luminance curves. Inset: Angular distribution of the EL intensity of the OLEDs. The dashed line shows the Lambertian distribution. (b) EL spectra. (c) external quantum efficiencies and (d) power efficiencies versus luminance of the OLEDs.

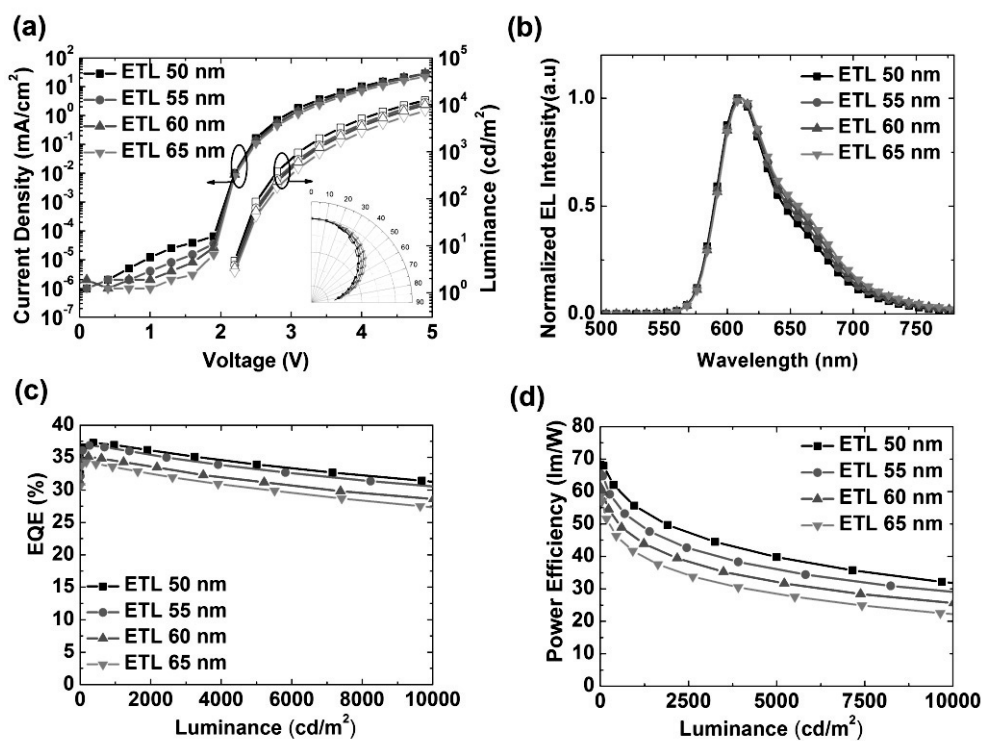


Figure 5.10 Performance of OLEDs with different thicknesses of ETL (50, 55, 60, and 65 nm). (a) Current density–voltage–luminance curves. Inset: Angular distribution of the EL intensity of the OLEDs. The dashed line shows the Lambertian distribution. (b) EL spectra. (c) external quantum efficiencies and (d) power efficiencies versus luminance of the OLEDs.

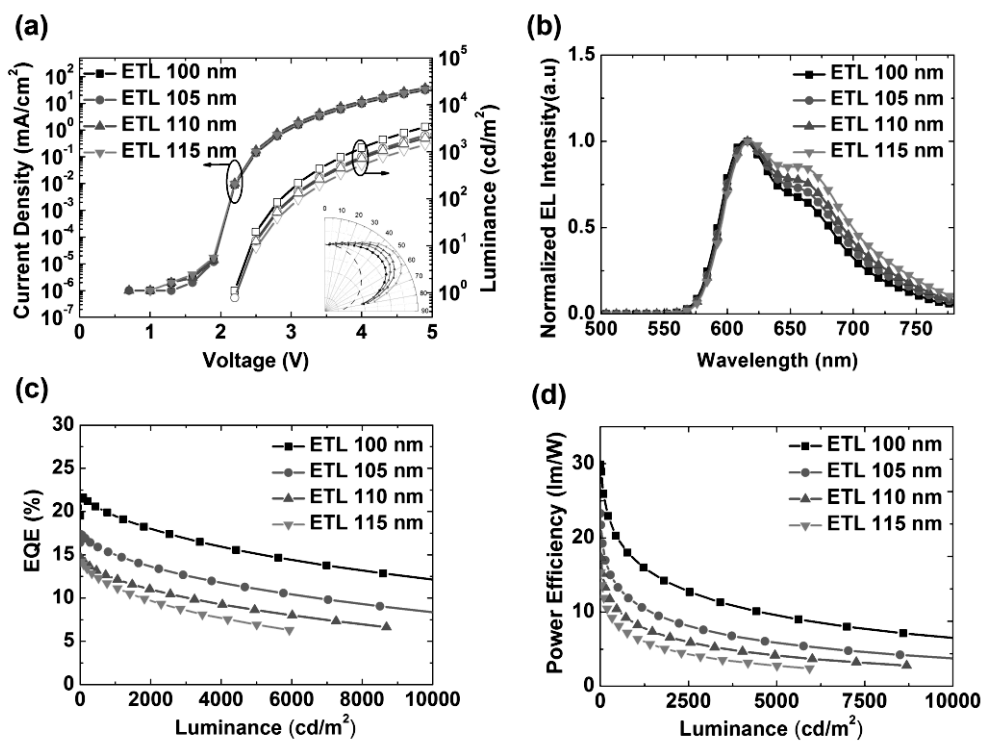


Figure 5.11 Performance of OLEDs with different thicknesses of ETL (100, 105, 110, and 115 nm). (a) Current density–voltage–luminance curves. Inset: Angular distribution of the EL intensity of the OLEDs. The dashed line shows the Lambertian distribution. (b) EL spectra. (c) external quantum efficiencies and (d) power efficiencies versus luminance of the OLEDs.

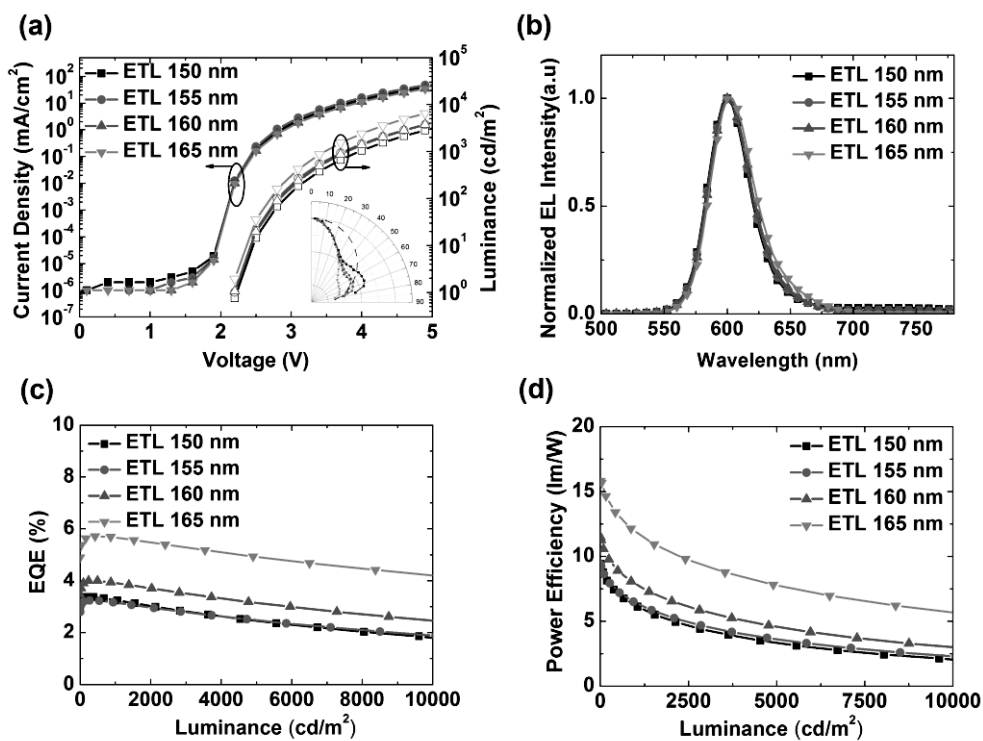


Figure 5.12 Performance of OLEDs with different thicknesses of ETL (150, 155, 160, and 165 nm). (a) Current density–voltage–luminance curves. Inset: Angular distribution of the EL intensity of the OLEDs. The dashed line shows the Lambertian distribution. (b) EL spectra. (c) external quantum efficiencies and (d) power efficiencies versus luminance of the OLEDs.

5.4 Conclusion

Using quantum chemical calculations, we demonstrated that the preferred orientation of HICs in OLEDs originates from the preferred direction of the HIC triplet transition dipole moments and the strong supramolecular arrangement within the co-host environment. The elongated supramolecules themselves or the preferred horizontal orientation of the host molecules resulted in the preferred horizontal triplet transition dipole moments of the HICs in the EML. Understanding the origin of the preferred orientation of HICs will enable us to design dyes with highly oriented transition dipole moments. As a result, it will be possible to achieve EQEs much higher than the conventional limit of 30%. To verify the effect of the orientation of the transition dipole moments on EQE, the simulation was extended to calculate the maximum achievable EQEs for red OLEDs using the emission spectrum of Ir(mphmq)₂tmd with arbitrary values of q_{PL} and Θ . Figure 5.8b shows a contour plot of the maximum EQEs for the red OLEDs as a function of q_{PL} and Θ assuming a perfect electron-hole balance without any electrical loss. The figure clearly shows that an EQE of over 45% is achievable if the emitter has a q_{PL} of 1 and horizontally oriented transition dipole moments. Practically, an EQE of 40% is possible with $q_{\text{PL}} = 0.95$ and $\Theta = 0.95$. The value is significantly higher than that achievable with randomly oriented emitting dipoles.

Chapter 6. Controlling emitting dipole orientation with methyl substituents on main ligand of iridium complexes for highly efficient phosphorescent organic light-emitting diodes

6.1 Introduction

Phosphorescent iridium complexes have long been thought to have random orientation when doped in an emitting layer (EML) due to their octahedron structures. External quantum efficiency (EQE) of organic light-emitting diodes (OLEDs) without any out-coupling structures is theoretically limited to 25%–30% if the orientation of emitting dipoles is randomly oriented.¹¹ Some platinum complexes and homoleptic iridium complexes indeed exhibited nearly isotropic orientation with the horizontal dipole ratio (Θ) of 67%–70%^{32,33,96,97}, where Θ is defined as the ratio of the horizontal transition dipole moments (TDMs) to total TDMs in an EML. Recently, however, some heteroleptic iridium complexes that have the ancillary ligands of β -diketonate or picolinate have been reported to have preferred orientation of emission dipoles along the horizontal direction (parallel to substrates) with Θ of 76%–82%.^{7,8-20,32-34} The outcoupling efficiency of the emitted light from the horizontally oriented emitting dipoles in an OLED can reach 45% that is much higher than isotropically oriented transition dipoles.^{7,18,20,33}

However, the origin of the preferred emitting dipole orientation (EDO) and the factors influencing the orientation have not been studied much. There are two

requirements for a phosphorescent dye to have preferred EDO in a film: (1) the phosphorescent dye should have triplet TDMs preferentially oriented along a specific direction and not have a combination of transition dipole moments with various orientations, and (2) the phosphorescent molecules themselves should align in the film with a preferred orientation with respect to the substrate.³³ It was proposed based on quantum chemical calculation that the heteroleptic molecular structure of the Ir (III) complexes and strong Coulombic interaction between the dopant and host molecules are the driving forces of the preferred EDO.^{32,33} In this regard, the structure of the emitting molecules, as well as the organic host molecules, must influence the EDO. The effect of the ancillary ligands in the heteroleptic Ir complexes (HICs) on the EDO and the photoluminescence quantum yields (PLQY) in doped films were reported recently, exhibiting that bis(2-phenylpyridine)Ir(III)(2,2,6,6-tetramethylheptane-3,5-diketonate) (Ir(ppy)₂tmd) results in higher PLQY and Θ values than bis(2-phenylpyridine)Ir(III)acetylacetonate (Ir(ppy)₂acac), which in turn has higher values than tris(2-phenylpyridine)Ir(III) (Ir(ppy)₃). Unfortunately, the reason why different ancillary ligands resulted in different EDOs has not been reported yet and their discussion was limited to rather qualitative description and there are few reports on the quantitative and systematic investigation of the effect of the structure of the emitting molecules on the EDO in films. Furthermore, the effect of the main ligands in HICs has not been investigated up to now to our best knowledge. The understanding of the structure–property relationship will eventually lead us to identify phosphorescent dyes with high Θ in films to fabricate OLEDs with high

EQE.

In this study, we investigated the effect of main ligands of HICs on the EDO in doped films and related the EDO to the angle between the TDM of emission dipoles and the C_2 axis of the molecules. For this purpose, we designed and synthesized four iridium complexes where the hydrogen atom(s) at different positions of the cyclometalated ligands of $\text{Ir}(\text{ppy})_2\text{tmd}$ were systematically replaced by methyl group(s) keeping the ancillary ligand the same as tmd. We used the same host for the dopants to minimize the host effect, i.e., to minimize the variation of the intermolecular interaction between the dopants and the host. We found that the methyl substitution resulted in different directions of the TDM in the iridium complexes. Moreover, the molecules with higher angle between the C_2 axis and the TDM in the molecules resulted in a higher horizontal portion of the emitting dipole orientation in the emitting layer. Based on the observation, we were able to develop a new green emitter having high Θ of 80% and PLQY of 97% and resultantly demonstrate a green OLED exhibiting an unprecedented high EQE of 34.1%, power efficiency (PE) of 157.6 lm/W, and current efficiency (CE) of 120.5 cd/A using the new emitter.

6.2 Experimental

Materials synthesis. New Ir complexes were designed by K.-H. Kim and J.-J. Kim at Seoul National University and synthesized by Y.-H. Kim and co-workers at Gyeongsang National University.

Calculation of triplet transition dipole moments of molecules. Triplet geometries of molecules were calculated using Gaussian09 program⁶⁴. The optimization of triplet state geometry were performed using B3LYP, LANL2DZ basis set for Ir, and the 6-311+G(d,p) for all other atoms. To calculate triplet transition properties of molecules, time-dependent density functional theory (TD-DFT) were carried out with optimized geometries using Dalton2013 program^{98,99}. The transition dipole moments of triplet states were calculated with a quadratic response function and LANL2DZ basis set for Ir, and 6-31G(d) for all other atoms.

Measurement of orientation of transition dipoles. Orientation of transition dipole moments was measured using a continuous wave laser (325 nm, Melles Griot). The incident angle of the excitation source was fixed at 45°. The angle dependent PL spectra of p-polarized light was detected using charge-coupled device (MAYA 2000, Ocean optics).

Device fabrication and characterization. The OLEDs were fabricated on clean glass substrates that were pre-patterned with 70-nm thick ITO under a pressure of 5×10^{-7} Torr by thermal evaporation without breaking the vacuum. Current density, luminance, and electroluminescence spectra were measured using a programmable source meter (Keithley 2400) and a spectrophotometer (Spectrascan PR650, Photo

Research). The angular distribution of the EL was measured with a programmable source meter (Keithley 2400), a goniometer, and a fiber optic spectrometer (Ocean Optics S2000).

6.3 Result and discussion

Chemical structures of the green-emitting phosphorescent dyes investigated in this study are shown in Figure 6.1a. All the structures are based on Ir(ppy)₂tmd having high Φ and high PLQY.^{32,73} Bis(2-phenyl-3-methylpyridine)Ir(III)(2,2,6,6-tetramethylheptane-3,5-diketonate) (Ir(3-mppy)₂tmd), bis(2-phenyl-4-methylpyridine)Ir(III)(2,2,6,6-tetramethylheptane-3,5-diketonate) (Ir(4-mppy)₂tmd), and bis(2-phenyl-5-methylpyridine)Ir(III)(2,2,6,6-tetramethylheptane-3,5-diketonate) (Ir(5-mppy)₂tmd) have a methyl substituent on different sites of the pyridine ring, whereas bis(2-(3,5-dimethylphenyl)-4-methylpyridine)Ir(III)(2,2,6,6-tetramethylheptane-3,5-diketonate) (Ir(3',5',4-mppy)₂tmd) has three methyl substituents on both pyridine and phenyl rings of Ir(ppy)₂tmd. We designed the molecules under the expectation that the methyl substitution of the hydrogen atom(s) in the cyclometalated ligands of the Ir complexes will modify the electron density and its distribution in the lowest unoccupied molecular orbital (LUMO) and the highest occupied molecular orbital (HOMO) of the molecules, resulting in the change of the direction of the TDMs in the molecules.

The absorption and emission spectra of the compounds are shown in Figure 6.1b. The absorption at 340–370 nm can be assigned to a spin allowed singlet metal-to-ligand charge transfer (¹MLCT) transition and weak long absorption at 450–470 nm can be assigned to the spin-forbidden triplet ligand centered (³LC) and/or triplet MLCT (³MLCT) transitions. The peak wavelengths of the PL spectra were 529 nm for Ir(3-mppy)₂tmd, 520 nm for Ir(4-mppy)₂tmd, 522 nm for Ir(5-mppy)₂tmd, and

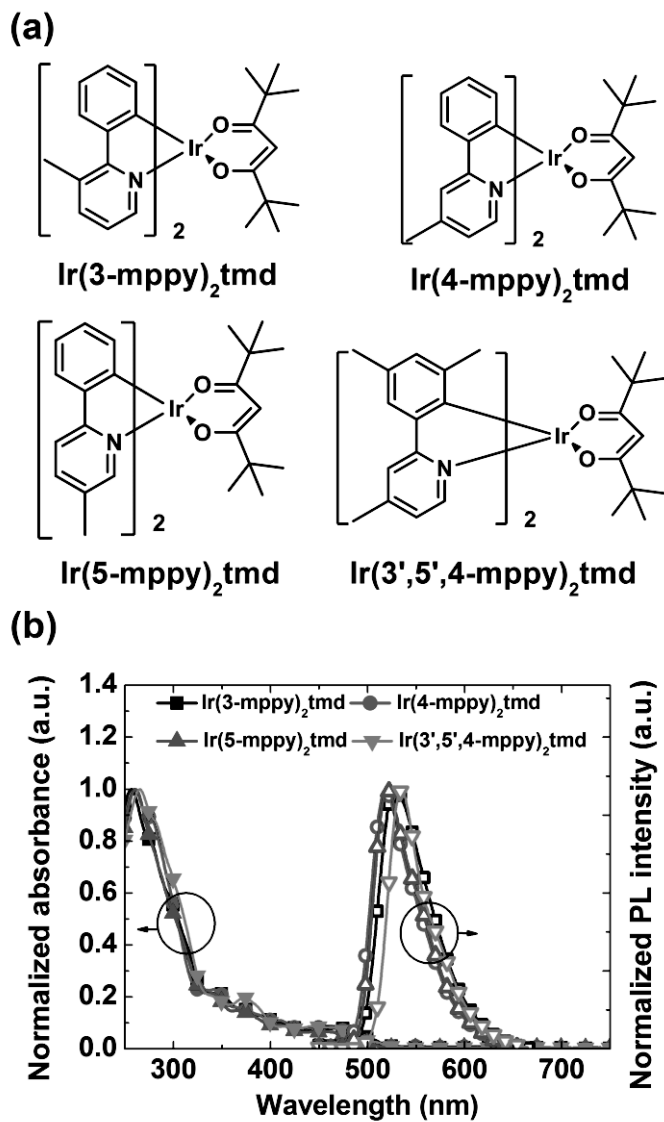


Figure 6.1 (a) Molecular structures and (b) absorption and PL spectra of Ir(3-mppy)₂tmd, Ir(4-mppy)₂tmd, Ir(5-mppy)₂tmd, and Ir(3',5',4-mppy)₂tmd in chloroform.

531 nm for Ir(3',5',4-mppy)₂tmd, respectively. The HOMO levels of the compounds were measured by using cyclic voltammetry, and the LUMO levels were calculated from the HOMO levels and the optical bandgaps. The HOMO levels of Ir(3-mppy)₂tmd, Ir(4-mppy)₂tmd, and Ir(5-mppy)₂tmd are similar because of the same substituents of phenyl rings, whereas Ir(3',5',4-mppy)₂tmd that has two methyl substituents on the phenyl ring showed a higher HOMO level than the other Ir-complexes (Table 6.1). The PLQYs of the Ir complexes were measured by using 50 nm thick films on quartz substrates in an integrating sphere. The PLQYs of Ir(3-mppy)₂tmd, Ir(4-mppy)₂tmd, Ir(5-mppy)₂tmd, and Ir(3',5',4-mppy)₂tmd doped (8 wt%) in 4,4',4''-tris(*N*-carbazolyl)-triphenylamine (TCTA): bis-4,6-(3,5-di-3-pyridylphenyl)-2-methylpyrimidine (B3PYMPM) co-hosts were 92%, 93%, 93%, and 97%, respectively. The photophysical and electronic properties of the compounds are summarized in Table 6.1.

The triplet transition properties of the Ir complexes were studied using the time-dependent density functional theory (DFT) with B3LYP level, the LANL2DZ basis set for the Ir atom, and the 6-31g(d) basis set for all other atoms. Details of the calculation scheme were reported previously.³³ The triplet transition energies were found to be 2.09 eV for Ir(3-mppy)₂tmd, 2.16 eV for Ir(4-mppy)₂tmd, 2.13 eV for Ir(5-mppy)₂tmd, and 1.99 eV for Ir(3',5',4-mppy)₂tmd. The total TDMs of the molecules are shown in Figure 6.2. The TDMs of the three sublevels of the T₁ state for each molecule are shown in Figure 6.3. The Ir complexes have different directions of the triplet TDMs that are significantly affected by the methyl

Table 6.1 Photophysical and electronic properties of the iridium complexes

Ir complex	Absorption peaks ^{a)} [nm]	PL peaks ^{a)} [nm]	FWHM [nm]	T ₁ [eV]	HOMO [eV]	LUMO [eV]	Film PL quantum yield (%)
Ir(3-mpyy) ₂ tmd	256, 349, 470	529	58	2.29	5.18	2.82	92
Ir(4-mpyy) ₂ tmd	259, 346, 463	519	53	2.39	5.16	2.76	93
Ir(5-mpyy) ₂ tmd	259, 342, 458	520	55	2.38	5.16	2.78	93
Ir(3',5',4-mpyy) ₂ tmd	265, 374, 455	530	46	2.34	5.06	2.72	97

^{a)} Measured in a CHCl₃ solution at room temperature

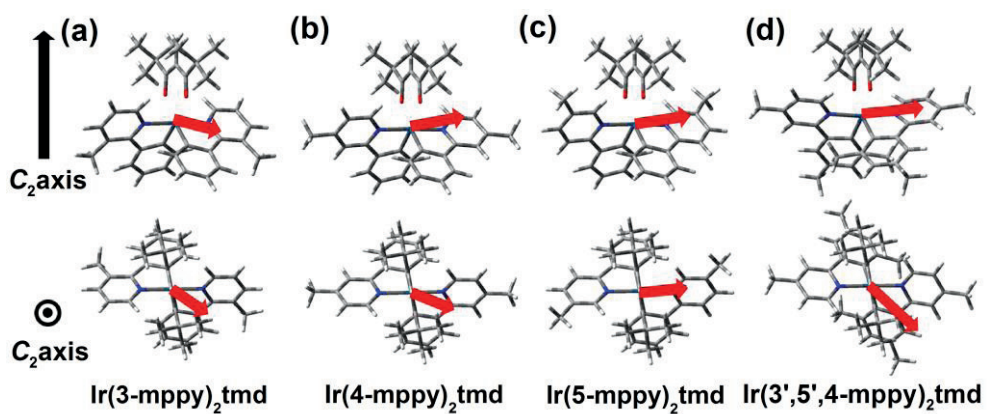


Figure 6.2 The triplet transition dipole moments of (a) Ir(3-mppy)₂tmd, (b) Ir(4-mppy)₂tmd, (c) Ir(5-mppy)₂tmd, and (d) Ir(3',5',4-mppy)₂tmd from the DFT calculations. Arrows represent the directions and relative magnitudes of the triplet transition dipole moments.

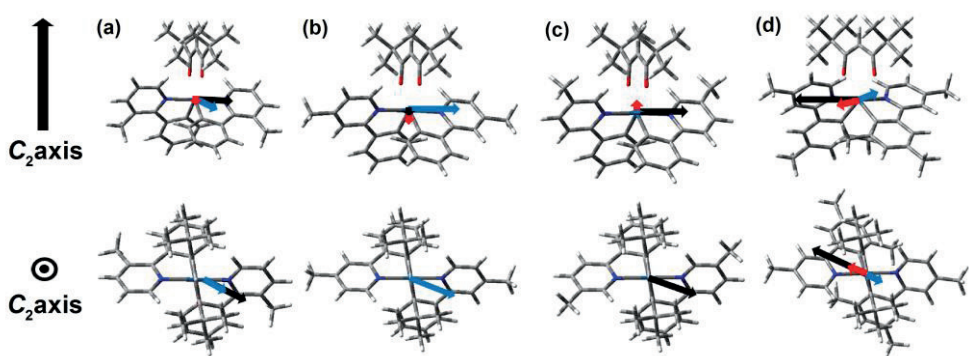


Figure 6.3 The triplet transition dipole moments of Ir(3-mppy)₂tmd, Ir(4-mppy)₂tmd, Ir(5-mppy)₂tmd, and Ir(3',4',5-mppy)₂tmd from three spin sublevels are shown as arrows. The transition dipole moments of the T_x, T_y and T_z sublevels correspond to the black, blue, red arrows respectively.

substituents of the cyclometalated ligand, as expected. The TDMs of Ir(3-mppy)₂tmd, Ir(4-mppy)₂tmd, and Ir(5-mppy)₂tmd are directed from the iridium metal to the methyl substituent in the main ligands. That is because the carbon adjacent to the methyl substituent has higher electron density than other carbon atoms in the *N*-heterocycle. The high electron density results from inductive effect of methyl substituents, which generates large transition from the carbon atoms adjacent to the methyl substituent when MLCT and LC charge transfer take place. The angles (Φ_s) between the C₂ axis and the direction of transition dipole moments were found to be 78.0° for Ir(3-mppy)₂tmd, 79.7° for Ir(4-mppy)₂tmd, 82.4° for Ir(5-mppy)₂tmd, and 85.5° for Ir(3',5',4-mppy)₂tmd, respectively. Oscillator strengths of the Ir complexes were calculated to be 4.89×10^{-4} a.u. for Ir(3-mppy)₂tmd, 5.65×10^{-4} a.u. for Ir(4-mppy)₂tmd, 5.69×10^{-4} a.u. for Ir(5-mppy)₂tmd, and 1.01×10^{-3} a.u. for Ir(3',5',4-mppy)₂tmd, respectively. The values of oscillator strengths are well consistent with the PLQYs of the dyes, as expected.

The emitting dipole orientation of the dyes in the emitting layer composed of TCTA:B3PYMPM:8 wt% dyes was determined from the analysis of the angle-dependent PL spectra obtained from the 32 nm thick films on fused silica substrates (Figure 6.4a–d). The angle-dependent PL spectra were analyzed using the classical dipole model considering the birefringence effect of the film.^{7,17,24,59,100} The experimental data were well fitted by the Θ values of 0.74 for Ir(3-mppy)₂tmd, 0.75 for Ir(4-mppy)₂tmd, 0.77 for Ir(5-mppy)₂tmd, and 0.80 for Ir(3',5',4-mppy)₂tmd. The Θ value of Ir(3-mppy)₂tmd is the same as the Θ value of Ir(pppy)₂tmd that has no substituents on the main ligands,¹⁰⁰ whereas Θ s of the other dyes are larger than that

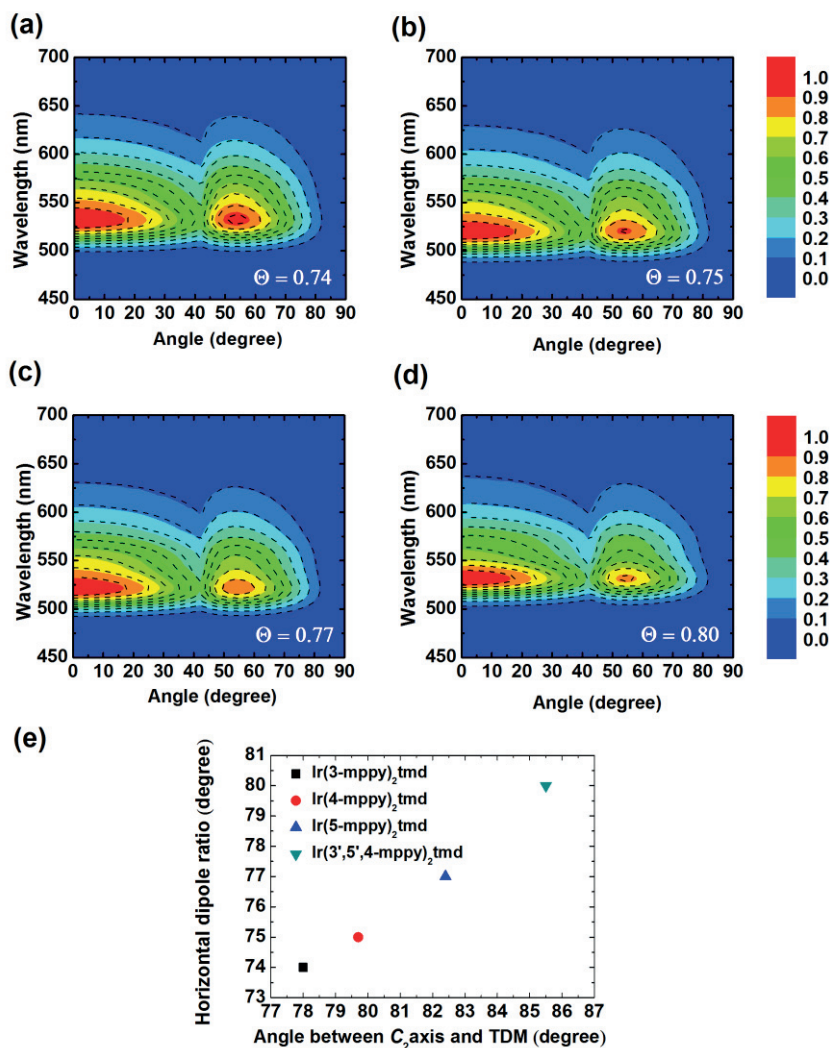


Figure 6.4 Angle-dependent PL spectra of the p-polarized light from the 32 nm thick films composed of TCTA:B3PYMPM for (a) Ir(3-mppy)₂tmd, (b) Ir(4-mppy)₂tmd, (c) Ir(5-mppy)₂tmd, and (d) Ir(3',5',4-mppy)₂tmd, respectively. Dashed lines represent theoretical fits to the experimental data. (e) The ratio of horizontal emitting dipoles (Θ) in films against the angle between the C_2 axis and TDM (Φ) of the molecules.

of Ir(ppy)₂tmd. Figure 6.4e shows the Θ values in the films against the Φ values of the molecules. Strikingly, good linear correlation can be observed in the figure. The highest Φ value of Ir(3',5',4-mppy)₂tmd resulted in the highest Θ , and the lowest Φ of Ir(3-mppy)₂tmd showed the lowest Θ among the four dyes. The excellent proportionality between Φ and Θ of the phosphorescent dyes implies that the C₂ axes of the Ir complexes doped in the films composed of TCTA:B3PYMPM are aligned almost perpendicular to the substrate on average with some distributions. These results clearly demonstrate that the direction of the TDM against the C₂ axis of heteroleptic Ir complexes is an important factor determining the orientation of the emission dipoles in films. Interaction between the Ir complexes and the host molecules must be almost the same because intermolecular interaction between the host and the dopants largely depends on the electrostatic potentials of the *N*-heterocycles of the iridium complexes and the tail of the host and the same host was used for the dyes.^{33,101} The DFT calculation showed that the electrostatic potential values of the methyl substituents and the *N*-heterocycles in the four dyes are similar (0.09–0.1 a.u.) (Figure 6.5), indicating that the Coulomb interactions between the host and the dyes must be similar despite the different positions of the methyl substituent. Therefore, the methyl substituent in the iridium complexes at different positions does not largely affect the intermolecular interaction. The photophysical data are summarized in Table 6.1.

We fabricated OLEDs using the dyes to investigate the influence of preferred horizontal orientation of the emitting dipoles on efficiency. The device structure of the OLEDs was as follows; indium tin oxide (ITO) (70 nm)/1,1-bis((di-4-

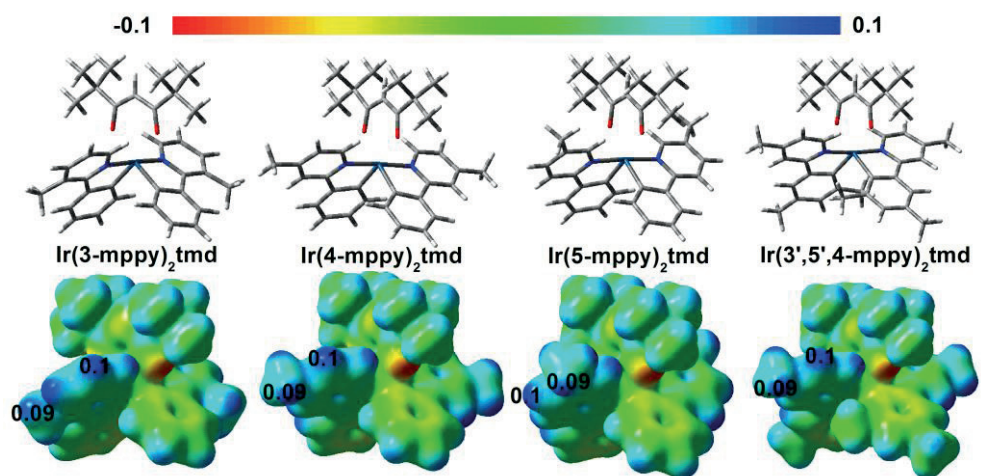


Figure 6.5 Electrostatic potential of iridium complexes. Unit of electrostatic potential is arbitrary unit.

tolylamino)phenyl)cyclohexane (TAPC) (75 nm)/TCTA (10 nm)/TCTA:B3PYMPM:8 wt% green dyes (32 nm)/B3PYMPM (45 nm)/LiF (0.7 nm)/Al (100 nm).³⁰⁻³² TCTA and B3PYMPM were used as the hole-transporting material and the electron-transporting material, respectively, and also used as the co-hosts of the EML with the molar ratio of 1:1. The co-host forms exciplex upon excitation as reported before.³⁰ We used the device structure because the device exhibited no electrical loss, low driving voltage, and low efficiency roll-off. Moreover, the device resulted in excellent match with the theoretically predicted efficiencies within $\pm 1\%$ calculated using the classical dipole model with the measured PLQY and Θ of the emitters and the refractive indices of the consisting layers under the assumptions of zero electrical loss.^{7,30,32,100} The current density–voltage–luminance (J - V - L) characteristics of the OLEDs doped with the dyes are shown in Figure 6.6a. The OLEDs showed the same turn-on voltage of 2.4 V. However the device of Ir(3',5',4-mppy)₂tmd showed higher driving voltage because the higher HOMO level of Ir(3',5',4-mppy)₂tmd plays a role as deep hole traps. The electroluminescent (EL) spectra of the devices were almost the same as the PL spectra of the dyes (inset of Figure 6.6a). The PE and the EQE of the devices are displayed in Figure 6.6b. The EQEs and PEs of the devices were calibrated using the angle-dependent emission intensity profiles (inset of Figure 6.6a). The maximum EQEs were 30.5%, 31.9%, 32.0%, and 34.1% with the standard deviation (std) of 0.5% and the maximum PEs were 145.8, 135.8, 147.5, and 157.6 lm/W with the std of 1.7 lm/W for the devices doped with Ir(3-mppy)₂tmd, Ir(4-mppy)₂tmd, Ir(5-mppy)₂tmd, and Ir(3',5',4-mppy)₂tmd, respectively. The maximum CEs were 108.1,

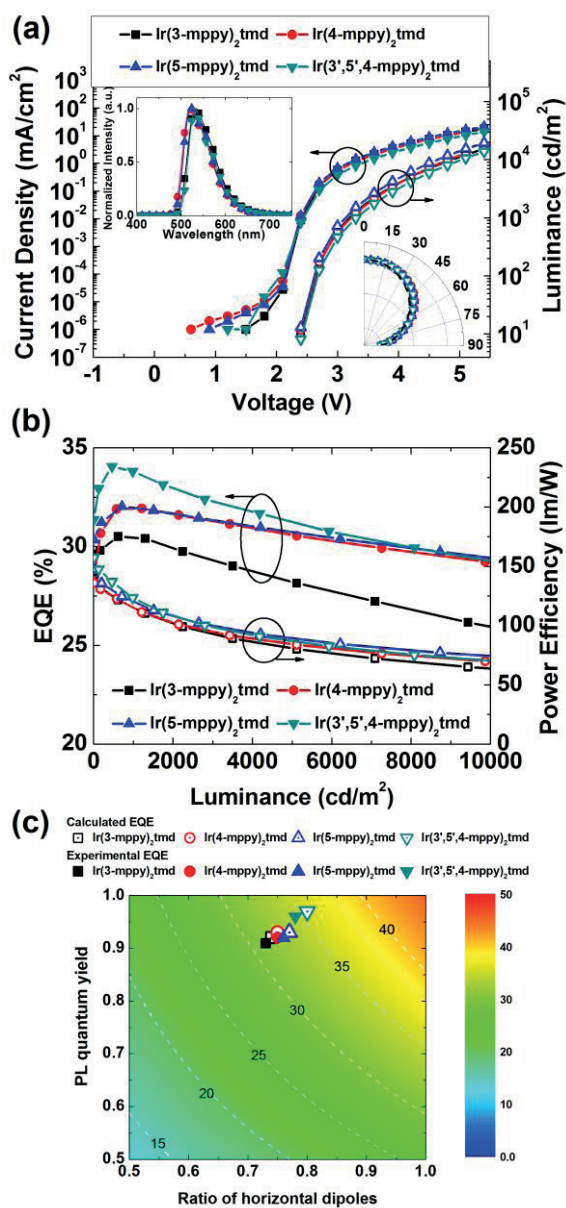


Figure 6.6 (a) The current density–voltage–luminance curves of the OLEDs. Inset: the normalized EL spectra of the OLEDs and the angular distributions of the EL intensities of the OLEDs. The dashed line in the inset shows the Lambertian distribution. (b) EQEs and power efficiencies against luminance. (c) Contour plot of the maximum achievable EQE possessing a certain PLQY and ratio of the horizontal dipoles compared with experimental EQE.

104.2, 107.5, and 120.5 cd/A with the std of 1.4 cd/A for the dyes, respectively. The EQE of 34.1% and the PE of 157.6 lm/W for the device doped with Ir(3',5',4-mppy)₂tmd are the highest efficiency reported to date for green OLEDs without any outcoupling structures. The highest EQE reported in the literature up to now is 32.3% to our best knowledge where Ir(ppy)₂tmd was used as the dopant using the same device structure as ours.³² The unprecedented high value of 157.6 lm/W originated from the high EQE combined with the low driving voltage and the spectral shift.

The experimentally obtained maximum EQEs of the devices are consistent with the maximum achievable EQEs predicted by the optical simulation based on the measured Θ s and PLQYs, as shown in Figure 6.6c.^{24,59} The contour plots of the maximum achievable EQEs were calculated as functions of PLQY and Θ under the assumption of no electrical loss. The emission zone was assumed to be located in the middle of the EML. The calculated maximum achievable EQEs of the devices doped with Ir(3-mppy)₂tmd, Ir(4-mppy)₂tmd, Ir(5-mppy)₂tmd, and Ir(3',5',4-mppy)₂tmd were 31.1%, 31.2%, 32.2%, 35.1%, respectively. These values well matched with the experimentally obtained maximum EQEs. The device of Ir(3',5',4-mppy)₂tmd having the highest Θ and PLQY exhibited the highest theoretical EQE, as well as the highest measured EQE. The device performances along with the orientation factors and the PLQYs are summarized in Table 6.2.

Table 6.2 Photophysical properties of iridium complexes and the device performances fabricated using the dyes.

Ir complex	PLQY ^{a)}		$\Phi^b)$ ($^{\circ}$)	$\Theta^c)$ (%)	EQE ^{d)} (%)	Theoretical EQE (%)	PE ^{e)} (lm/W)	CE ^{f)} (cd/A)
	(%)	(%)						
Ir(3-mppy) ₂ tmd	92	74	78.0	74	30.5	31.1	145.8	108.1
Ir(4-mppy) ₂ tmd	93	75	79.7	75	31.9	31.2	135.8	104.2
Ir(5-mppy) ₂ tmd	93	77	82.4	77	32.0	32.2	147.5	107.5
Ir(3',5',4-mppy) ₂ tmd	97	80	85.5	80	34.1	35.1	157.6	120.5

^{a)}Photoluminescence quantum yield; ^{b)}The angle between the C₂ axis and the direction of transition dipole moments; ^{c)}Horizontal dipole ratio; ^{d)} External quantum efficiency; ^{e)}Power efficiency; ^{f)}Current efficiency

6.4 Conclusion

In summary, we found that there is a strong linear correlation between the orientation of the emitting dipoles (Θ) in films and the orientation of the TDMs (Φ) against the C_2 axis of the heteroleptic Ir complexes. Higher Φ resulted in higher Θ in the same host molecules. We also showed that the methyl substitution of the hydrogen atom(s) in the pyridine and phenyl rings of a heteroleptic phosphorescent iridium complex significantly influences the orientation of the emission dipoles, as well as the angle between the C_2 axis and the direction of the transition dipole moments. Based on the observation, we were able to develop new green emitters having high horizontal orientation of phosphorescent emitting dipoles and resultantly a high performance green OLED with unprecedentedly high EQE of 34.1%, PE of 157.6 lm/W, and CE of 120.5 cd/A, respectively.

Chapter 7. Design of heteroleptic Ir complex with horizontal emitting dipoles for organic light-emitting diodes

7.1 Introduction

The orientation of emitting dipoles for organic light-emitting diodes is one of the most important material properties influencing the optical outcoupling efficiency. Horizontally oriented emitting dipoles in organic light-emitting diodes (OLEDs) lead to reduced losses from surface plasmon modes and waveguide modes, which increases the outcoupling efficiency of OLEDs.^{12,13,16-20} The theoretically predicted maximum achievable EQE is 45–55% for emitters with the emitting dipoles horizontally oriented with respect to the substrate, with a photoluminescence quantum yield (PLQY) of 100%, which is considerably higher than the EQE of 25–30% for randomly oriented emitting dipoles.^{7,23} This prediction is supported by the demonstration of an EQE of 39% using a crystal OLED with an undoped Pt complex where the emitting dipoles were horizontally oriented.¹⁰³

Horizontal orientation of the emitting dipoles has been reported for spin-coated polymer films and vacuum-evaporated films for rod- or disk-like molecules.¹²⁻¹⁷ Recently, the emitting dipoles of heteroleptic, and some homoleptic, Ir-based phosphorescent dyes were reported to exhibit a preferential orientation in doped films.^{18-20,32-34,100-102} There have been attempts to increase the fraction of horizontal emitting dipoles (Θ) by modifying the main and ancillary ligands of heteroleptic Ir complexes (HICs)^{32,102}, increasing Θ to 74–80%, and achieving EQEs

of $> 30\%$.^{32-34,102,104} It transpires that Θ is strongly dependent on the host molecules, indicating that intermolecular interactions are important in the orientation of the emitting dipoles.^{33,101} Models have been proposed to explain why some Ir complexes have a preferred orientation;^{33,105} however, it remains unclear what strategies should be followed in the design of molecules to achieve a high Θ .

There are two factors that should be considered to understand the preferred orientation of Ir complexes: the symmetry of the transition dipole moment (TDM) in a specific molecule, and the orientation of that dopant molecule in a film of host molecules.^{32,33,105} The degeneracy of the TDMs and their relative orientations in the molecule must be taken into account in the molecular symmetry. High values of Θ are expected for HICs if the emitting dipole vectors are perpendicular to the C_2 axes in the molecules, and the doubly degenerated TDMs are parallel to the substrate. The influence of the orientation of the transition dipoles in a molecule with respect to the C_2 axis on Θ (i.e. the average dipole orientation in films) was investigated by slight modifications to the main phenyl pyridine (ppy) ligands; i.e. by substituting methyl group(s) at different positions of ppy with the same ancillary ligand in the same host to minimise variations in the intermolecular interactions (or the molecular axis against the substrate) in the film.¹⁰² The larger the angle (Φ) between the C_2 axis and the emitting dipole vector, the larger the value of Θ . A value of $\Theta = 80\%$ was obtained from an Ir complex where the angle between the C_2 axis and the emitting dipole vector was almost 90° ; this may be the limit that is achievable using this approach.^{33,102} This limitation may result from variations in the alignment of the TDMs of the molecules with respect to the direction parallel to the surface in a doped

amorphous film. This can be represented as the average and the standard deviation of the angle between the TDMs of the molecules and the film surface. Therefore, we may expect that it will be valuable in the design of molecules such that their TDMs are parallel to the surface.

Here, we show that orienting Ir complexes with the TDMs parallel to the substrate is possible if they are elongated by substituting conjugated functional moieties at the para-position of the pyridine in the main ligands. We demonstrate values of Θ up to 86.5%, obtaining unprecedentedly high-efficiency yellow and green OLEDs, with EQEs of 38% and 36%, respectively.

7.2 Experimental

Materials. New Ir complexes were designed by K.-H. Kim and J.-J. Kim at Seoul National University and synthesized by Y.-H. Kim and E. S. Ahn at Gyeongsang National University. The hole- and electron-transport materials (> 99%) were purchased from Nichem Fine Technology Co., Ltd (Hsinchu County, Taiwan). Al and LiF were purchased from Meterion (Fremont, CA, USA).

DFT calculations. Optimized geometries and HOMO and LUMO frontier orbitals were calculated using Gaussian 09.⁶⁴ Geometry optimization of the triplet states was performed using the B3LYP exchange–correlation functional, where the ‘double- ξ ’ quality LANL2DZ basis was used for the Ir atom, and the 6-31G+(d) basis set was used for all other atoms. A pseudopotential (LANL2DZ) was used to describe the inner core electrons of the Ir atom. The triplet transition properties of the Ir complexes were investigated using quantum chemistry calculations, implemented via the Jaguar package^{106,107} that is included in Schrödinger Materials Science Suite¹⁰⁸. Geometry optimization of triplet states was performed using the B3LYP exchange–correlation functional, with the LACVP** basis set for all atoms. The triplet energies and triplet TDMs of the Ir complexes were determined using time-dependent DFT (TD-DFT) calculations, where the spin-orbit Hamiltonian was described using the Tamm–Dancoff approximation. The B3LYP exchange–correlation functional was used with the DYALL-2ZVCP_ZORA-J-PT-GEN basis set for all atoms, and the spin-orbit zeroth order regular approximation (ZORA) was used to calculate relativistic effects.

Analysis of emitting dipole orientation. The orientation of the dipoles of Ir complex was determined based on angle-dependent PL using a classical dipole model.^{7,17} This model allows for separate calculation of the *p*- and *s*-polarised optical emissions from horizontally and vertically oriented dipoles in a non-absorbing anisotropic medium. The experimental setup has been reported previously.^{7,17} Briefly, it consisted of a motorised rotation stage, a half cylinder lens with a sample holder, a dichroic mirror to filter the excitation beam, a polariser to select the polarisation of the emitted light, and a fibre optic spectrometer (Maya2000; Ocean Optics, Oxford, UK). An He-Cd continuous-wave laser (325 nm; Melles Griot, Rochester, NY, USA) was used as the excitation source. The emitting films were thermally deposited on a 1-mm-thick fused silica substrate and encapsulated under an N₂ atmosphere prior to use. *P*-polarised light was used to analyse the orientation of the dipoles in the films.

Device fabrication and characterization. OLEDs were fabricated on cleaned glass substrates that were pre-patterned with 70-nm-thick ITO, which were formed using thermal evaporation at a pressure of 5×10^{-7} Torr without breaking the vacuum. Prior to deposition of the organic layers, the ITO substrates were pre-cleaned using isopropyl alcohol and acetone, then exposed to ultraviolet–ozone for 10 min. Each layer was deposited at a rate of 1 Å/s, and the total deposition rate of the co-deposited layers was 1 Å/s. Current density, luminance, and EL spectra were measured using a programmable source meter (Keithley 2400; Keithley Instruments, Cleveland, OH, USA) and a spectrophotometer (Spectrascan PR650; Photo Research Inc., Chatsworth, CA, USA), which measures power per steradian per unit wavelength per unit area (in units of W/(nm·sr·m²)). Luminance was calculated based on the

measured optical power considering the CIE luminosity function. The angular distribution of the EL was measured using a programmable source meter (Keithley 2400), a goniometer, and a fibre optic spectrometer (Ocean Optics S2000). The EQE and PE were calculated based on the J - V - L characteristics, EL spectra and angular distributions of the EL intensity.

7.3 Result and discussion

Figure 7.1 shows the chemical structures of Ir complexes used in this work, together with optimized geometries and the triplet TDMs of the Ir complexes. The 4-position of pyridine of bis(2-(3,5-dimethylphenyl)-4-methylpyridine) Ir (III) (2,2,6,6-tetramethylheptane-3,5-diketonate) $[\text{Ir}(\text{3',5',4-mppy})_2\text{tmd}]^{102}$ was substituted with functional groups such as a trifluoromethyl (CF_3) group, which is strongly electron withdrawing, as well as with a propyl group, which is elongated, and with a phenyl group, which is planar and charge conjugated, creating the following compounds: bis(2-(3,5-dimethylphenyl)-4-(trifluoromethyl)pyridine) Ir (III) (2,2,6,6-tetramethylheptane-3,5-diketonate) $[\text{Ir}(\text{dmppy-CF}_3)_2\text{tmd}]$, bis(2-(3,5-dimethylphenyl)-4-propylpyridine) Ir (III) (2,2,6,6-tetramethylheptane-3,5-diketonate) $[\text{Ir}(\text{dmppy-pro})_2\text{tmd}]$ and bis(2-(3,5-dimethylphenyl)-4-phenylpyridine) Ir (III) (2,2,6,6-tetramethylheptane-3,5-diketonate) $[\text{Ir}(\text{dmppy-ph})_2\text{tmd}]$.

Geometry optimisations and calculations of the frontier orbitals of the T_1 states were implemented using the density functional theory (DFT) package Gaussian 09,⁶⁴ where the triplet energies and TDMs of the molecules were found using time-dependent calculations, and where spin-orbit coupling was included using the quantum chemistry package Jaguar^{106,107} (part of the Schrödinger Materials Science Suite¹⁰⁸). Details of calculations are given in the experimental section. $\text{Ir}(\text{dmppy-pro})_2\text{tmd}$ and $\text{Ir}(\text{dmppy-ph})_2\text{tmd}$ have relatively high aspect ratios of 1.81 and 1.99, respectively (*c.f.* 1.34 for $\text{Ir}(\text{3',5',4-mppy})_2\text{tmd}$ and $\text{Ir}(\text{dmppy-CF}_3)_2\text{tmd}$). The dihedral angle between the pyridine and phenyl groups at the 4-position of the

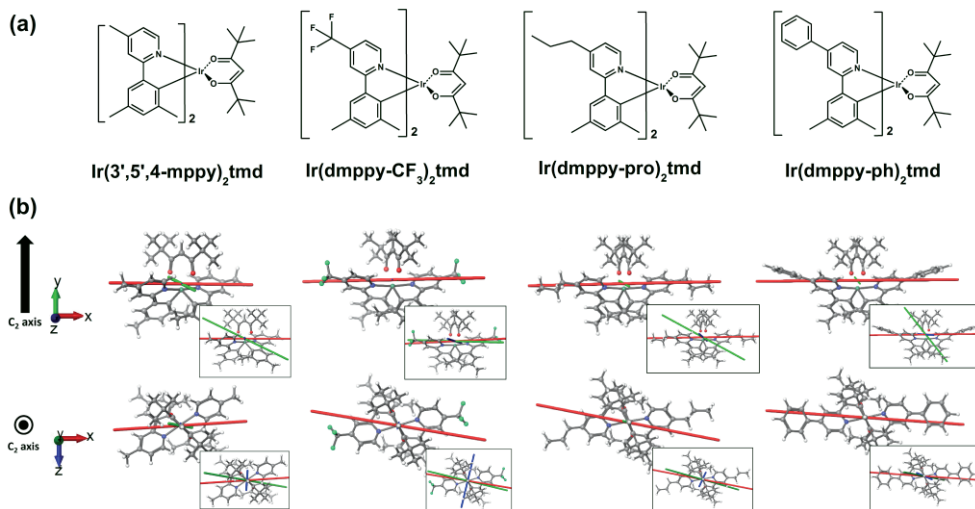


Figure 7.1 (a) Chemical structures and (b) optimized geometries along with triplet transition dipole moments of $\text{Ir}(3',5',4\text{-mppy})_2\text{tmd}$, $\text{Ir}(\text{dmppy-CF}_3)_2\text{tmd}$, $\text{Ir}(\text{dmppy-pro})_2\text{tmd}$, and $\text{Ir}(\text{dmppy-ph})_2\text{tmd}$ from three sublevels are shown as bars based on the center of mass. The transition dipole moments of the T_x , T_y , T_z sublevels correspond to the blue, green, and red bars, respectively. Scaled TDMs were shown in inset of Figure 1(b).

pyridine of Ir(dmppy-ph)₂tmd was 23°. The small dihedral angle enables conjugation between the phenyl and pyridine groups, resulting in sufficiently large dipole length in the horizontal direction.

The triplet TDMs of T_x, T_y and T_z sublevels of the HICs are shown by the bars in Figure 7.1. The triplet TDMs of all the Ir complexes were aligned almost vertically with the C₂ axis (see Tables 7.1 and 7.2). The TDMs and oscillator strengths of the T₁ transition of Ir(dmppy-CF₃)₂tmd and Ir(dmppy-ph)₂tmd were significantly larger than those of Ir(dmppy-pro)₂tmd and Ir(3'5',4-mppy)₂tmd. This is attributed to conjugation between the pyridine and phenyl substituents of Ir(dmppy-ph)₂tmd, the increased dipole length, and the phenyl and CF₃ substituents at the 4-position of pyridine pull the large amount of electrons at the lowest unoccupied molecular orbital (LUMO) (see Figure 7.2). Thus, the contributions of the ligand-centred (LC) orbitals of Ir(dmppy-CF₃)₂tmd and Ir(dmppy-ph)₂tmd were almost twice that of Ir(3',5',4-mppy)₂tmd, resulting in increased oscillator strengths for Ir(dmppy-CF₃)₂tmd and Ir(dmppy-ph)₂tmd. By contrast, the LUMO and highest occupied molecular orbital (HOMO) of Ir(3',5',4-mppy)₂tmd and Ir(dmppy-pro)₂tmd exhibited similar electron distributions (see Figure 7.2); therefore the metal-to-ligand charge transfer (MLCT) and LC of the two emitters were similar (Table 7.1).

Figure 7.3a shows photoluminescence (PL) and absorption spectra of HICs in solution. The absorption at 300–400 nm can be assigned to a spin-allowed singlet MLCT (¹MLCT) transition, and the weak absorption at 430–500 nm can be assigned to a spin-forbidden triplet LC (³LC) and/or triplet MLCT (³MLCT) transitions. The

Table 7.1 Photophysical properties and DFT results of Ir complexes.

Ir complex	PLQY ^a [%]	Θ [%]	Aspect ratio	Φ [°]	MLCT ^b [%]	LC ^b [%]
Ir(3',5',4-mppy) ₂ tmd	97	79	1.34	88.2	32.6	19.2
Ir(dmppy-CF ₃) ₂ tmd	75	80	1.34	88.1	32.7	45.7
Ir(dmppy-pro) ₂ tmd	98	83.5	1.81	88.2	32.3	19.7
Ir(dmppy-ph) ₂ tmd	98	86.5	1.99	89.1	35.2	47

^aMeasured using 50-nm-thick TCTA:B3PYMPM films doped with 4 wt% HICs. ^bContribution of the frontier orbitals of HICs to the triplet transitions from HOMO to LUMO level

Table 7.2 Calculated triplet transition properties of HICs using TD-DFT calculations to consider spin-orbit coupling.

	Energy (nm)	Oscillator strength (a.u.)	Transition dipole moment (a.u.) ^a			Φ (°)
			x	y	z	
Ir(3',5',4-mppy) ₂ tmd	620	7.86E-07	0.001	-0.0018	-0.0136	88.2
	620	6.16E-05	-0.059	0.0299	-0.0116	
	616	1.52E-03	-0.3324	0.0071	0.02	
Ir(dmppy-CF ₃) ₂ tmd	681	7.20E-06	-0.0063	0.0032	0.0269	88.1
	680	1.63E-05	0.0404	-0.002	0.0096	
	674	4.80E-03	0.7025	0.0174	0.1133	
Ir(dmppy-pro) ₂ tmd	619	2.05E-06	0.0041	-0.0037	-0.008	88.2
	618	5.60E-05	-0.0437	0.0223	-0.0131	
	615	1.96E-03	-0.8362	-0.0345	-0.1683	
Ir(dmppy-ph) ₂ tmd	661	1.82E-06	0.0057	-0.0004	0.0022	89.1
	660	3.07E-05	-0.0153	0.0198	-0.0027	
	655	1.77E-02	0.6025	0.0019	0.022	

^a x,y,z components of triplet transition dipole moments in Cartesian coordinates.

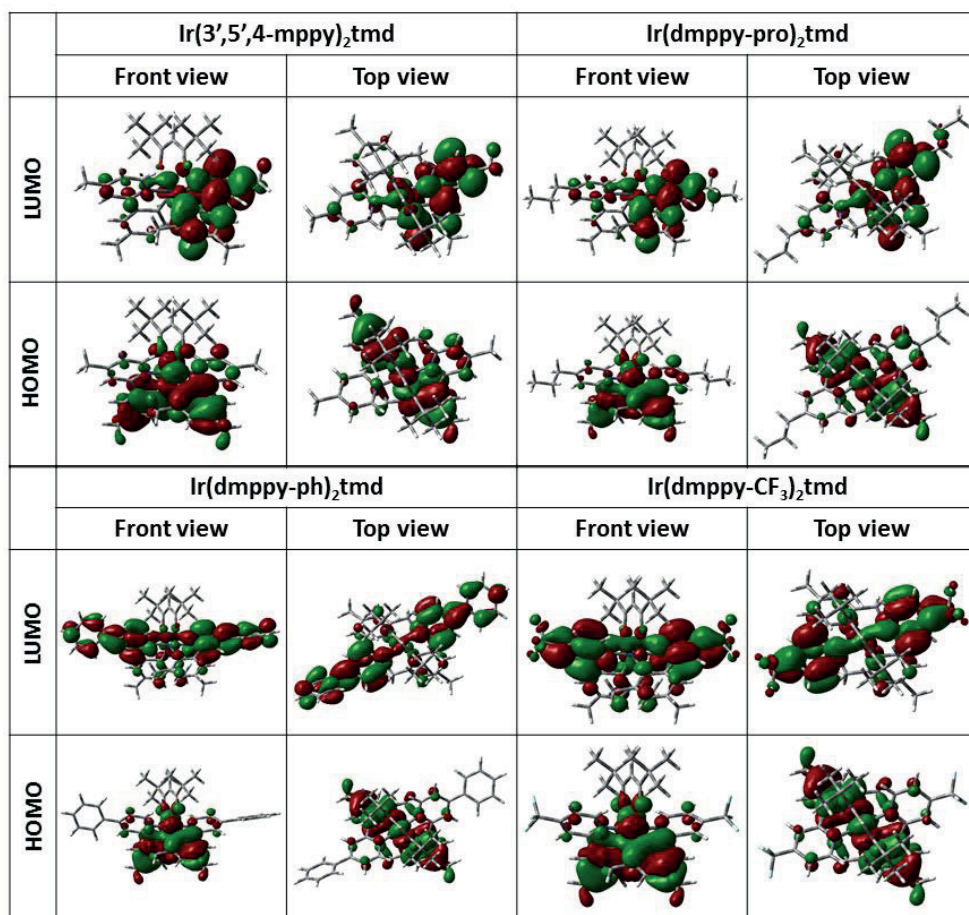


Figure 7.2 The frontier molecular orbitals of the HICs at triplet state, calculated using the density functional theory with B3LYP/6-31+G(d) for C, H, N, O and LANL2DZ for Ir as basis set.

peak wavelengths of the PL spectra were 587 nm for Ir(dmppy-CF₃)₂tmd, 532 nm for Ir(3',5',4-mppy)₂tmd and Ir(dmppy-pro)₂tmd, 579 nm for Ir(dmppy-ph)₂tmd. The HOMO levels of the compounds were measured using cyclic voltammetry, and the LUMO levels were calculated from the HOMO levels and the optical bandgaps; these data are listed in Table 7.3. The PLQYs of 4 wt% HICs doped in a 4,4',4''-tris(*N*-carbazolyl)-triphenylamine (TCTA): bis-4,6-(3,5-di-3-pyridylphenyl)-2-methylpyrimidine (B3PYMPM) co-host film were 97 ± 2%, 75 ± 2%, 98 ± 2%, and 98 ± 2%, for Ir(3',5',4-mppy)₂tmd, Ir(dmppy-CF₃)₂tmd, Ir(dmppy-pro)₂tmd and Ir(dmppy-ph)₂tmd, respectively.

The orientation of the emitting dipoles of the Ir complexes doped at 4 wt% into 30-nm-thick TCTA:B3PYMPM films was determined based on angle-dependent PL spectra (Figure 7.3b)^{7,17} using a classical dipole model considering the birefringence of the film.¹⁰⁰ Figure 7.4 shows the angle-dependent *p*-polarized PL intensities at various wavelengths. The measured angle-dependent PL spectra were well fitted by Θ values of 79% for Ir(3',5',4-mppy)₂tmd, 80% for Ir(dmppy-CF₃)₂tmd, 83.5% for Ir(dmppy-pro)₂tmd, and 86.5% for Ir(dmppy-ph)₂tmd. Note that larger values of Θ correspond to a greater degree of parallel orientation of TDMs of the molecules in the films, rather than orientation of the TDM against the C₂ axis in the molecules; this is because the TDMs are almost 90° with respect to the C₂ axis for all molecules. Parallel orientation of Ir-N bonds with the substrate becomes more effective as the aspect ratio of the molecules increases, which corresponds to substitution of an elongated group (propyl and phenyl), and to the strength of the host-dopant π - π interactions increasing due to the substituent being a planar

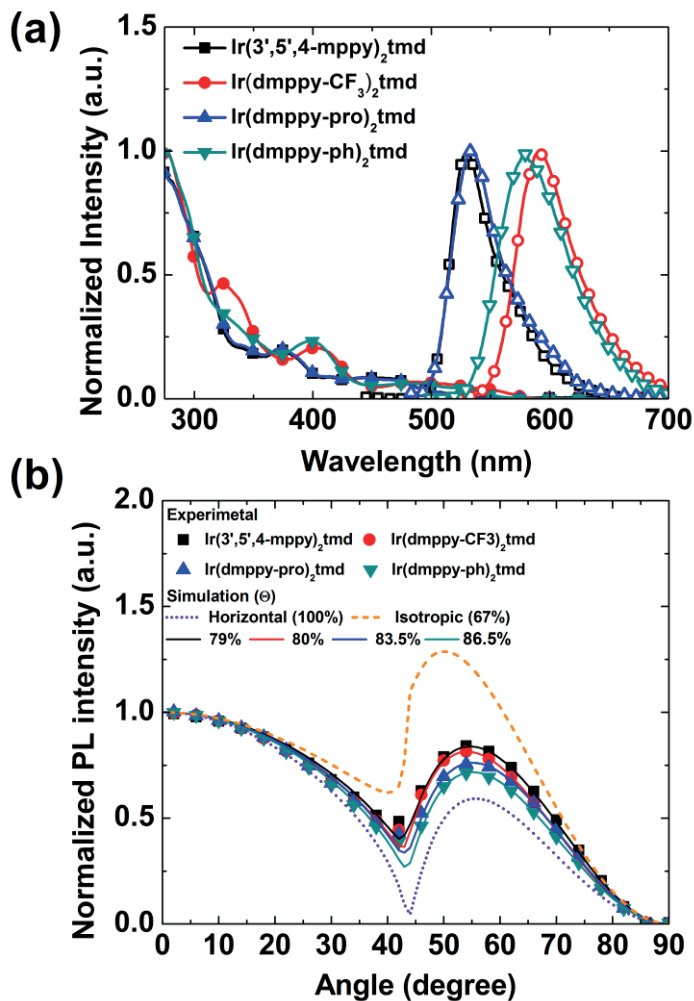


Figure 7.3 (a) Absorption (close scatter) and PL spectra (open scatter) of Ir complexes in chloroform. (b) Angle-dependent PL intensities of the p-polarized light from the 30 nm thick films composed of TCTA:B3PYMPM: 4 wt% Ir complexes measured at 530 nm for $\text{Ir}(3',5',4\text{-mppy})_2\text{tmd}$ and $\text{Ir}(\text{dmppy-pro})_2\text{tmd}$, 570 nm for $\text{Ir}(\text{dmppy-ph})_2\text{tmd}$, and 590 nm for $\text{Ir}(\text{dmppy-CF}_3)_2\text{tmd}$, respectively.

Table 7.3 Photophysical and electronic properties of HICs

Ir complex	Absorption ^a [nm]	HOMO [eV]	LUMO [eV]	PL ^a [nm]
Ir(3',5',4-mppy) ₂ tmd	265, 374, 455	-5.06	-2.72	530
Ir(dmppy-CF ₃) ₂ tmd	276, 326, 402, 481	-5.04	-2.89	589
Ir(dmppy-pro) ₂ tmd	263, 373, 441	-5.10	-2.77	532
Ir(dmppy-ph) ₂ tmd	276, 398, 481	-5.18	-2.97	579

^aMeasured in a CHCl₃ solution at 297 K.

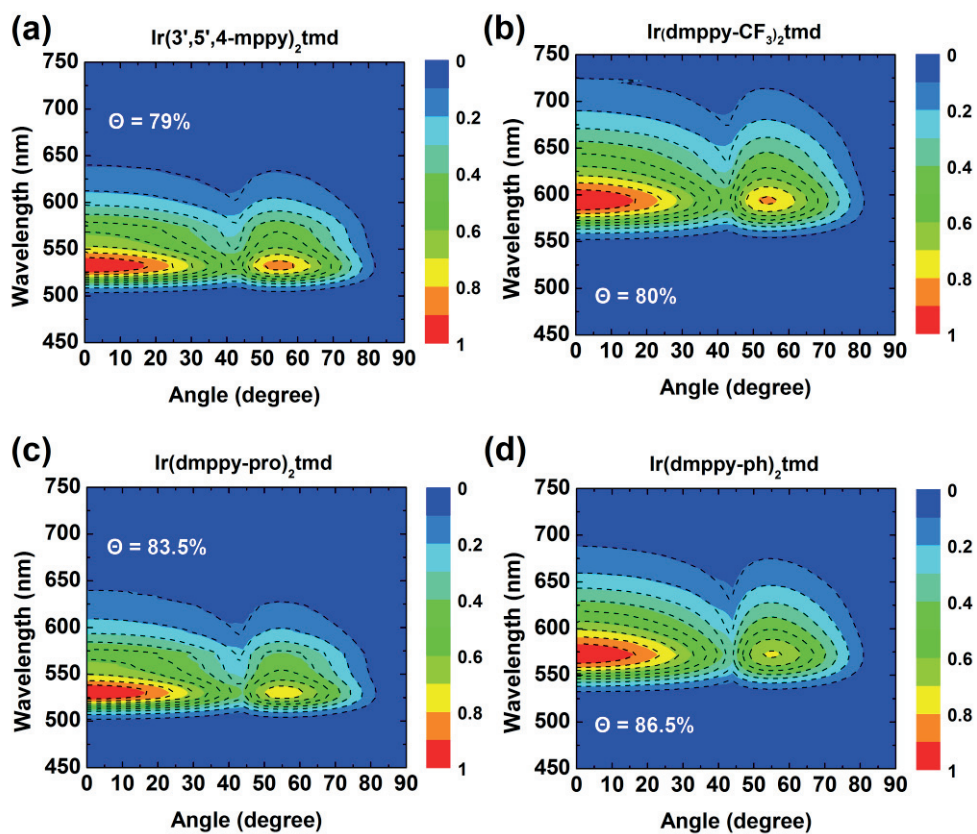


Figure 7.4 Angle-dependent PL spectra for (a) $\text{Ir}(3',5',4\text{-mppy})_2\text{tmd}$, (b) $\text{Ir}(\text{dmppy-CF}_3)_2\text{tmd}$, (c) $\text{Ir}(\text{dmppy-pro})_2\text{tmd}$, and (d) $\text{Ir}(\text{dmppy-ph})_2\text{tmd}$, respectively. Dashed lines represent theoretical fits to the experimental data.

conjugated group (phenyl) rather than to a strong intermolecular interaction with an electron-withdrawing substituent group such as CF₃.

We fabricated OLEDs using these dyes to investigate the influence of the preferred horizontal orientation of the emitting dipoles on the efficiency of the devices. The device structure was as follows: indium tin oxide (ITO) (70 nm)/1,1-bis((di-4-tolylamino)phenyl)cyclohexane (TAPC) (75 nm)/TCTA (10 nm)/TCTA:B3PYMPM: 4 wt% green dyes (30 nm)/B3PYMPM (45 or 55 nm) / LiF (0.7 nm)/Al (100 nm). TCTA was used as the hole-transport material, with B3PYMPM used as the electron-transport material. These two compounds were also used as the exciplex-forming co-hosts of the EML, where the molar ratio was 1:1.³⁰ The thickness of the B3PYMPM layer was 45 nm for Ir(3',5',4-mppy)₂tmd and Ir(dmppy-pro)₂tmd, compared to 55 nm for Ir(dmppy-ph)₂tmd and Ir(dmppy-CF₃)₂tmd. The device results of Ir(3',5',4-mppy)₂tmd are from ref. 102. Figure 7.5a shows the current density–voltage–luminance (*J-V-L*) characteristics of these OLEDs. The OLEDs all exhibited turn-on voltages of 2.4 V. The electroluminescence (EL) spectra of the devices were almost identical to those of the PL spectra of the dyes (Figure 7.5b). The power efficiencies (PEs) and current efficiencies (CEs) of the devices are shown in Figure 7.5c, and the EQEs are shown in Figure 7.5d. The EQE and PE were calibrated using angle-dependent emission intensity profiles (see the inset of Figure 7.5a). The maximum EQEs were 34.1%, 25.5%, 36.0% and 38.1% for the devices doped with Ir(3',5',4-mppy)₂tmd, Ir(dmppy-CF₃)₂tmd, Ir(dmppy-pro)₂tmd, and Ir(dmppy-ph)₂tmd, respectively; the corresponding PEs were 123, 51, 139 and 108 lm W⁻¹ at 1,000 cd m⁻², and the

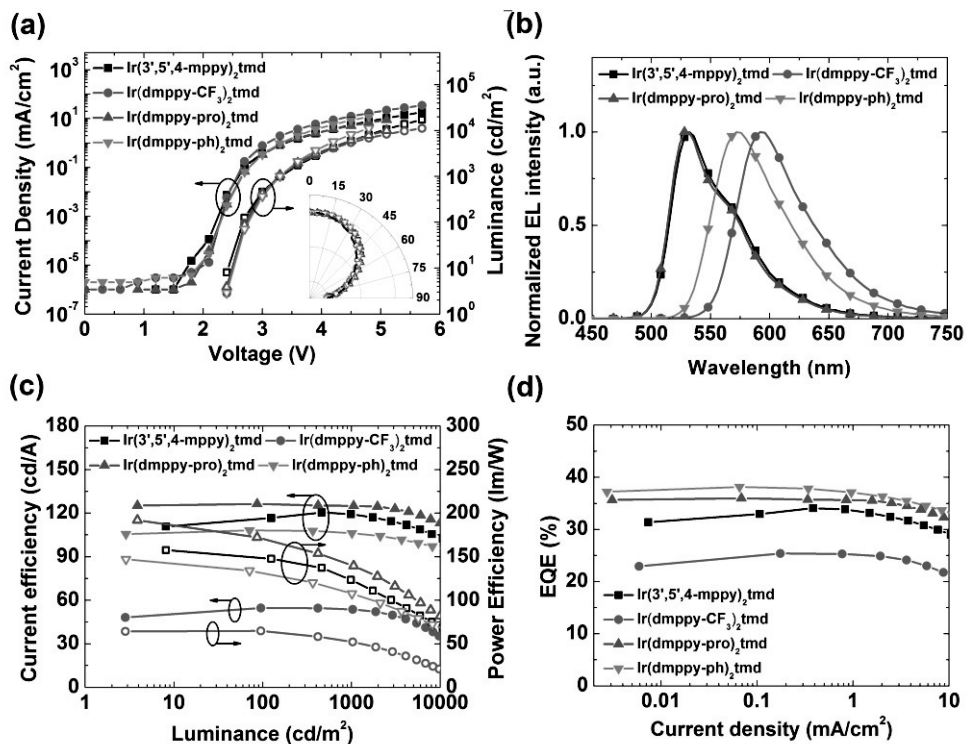


Figure 7.5 (a) Current density–voltage–luminance characteristics (b) EL spectra, (c) current efficiency and power efficiency as a function of the luminance of OLEDs, and (d) EQEs as a function of the current density with different Ir complexes as dopants. Inset of (a) shows the angular distributions of the EL intensities of the OLEDs with the dashed line of the Lambertian distribution.

maximum respective CEs of the dyes were 120, 54, 126 and 108 cd A⁻¹. The EQE of 36.0% for the green OLED that was doped with Ir(dmppy-pro)₂tmd, and the EQE of 38.1% for the yellow OLED that was doped with Ir(dmppy-ph)₂tmd, represent the highest efficiencies yet reported for Ir-based phosphorescent OLEDs with no outcoupling structures. This is attributed to the large values of Θ and PLQY. To the best of our knowledge, the highest previously reported EQEs are 34.1% for a green OLED and 27.2% for a yellow OLED.^{102,109} The experimentally measured EQEs reported here are in good agreement with the calculated maximum achievable EQEs of 27.2%, 36.4%, and 38.2% for Ir(dmppy-CF₃)₂tmd, Ir(dmppy-pro)₂tmd, and Ir(dmppy-ph)₂tmd, OLEDs respectively (these calculations were based on measured values of Θ and PLQY and assumed no electrical losses.)

7.4 Conclusion

In conclusion, we have shown that HICs can be aligned with the Ir-N bonds and TDMs parallel to the surface of doped films if the molecules have an elongated structure with a high aspect ratio, and exhibit strong intermolecular interactions between the donor and the host molecules. Ir-based complexes with unprecedentedly large horizontal emitting dipoles were formed in doped films by substituting functional groups at the 4-position of pyridine in the ppy main ligands, allowing it to realise high EQEs of 38.1% for a yellow OLED and 36% for a green OLED. Substituents at the 4-position of the pyridine ring significantly affect the molecular orientation of HICs. Although this approach was developed using HICs, it may also be applied to homoleptic Ir complexes.

Chapter 8. Crystal organic light-emitting diodes with perfectly oriented non-doped Pt-based emitting layer

8.1 Introduction

Organic semiconductor materials have gained widespread popularity for electrical and optical devices because they are light weighted, flexible, transparent, and easily processable. In recent years, ordered organic materials come to the fore to enhance the performance of organic optoelectronic and electronic devices because preferred orientation of organic materials can significantly enhance charge carrier mobility,^{110,111} absorption of organic photovoltaic materials,¹¹²⁻¹¹⁶ and outcoupling efficiency of organic light-emitting diodes (OLEDs).^{7,12-20} In this respect, organic single crystals have exhibited big advantages in the device performance over amorphous or polycrystalline organic films, especially in organic field effect transistors because of the perfect molecular orientation and arrangement of organic materials. Hence, efforts have been poured into growing highly oriented polycrystalline thin films for organic transistors to realize high charge carrier mobility.^{110,111,117-119} However, organic crystal has been rarely used for OLEDs because crystals of most phosphorescent emitters exhibit low photoluminescence quantum yield (PLQY) due to concentration quenching,⁷⁴ and trapped holes and electrons at grain boundaries. Moreover, rough surface results in high leakage current and low device stability. Because of these reasons, majority of researchers

have focused on the amorphous organic film by substituting bulky substituents on chromophore and emitters doped in host matrix instead of growing highly oriented crystalline films. Apparently, amorphous organic layers increase the driving voltage due to low electron and hole mobilities in OLEDs. Orientation of emitting dipoles is one of the most important material properties influencing outcoupling efficiency along with the refractive indices of the consisting materials. Recently, it has been theoretically predicted that external quantum efficiency (EQE) over 45% can be realized without any extra light extraction structures using horizontally oriented emitting dipoles parallel to the substrate compared to 25%–30% for randomly oriented emitting dipoles if the emitter has 100% PLQY and the device has no electrical loss.⁷ Some iridium complexes and thermally activated delayed fluorescence (TADF) emitters have shown the possession of preferred horizontal transition dipole ratio (Θ) of 70%–82% and demonstrated high EQEs over 30% without any outcoupling layers.^{7,50,32-33,102} However, it will be difficult to obtain an even higher Θ due to the amorphous nature of typical emitting layers. In this regard, organic crystals would be the better emitters because of the orientational and positional ordering.

Among the various phosphorescent emitters, Pt complexes can be one of the best candidates to form organic crystals because they have d^8 square planar structure and d_z^2 orbital placed to the molecular plane, leading to strong metal–metal interaction between Pt complexes.^{120,121} Chi and co-workers synthesized a series of columnar stacked Pt(II) pyridyl azolate complexes.¹²²⁻¹²⁴ The stacking was strongly influenced by the ligating substituents and the complexes with the CF_3 -substituted

pyrazolate ligands such as Pt(II)bis(3-(trifluoromethyl)-5-(2-pyridyl)-pyrazolate) [Pt(fppz)₂] showed strong tendency toward the formation of columnar structure with short Pt–Pt distances, as well as large red shift in photoluminescent (PL) and electroluminescent (EL) spectra in solid state. Cocchi and co-workers observed similar results using Pt(II) complexes bearing both phenylpyridine (ppy) and 2-(pyridyl)tetrazolate (2-PTZ) chelates, and observed that the F substituents on Pt(F2ppy)(2-PTZ) promote the molecular self-assembly into more uniform ordered structures in neat thin films.¹²⁵ Formation of the crystalline thin films was previously demonstrated using a platinum porphyrin derivative.¹¹¹ Both groups (Chi and Cocchi) fabricated red emitting OLEDs using the neat crystalline thin films based on the Pt complexes as the emitting layers with the EQEs of 2% and 8%, respectively.^{122,125} In contrast, many of the highly efficient Pt complexes did not show ordered crystalline packing.¹²⁶⁻¹²⁹ Recently Wang and co-workers reported that the neat film of Pt(fppz)₂ exhibits the PLQY of 96% and demonstrated an OLED with a remarkably high EQE of 31.1% using the same as the emitting layer.¹³⁰ However, orientation of emitting dipoles and crystal properties of non-doped emitting layer were not discussed.

Here, we investigated the emitting dipole orientation of the thin films fabricated using Pt complexes and discussed the structural relationship between X-ray structural analyses and structures in thin films based on quantum chemical calculations. Crystal structures are largely influenced by the symmetry of the molecules. Interestingly enough, the emitting dipole orientation and the PLQY of the thin-film crystal layers were largely affected not only by the crystallinity of the emitting layer but also by the molecular arrangement in the crystal. We realized

highly oriented emitting dipoles with the horizontal emitting dipole ratio of 93% and the PLQY of 96% and resultantly an unprecedentedly high efficiency OLED with the EQE 38.8% using the Pt(fppz)₂ based perfectly oriented thin film crystal as the emitting layer.

8.2 Experimental

Materials. Hole transporting and electron transporting materials (>99%) were purchased from Nichem Fine Technology Co., Ltd (Hsinchu County, Taiwan). Al and LiF were purchased from Meterion (United States). Pt complexes were synthesized by Y. Chi and co-workers in National Tsing Hua University.

Pt complex thin film fabrication. Films were fabricated on substrate under a pressure of 5×10^{-7} Torr by thermal evaporation without any pre- and post-treatments. The deposition rate of the Pt complex layers was 0.18 \AA/s .

Grazing incident wide-angle X-ray diffraction (GIWAXD) measurements. GIWAXD measurements were performed at 5A scattering beamline for materials science at the Pohang Light Source II (PLS-II) in Korea. X-rays with 11.57 keV energy and 2D image plate were used for the measurement.

PL measurements. PL spectra of the organic materials were measured using samples thermally deposited on fused silica under a vacuum of 5×10^{-7} Torr. The samples were excited with a He/Cd laser (325 nm) to detect PL using a photomultiplier tube attached to a monochromator.

Measurement and simulation of angle-dependent PL spectra. The dipole orientations of Pt complex thin films were determined by analyzing the angle-dependent PL of the film using the classical dipole model. This model allows for the separate calculation of the p- and s-polarized light emission from horizontally and vertically oriented dipoles in a non-absorbing anisotropic medium. The principle of the characterization of the emitting dipole orientation in a birefringent medium was

described in the reference 100. The refractive indices of the Pt complex thin films were measured using VASE. The incident angle was varied from 45° to 75° in steps of 5°.

The experimental setup was reported previously^{7,17} and is composed of a half cylinder lens with a sample holder on a motorized rotation stage, a dichroic mirror to filter the excitation beam, a polarizer to select the polarization of the emitted light and a fiber optic spectrometer (Ocean Optics Maya2000). A He-Cd continuous wave laser light (325 nm, Melles Griot) used as the excitation source was guided by an optical fiber which is fixed behind of sample holder at an angle of 45°. Emitting layers were thermally deposited on a 1-mm-thick fused silica substrate and encapsulated under N₂ atmosphere before use for the angle-dependent PL measurements. P-polarized light was used to analyze the orientation of the dipoles in the films.

Transient PL measurement. Transient PL was measured by using a pulsed N₂ laser (KEN-2X, USHO) as the excitation light source and a streak camera (C10627, Hamamatsu) as the optical detection system.

Device fabrication. The OLEDs were fabricated on clean glass substrates pre-patterned with 100-nm-thick indium tin oxide (ITO) under a pressure of 5×10^{-7} Torr by thermal evaporation without breaking the vacuum. Before the deposition of the organic layers, the ITO substrates were pre-cleaned with isopropyl alcohol and acetone, then exposed to ultraviolet-ozone for 10 min.

Device characterization. The current densities, luminance intensities and EL

spectra were measured using a programmable source meter (Keithley 2400) and a spectrophotometer (Spectrascan PR650, Photo Research). The angular distribution of the EL was measured with a programmable source meter (Keithley 2400), a goniometer, and a fiber optic spectrometer (Ocean Optics S2000). The EQE and the power efficiency of the OLEDs were calculated from their J - V - L characteristics, their EL spectra and the angular distribution of the EL intensity.

Density functional theory (DFT) calculations on the platinum complexes.

Quantum chemical calculations based on DFT were carried out using Gaussian 09 program.⁶⁴ The ground state geometry optimization were performed using M062X exchange–correlation functional, the ‘double- ξ ’ quality LANL2DZ basis set for the Pt atom, and the 6-31G+(d) basis set for all other atoms. A pseudo potential (LANL2DZ) was applied to replace the inner core electrons of the Pt atom.

8.3 Result and discussion

Three Pt complexes were synthesized to investigate the effect of the symmetry of the molecules and photophysical properties, whose structural drawings are shown in Figure 8.1a-c. Pt(fppz)₂ possesses two-fold rotational symmetry, Pt(II)(5,5'-di(trifluoromethyl)-3,3'-bipyrazolate)(2,2'-bipyridine) [Pt(f2bipz)(bpy)] possesses a mirror symmetry, but Pt(II)(3-(trifluoromethyl)-5-(2-pyridyl)pyrazolate)(picolinate) [Pt(fppz)(pic)] does not have the mirror or rotational symmetry caused by the picolinate ancillary ligand. All the compounds are composed of two pyridyl units and at least one CF₃-substituted pyrazolate unit to promote the molecular self-assembly into more ordered structures and packing in neat films.^{122,125} The ground state geometries and isosurfaces of the molecular electrostatic potential (ESP) of the Pt complexes calculated using DFT are shown in Figure 8.1d-f. The ESP of the Pt complexes was calculated with M062X level of theory without symmetry constraints. The isosurfaces of the studied molecules show that there are highly electropositive spots (0.12–0.15 a.u.) at the hydrogen atoms of pyridine and electronegative spots (–0.04–0.03 a.u.) at the fluorine atoms of CF₃-substituted pyrazolate ligands, which will induce strong coulomb interactions between molecules. Pt(f2bipz)(bpy) has stronger electropositivity at the hydrogen atoms of pyridine and electronegative spots in the CF₃-substituted pyrazolates than those of Pt(fppz)₂ and Pt(fppz)(pic). The oxygen of Pt(fppz)(pic) exhibited the strongest electronegativity (–0.1 a.u.) in the molecules.

The energetics of the Pt complexes as dimer were calculated with geometries based on the single-crystal X-ray diffraction (XRD) data of Pt(fppz)₂ and

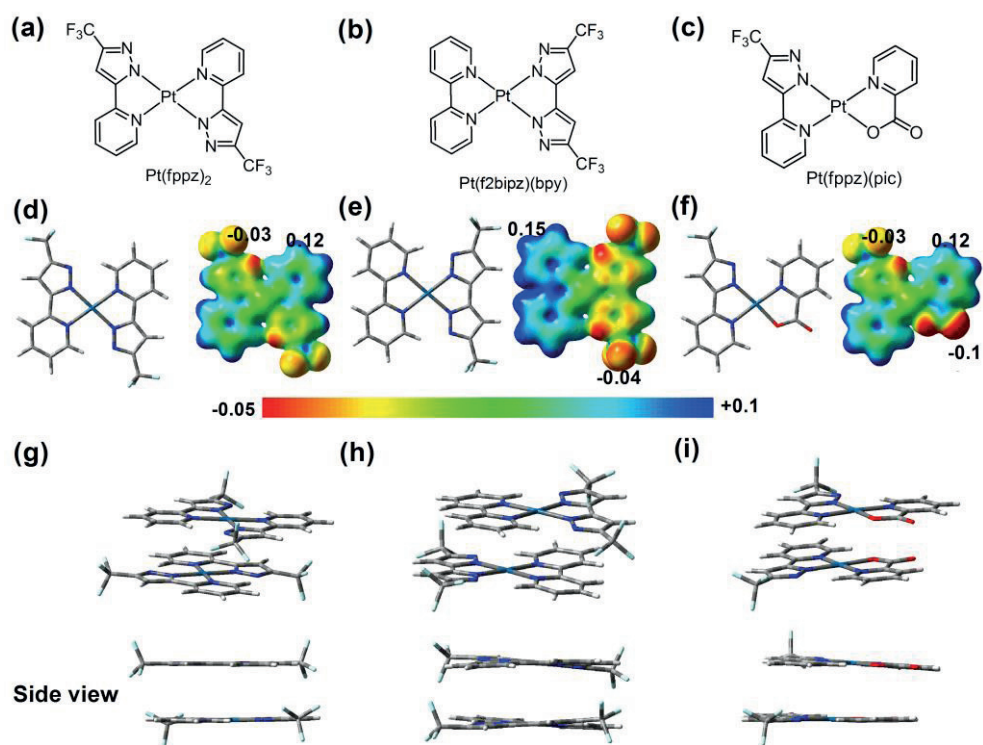


Figure 8.1 Molecular structures of (a) Pt(fppz)₂, (b) Pt(f2bipz)(bpy) and (c) Pt(fppz)(pic). Isosurfaces of the molecular ESP for (d) Pt(fppz)₂, (e) Pt(f2bipz)(bpy), and (f) Pt(fppz)(pic). Optimized dimer geometries of (g) Pt(fppz)₂, (h) Pt(f2bipz)(bpy), and (i) Pt(fppz)(pic).

Pt(f2bipz)(bpy). 90° and 180° rotational alignments were considered as the initial geometries for optimizing the dimer structure of Pt(fppz)(pic) due to the lack of structural data. The optimized geometries of all Pt dimers are shown in Figure 8.1g-i. The Pt(fppz)₂ and Pt(f2bipz)(bpy) dimers are juxtaposed parallel each other. In contrast, the 90°-disposed Pt(fppz)(pic) dimer (Figure 8.1i) is more stable than the 180°-aligned geometry (Figure 8.2) and the molecules are slanted due to the stronger coulomb interaction between overlapping pyridine and oxygen in picolinate in the dimer than the interaction between pyridine and CF₃-substituted pyrazolate. Steric hindrance also plays a major role for the non-parallel alignment in the Pt(fppz)(pic) dimer. The calculated interplanar distances between the dimeric Pt complexes were found to be 3.25 Å for Pt(fppz)₂, 3.18 Å for Pt(f2bipz)(bpy), and 3.25 Å (center of molecule) for Pt(fppz)(pic) and the binding energies of the Pt complex dimers were -31.1 kcal/mol for Pt(fppz)₂, -44.1 kcal/mol for Pt(f2bipz)(bpy), -29.5 kcal/mol for Pt(fppz)(pic), respectively. The strongest binding energy of Pt(f2bipz)(bpy) resulted in the shortest interplanar distance. As results, Pt(f2bipz)(bpy) possesses higher intermolecular binding than Pt(fppz)₂ due to stronger coulomb interaction between ligands, and Pt(fppz)(pic) exhibits non-parallel molecular alignment coming from lower symmetry.

Figure 8.3 shows the GIWAXD and the atomic force microscope (AFM) images of the neat films of Pt(fppz)₂ (Figure 8.3a,b), Pt(f2bipz)(bpy) (Figure 8.3c,d), and Pt(fppz)(pic) (Figure 8.3e,f), respectively, which were vacuum deposited under 5×10^{-7} Torr on Si substrates. The Pt(fppz)₂ and Pt(f2bipz)(bpy) films showed the single-crystal-like GIWAXD images, which are very well indexed as the perfectly

Top view



Side view

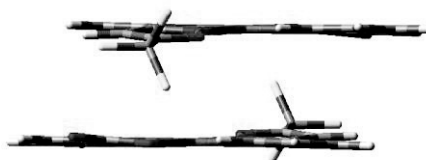


Figure 8.2 Optimized geometry of Pt(fppz)(pic) dimer at 180° rotational geometry. The binding energy of 180° rotational geometry (21.7 kcal/mol) is lower than that of 90° rotational geometry (29.5 kcal/mol).

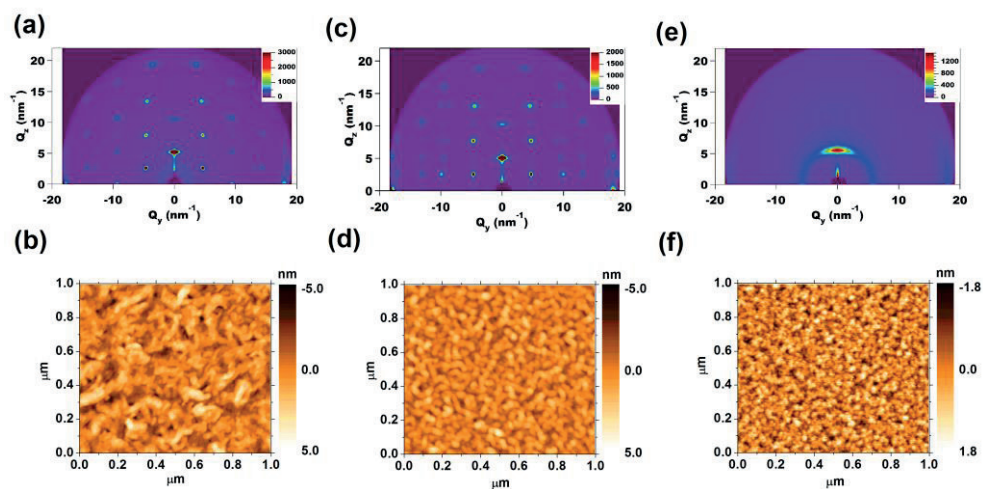


Figure 8.3 GIWAXD images measured at 0.15° incident angle of 30 nm thick film (a) Pt(fppz)₂, (c) Pt(f2bipz)(bpy), (e) Pt(fppz)(pic) on silicon substrate. AFM images of 30 nm thick (b) Pt(fppz)₂, (d) Pt(f2bipz)(bpy), (f) Pt(fppz)(pic).

oriented crystals along the [100] direction. The unit cells of the thin-film crystals are shown in Figure 8.4a,b, which are different from the unit cells of single crystals shown in Figure 8.4c,d, respectively. The lattice parameters and the angles of the crystals of the unit cells are summarized in Table 8.1. The thin-film crystals have the pseudo orthorhombic structures with $\beta = 91^\circ$ for Pt(fppz)₂, 89° for Pt(f2bipz)(bpy) and $\alpha = \gamma = 90^\circ$ whereas the single crystals have the monoclinic structures with $\beta = 99^\circ$ and 93° for Pt(fppz)₂ and Pt(f2bipz)(bpy), respectively. The lattice parameters of the Pt(fppz)₂ crystal in the film are similar with those of the single crystal. However, the lattice parameter *a* of the Pt(f2bipz)(bpy) crystal in the thin film is almost twice of the single crystal because the molecules of upper layer in the unit cell are translated by the half of the lattice parameter *c* along the z-axis from the bottom layer, shown in Figure 8.4b. The x, y, z-projection views of the thin-film unit cell are shown in Figure 8.5. Thus, Pt(fppz)₂ crystals in thin film and single crystal have 4 molecules in monoclinic C-lattice, but Pt(f2bipz)(bpy) crystals in thin film and single crystal have 8 and 4 molecules in monoclinic P-lattice, respectively. The single-crystal-like GIWAXD images were assigned as the polycrystalline structures perfectly oriented along the [100] direction based on the same diffraction images independent of the azimuthal angle as shown in Figure 8.6. In contrast, the Pt(fppz)(pic) film has much less ordered structure, but still showed the preferred orientation with the edge on molecular ordering based on the layer spacing of ≈ 2.1 nm calculated from the *k* value of the strong diffraction peak. The grain sizes of Pt(fppz)₂, Pt(f2bipz)(bpy), and Pt(fppz)(pic) in the 30 nm thick films were 20.1, 21.6, and 12.5 nm along the vertical direction ([100] direction), and 8.9, 14.7, and 3.3 nm

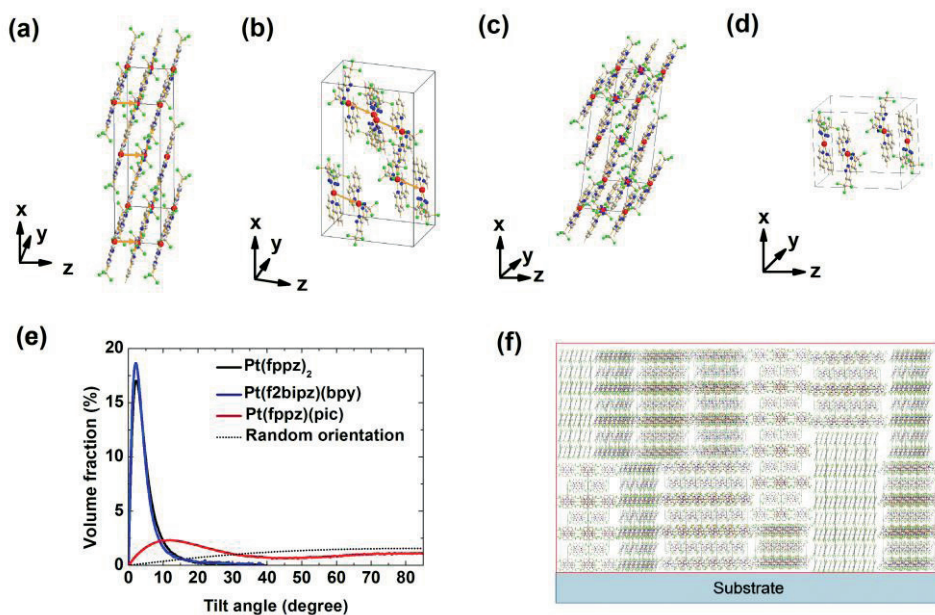


Figure 8.4 Unit cells of a) Pt(fppz)₂ crystal in the film, b) Pt(f2bipz)(bpy) crystal in the film, c) Pt(fppz)₂ single crystal, d) Pt(f2bipz)(bpy) single crystal. Orange arrows in a) and b) indicate the direction of transition dipole moments of MMLCT. e) Angular volume fractions of Pt(fppz)₂, Pt(f2bipz)(bpy), and Pt(fppz)(pic) crystals in the film f) Schematic drawing of Pt(fppz)₂ crystals in thin film.

Table 8.1 Crystal data of single crystal and thin film for Pt(fppz)₂, Pt(f2bipz)(bpy) and Pt(fppz)(pic).

	Pt(fppz) ₂		Pt(f2bipz)(bpy)		Pt(fppz)(pic)	
	Single crystal	Thin film	Single crystal	Thin film	Single crystal	Thin film
a (Å)	19.6	22.3	12.5	22.6	-	20.8
b (Å)	12.6	12.7	12.0	12.0	-	-
c (Å)	7.7	6.9	13.3	13.9	-	6.8
α (°)	90	90	90	90	-	-
β (°)	99	91	93	89	-	-
γ (°)	90	90	90	90	-	-
Vertical grain size (nm, [100] direction)	-	20.1	-	21.6	-	12.5
Horizontal grain size (nm, [010] direction)	-	12.7	-	11.6	-	-
Horizontal grain size (nm, [001] direction)	-	8.9	-	14.7	-	3.3

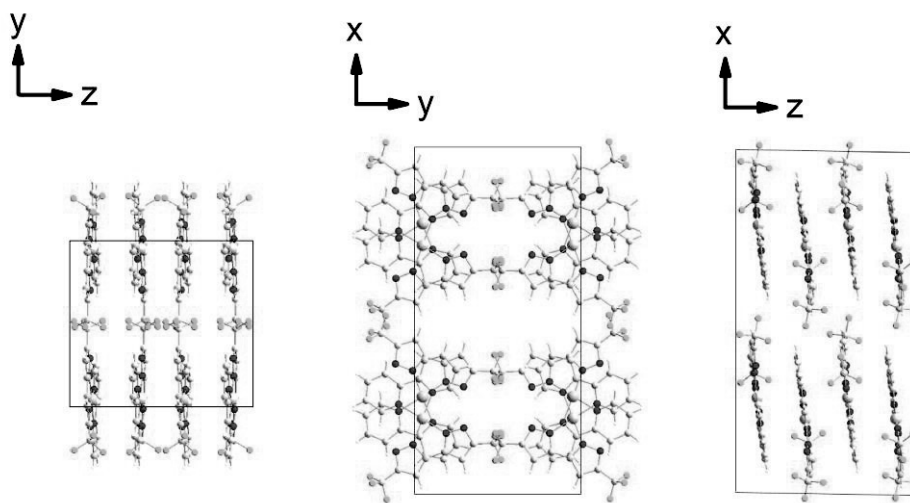


Figure 8.5 Projection view of thin film unit cell of Pt(f2bipz)(bpy). Y and Z axis are parallel to the substrate.

along the [001] direction, and 12.7 nm for Pt(fppz)₂ and 11.6 nm for Pt(f2bipz)(bpy) along the [010] direction, respectively, which were calculated from the full width at half maximum of the XRD peak using the Scherrer's equation (Table 8.1). AFM images of the films show that the Pt(fppz)₂ and Pt(f2bipz)(bpy) crystals have needle and granular shapes, respectively, with larger grains than the circular shape crystals for Pt(fppz)(pic), consistent with the X-ray analysis. The root mean square roughness of the films were 1.17 nm for Pt(fppz)₂, 0.54 nm for Pt(fppz)(pic) and 0.88 nm for Pt(f2bipz)(bpy), respectively. The films are smooth enough to fabricate OLEDs with little leakage current.

Angular volume fraction of platinum crystals was calculated to compare the degree of preferential ordering in each case. The angular volume fractions were obtained from the intensity distribution in the (200) halo in the 2D diffraction images by counting all the crystals having the same angular orientation in the in-plane direction (x-y plane), but different orientations from the surface normal under the assumption of homogeneous film in the in-plane direction. Angular volume fraction of platinum complex is defined as volume fraction of platinum crystal placed between θ and $\theta + \delta\theta$ from surface normal direction. The spherical integration was performed because 2D diffraction image is the cross sectional view of the Ewald sphere of a film as shown in Figure 8.7. Analysis of the angular volume fraction indicated that more than 95% of the crystals in the Pt(fppz)₂ and Pt(f2bipz)(bpy) films have the tilt angle less than 10° from the (100) orientation, respectively (Figure 8.4e). Based on the analysis, the crystal structure of the Pt(fppz)₂ thin film is schematically depicted in Figure 8.4f, displaying the perfectly oriented molecules

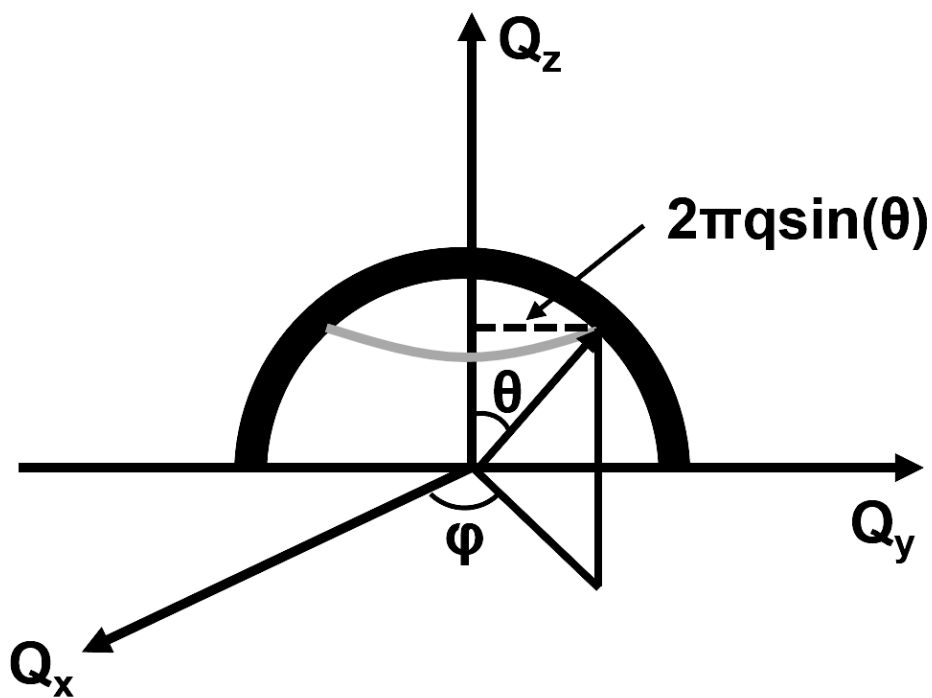


Figure 8.7 Integration geometry of (200) 2D circular peak data in the spherical coordinate.

with the edge-on molecular alignment tilted by 14° from the surface normal direction, but with random orientation in the lateral direction. It is interesting to note that Pt atoms are aligned parallel to the substrate. Similar crystal structure can be drawn for the Pt(f2bipz)(bpy) film. We measured GIWAXD with various substrates to figure out if they are influenced by the underlying layers. The 30 nm thick neat films of Pt complexes were deposited on the piranha-treated Si substrate, OTS-treated Si substrate, Si/1,1-bis(4-p-tolylaminophenyl)cyclohexane (TAPC) (80 nm)/4,4',4''-tri(N-carbazolyl)-triphenylamine (TCTA) (10 nm) substrate with the respective contact angles of 10° , 104° , and 81° determined from water droplet.^{131,132} All the samples exhibited the same crystal pattern but different crystallinity, indicating that crystallinity is influenced by the surface energy of the under layers even though the crystal structures are not affected (Figure 8.8). Especially, the grain sizes in the 30 nm thick Pt(fppz)₂ films on organic layer (Figure 8.8c) are almost same with that on Si substrate (22.3 nm along the vertical direction ([100] direction), and 8.7 nm along the [001] direction, and 12.5 nm along the [010] direction, respectively) but orientation of Pt(fppz)₂ crystals on organic layer exhibited slightly broader distribution against the surface normal direction than that on Si substrate.

PL spectra of the platinum complexes are shown in Figure 8.9a. The PL peaks of 10^{-5} M Pt complexes in THF were 447 nm for Pt(fppz)₂, 403 nm and 423 nm for Pt(f2bipz)(bpy) and 403 nm for Pt(fppz)(pic), respectively. The PL intensities were very low. All Pt complex thin films exhibited intense PL emission with featureless and red-shifted spectra corresponding to the excimer originated from metal-metal-to-ligand charge transfer (MMLCT) caused by Pt–Pt metallophilic ligand

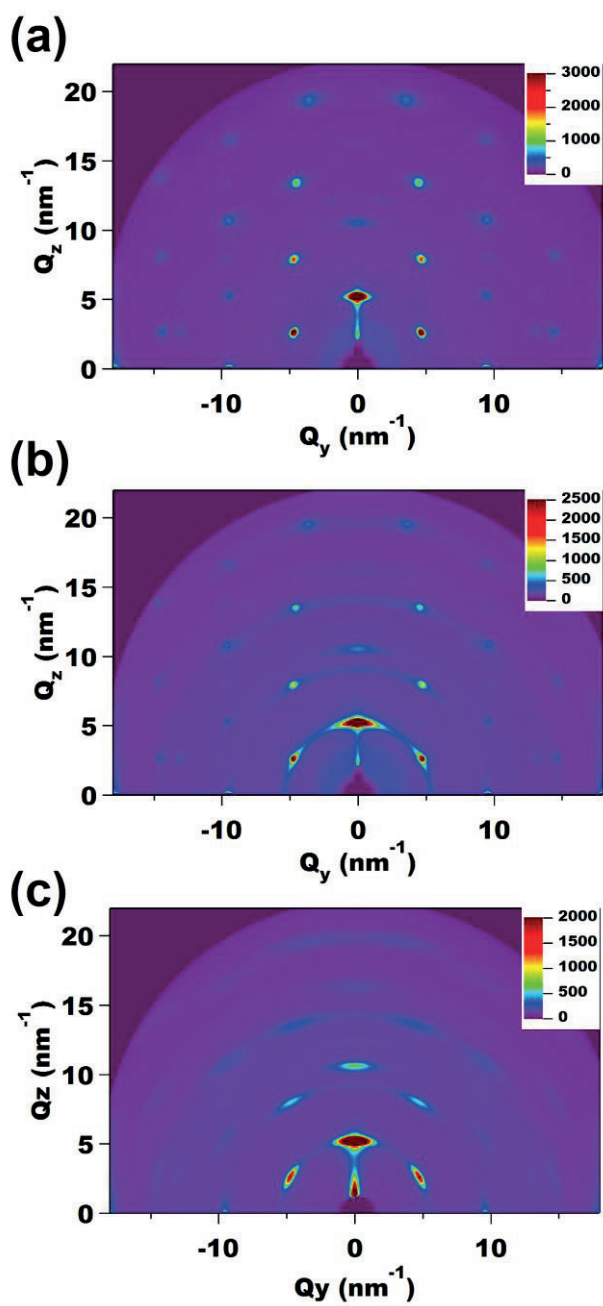


Figure 8.8 GIWAX images of 30 nm thick Pt(fppz)₂ neat film on (a) piranha treated Si substrate, (b) OTS treated Si substrate, (c) hole transporting materials deposited Si substrate.

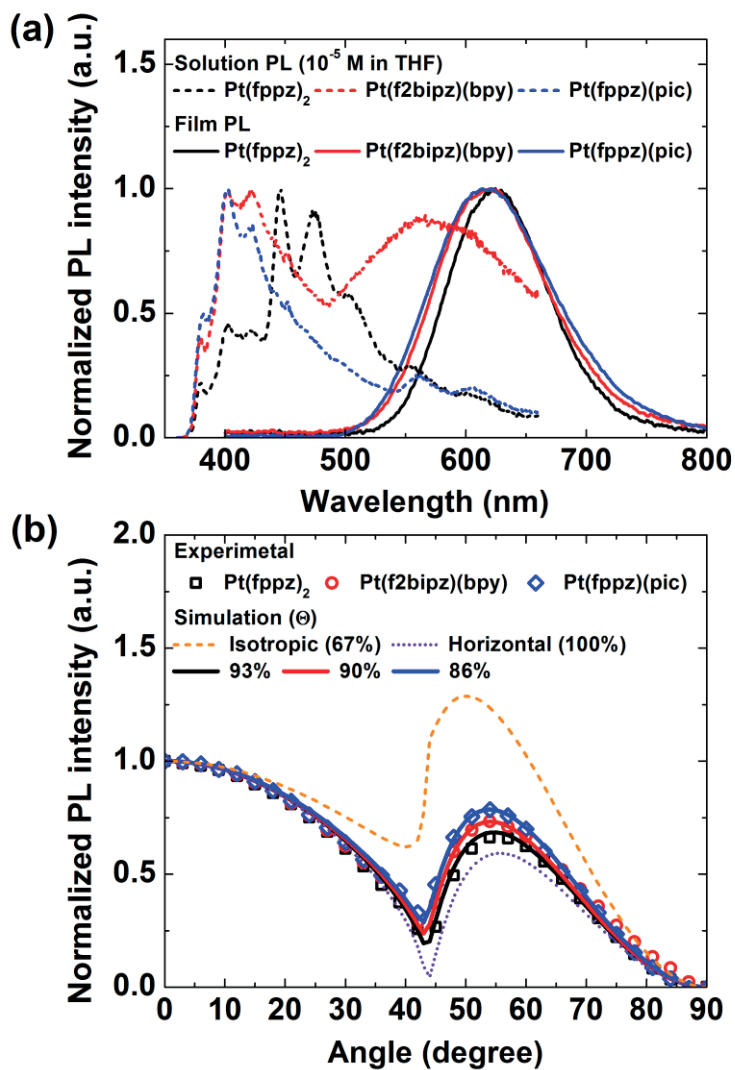


Figure 8.9 (a) PL spectra of 10⁻⁵ M solution and thin film for Pt(fppz)₂, Pt(f2bipz)(bpy), and Pt(fppz)(pic). (b) Angle-dependent PL intensity of p-polarized light at 625 nm from platinum complex 30 nm thick film for Pt(fppz)₂, Pt(f2bipz)(bpy), and Pt(fppz)(pic).

interactions.¹³³⁻¹³⁵ It is interesting to note that the Pt(fppz)₂, Pt(f2bipz)(bpy), and Pt(fppz)(pic) neat films showed essentially identical peak maximum at 625, 622, and 620 nm, respectively. These emission patterns indicate that the Pt–Pt interaction plays a major role in the optical transition versus the Pt–ligand or ligand–ligand interaction. The PLQYs of the neat films were 96% for Pt(fppz)₂, 43% for Pt(f2bipz)(bpy), and 56% for Pt(fppz)(pic). It is not clear at this moment why different complexes result in so different PLQYs, which requires further study. Transient PLs of the Pt complex films are shown in Figure 8.10. The lifetimes of MMLCT were 382 ns for Pt(fppz)₂, 479 ns for Pt(f2bipz)(bpy), and 489 ns for Pt(fppz)(pic), respectively. The emitting dipole orientations of these thin films were analyzed from the angle-dependent PL intensities using *p*-polarized light at 625 nm shown in Figure 8.9b.^{7,17} Birefringence of the films was considered in the analysis.¹⁰⁰ The Θ 's of the emitting dipoles were 93%, 90%, and 86% for Pt(fppz)₂, Pt(f2bipz)(bpy), and Pt(fppz)(pic), respectively. Analysis of angle-dependent PL intensities at various wavelengths is shown in Figure 8.11. Moreover, the Θ of Pt(fppz)₂ film deposited on hole-transporting layer (Fused silica/TCTA 5 nm/Pt(fppz)₂ 30 nm) is almost the same as that of the film deposited on fused silica substrate (Figure 8.12). Apparently the emitting dipoles are aligned along the horizontal direction in the films. MMLCT is almost orthogonal to metal-ligand charge transfer (MLCT) in the films because the experimentally observed orientation of the emitting dipoles (MMLCT) is along the horizontal direction while the molecular plane is almost vertical within which the MLCT is located. Naturally, the preferred orientation of the Pt(fppz)₂ crystals resulted in unprecedented high Θ value

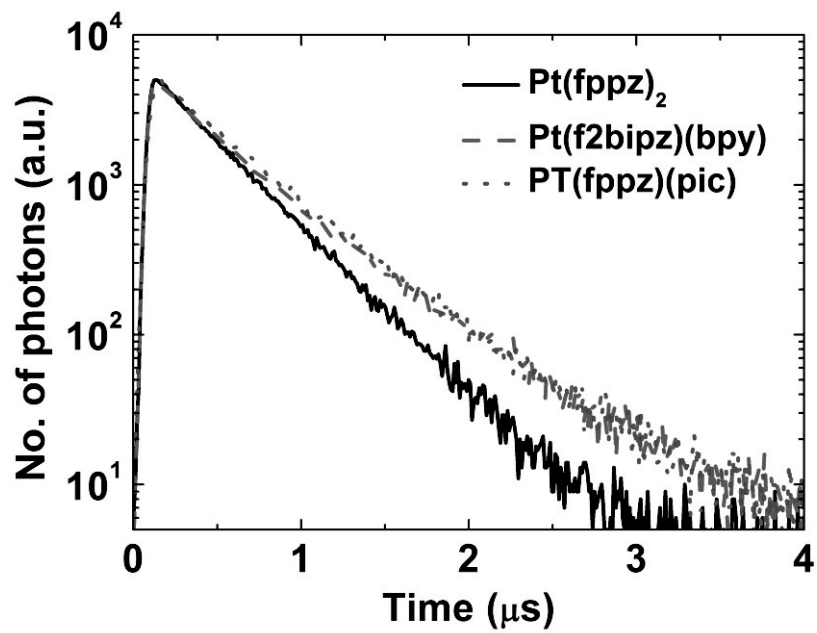


Figure 8.10 Transient PLs of 30 nm thick films for $\text{Pt}(\text{fppz})_2$, $\text{Pt}(\text{f2bipz})(\text{bpy})$, and $\text{Pt}(\text{fppz})(\text{pic})$.

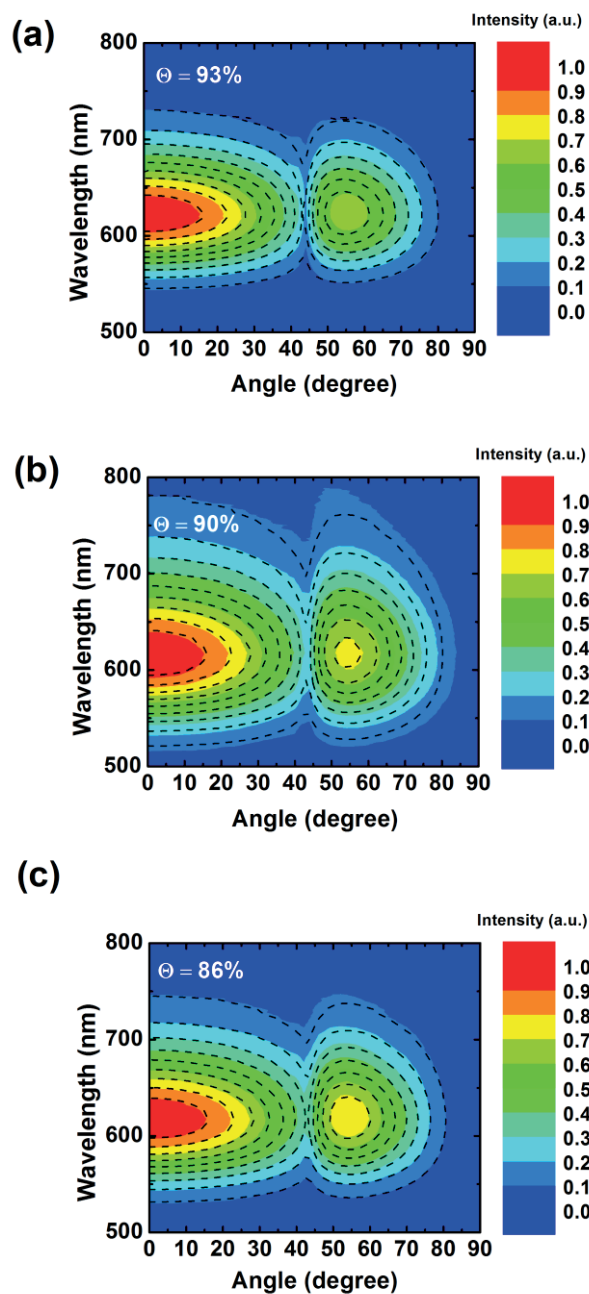


Figure 8.11 Angle-dependent PL spectra of p-polarized light from platinum complex 30 nm thick film for (a) Pt(fppz)₂, (b) Pt(f2bipz)(bpy) and (c) Pt(fppz)(pic). Dashed lines represent theoretical fits to the experimental data.

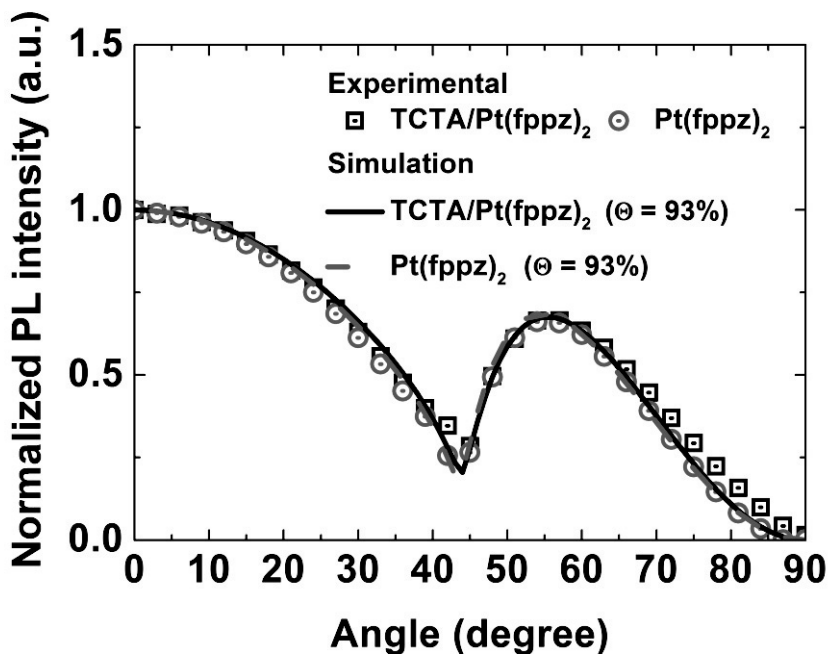


Figure 8.12 Angle-dependent PL intensity of p-polarized light at 625 nm from 30 nm thick Pt(fppz)₂ deposited on hole transporting material (fused silica/TCTA 5 nm/ Pt(fppz)₂ 30nm) and fused silica (fused silica/Pt(fppz)₂ 30nm).

of 93%. Pt(fppz)(pic) exhibited lower Θ than Pt(fppz)₂ and Pt(f2bipz)(bpy) because the Pt(fppz)(pic) crystal is less oriented than others as shown in Figure 8.4e. Structural analysis of the thin-film crystals showed that the Pt–Pt bonds in the Pt(fppz)₂ crystal aligned entirely parallel to the substrate (Figure 8.4), but those of the Pt(f2bipz)(bpy) molecules are tilted by 22.6° from the substrate (Figure 8.5). The direction of Pt–Pt bonds in crystal is shown by orange arrow in Figure 8.4a,b. Thus, the Θ of Pt(f2bipz)(bpy) was lower than that of Pt(fppz)₂ even though Pt(f2bipz)(bpy) have higher crystallinity. Therefore, not only the orientation and crystallinity but also the molecular arrangement in crystals is a crucial factor for having preferred orientation of emitting dipoles.

OLEDs were fabricated using these Pt complexes as an emitting layer. The structure of the OLEDs are: ITO (100 nm)/TAPC (80 nm)/TCTA (10 nm)/Pt(fppz)₂ or Pt(fppz)(pic) (30 nm)/1,3-bis(3,5-di(pyridin-3-yl)phenyl)benzene (BMPYPB) (15 nm)/BMPYPB: 1 wt% Rb₂CO₃ (40 nm)/Al (100 nm), or ITO (100 nm)/1,3-Bis(N-carbazolyl)benzene (mCP): 5 wt% ReO₃ (60 nm)/mCP (10 nm)/Pt(f2bipz)(bpy) (30 nm)/bis-4,6-(3,5-di-3-pyridylphenyl)-2-methylpyrimidine (B3PYMPM) (15 nm)/B3PYMPM: 1 wt% Rb₂CO₃ (40 nm)/Al (100 nm). We applied mCP as the hole-transporting layer and B3PYMPM as the electron-transporting layer in the Pt(f2bipz)(bpy) device to achieve balanced carrier transport because the highest occupied molecular orbital (HOMO) and lowest unoccupied molecular orbital (LUMO) energy levels of Pt(f2bipz)(bpy) are lower than those of Pt(fppz)₂ and Pt(fppz)(pic). The HOMO and LUMO levels of Pt complexes are summarized in Table 8.2. Their current density–voltage–luminance (*J-V-L*) characteristics are sho-

Table 8.2 Energy levels of HOMO and LUMO for Pt(fppz)₂, Pt(f2bipz)(bpy) and Pt(fppz)(pic).

	HOMO (eV)	LUMO (eV)
Pt(fppz) ₂	5.67	2.65
Pt(f2bipz)(bpy)	6.14	3.16
Pt(fppz)(pic)	5.72	2.73

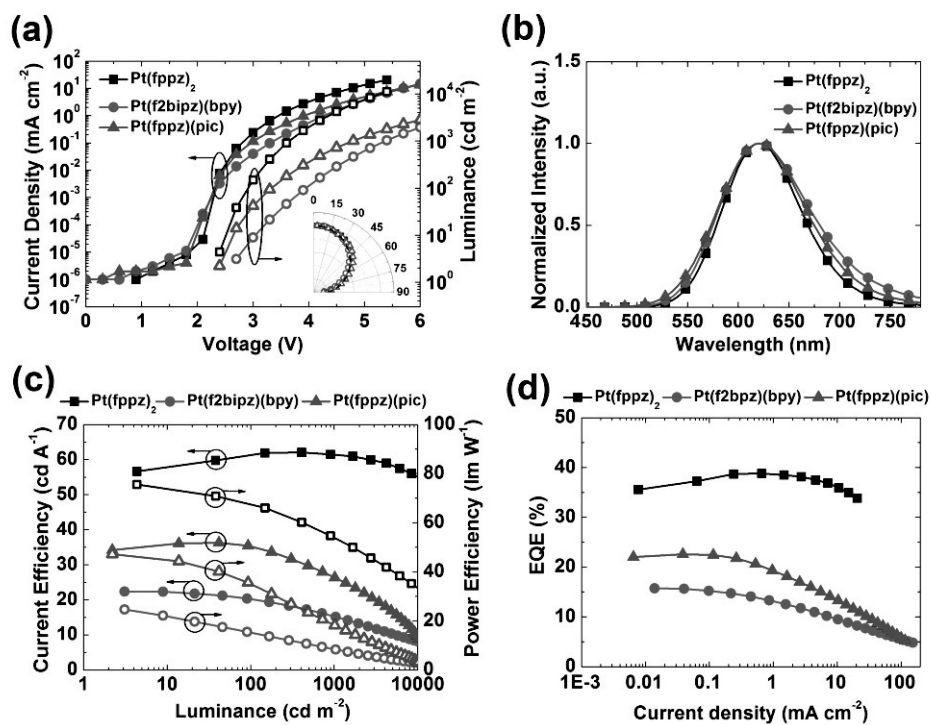


Figure 8.13 (a) J - V - L characteristics. (Inset: the angular distributions of the EL intensities of the OLEDs. The dashed line in the inset shows the Lambertian distribution.) (b) EL spectra of the OLEDs. (c) Current efficiency and power efficiency as a function of the luminance. (d) EQEs as a function of the current density.

wn in Figure 8.13a. The turn on voltages were recorded to be 2.4 V for Pt(fppz)₂ and Pt(fppz)(pic), and 2.7 V for Pt(f2bipz)(bpy). OLEDs composed of crystal emitting layer exhibit low leakage currents and smooth *J-V-L* curves, results from smooth surface of crystal emitting layer. The EL spectra of the OLEDs matched very well with the respective PL spectra (Figure 8.9a). The EQEs and power efficiencies of the devices calibrated using the profiles of the angle-dependent emitted number of photons (inset of Figure 8.13a) are shown in Figure 8.13c,d. The maximum EQEs were 38.8%, 15.7%, and 22.6% and the maximum current efficiencies were 62, 22.4, and 36.3 cd/A and the power efficiencies at 1000 cd/m² were 53.8, 8.4, and 18.2 lm/W for the devices of Pt(fppz)₂, Pt(f2bipz)(bpy), and Pt(fppz)(pic), respectively. This EQE of 38.8% is the highest efficiency ever reported to date.^{33,130} The calculated maximum achievable EQEs of the devices based on the measured Θ 's and PLQY's under the assumption of no electrical loss were 40.5%, 17.9%, and 22.8% for Pt(fppz)₂, Pt(f2bipz)(bpy), and Pt(fppz)(pic), respectively. Refractive indices of platinum complex thin film used in optical simulation are shown in Figure 8.15. These values match well with all of the recorded EQEs, indicating that all devices had lowered leakage current, among which the Pt(fppz)₂ devices exhibited the highest measured EQE as well as the highest calculated EQE. OLED light emission is uniform for eyes even though emitting layer is polycrystalline because the grain size of crystal is in nanometer scale (Figure 8.14).



Figure 8.14 A light emission image of a Pt(fppz)₂ based OLED at 0.75 mA/cm².

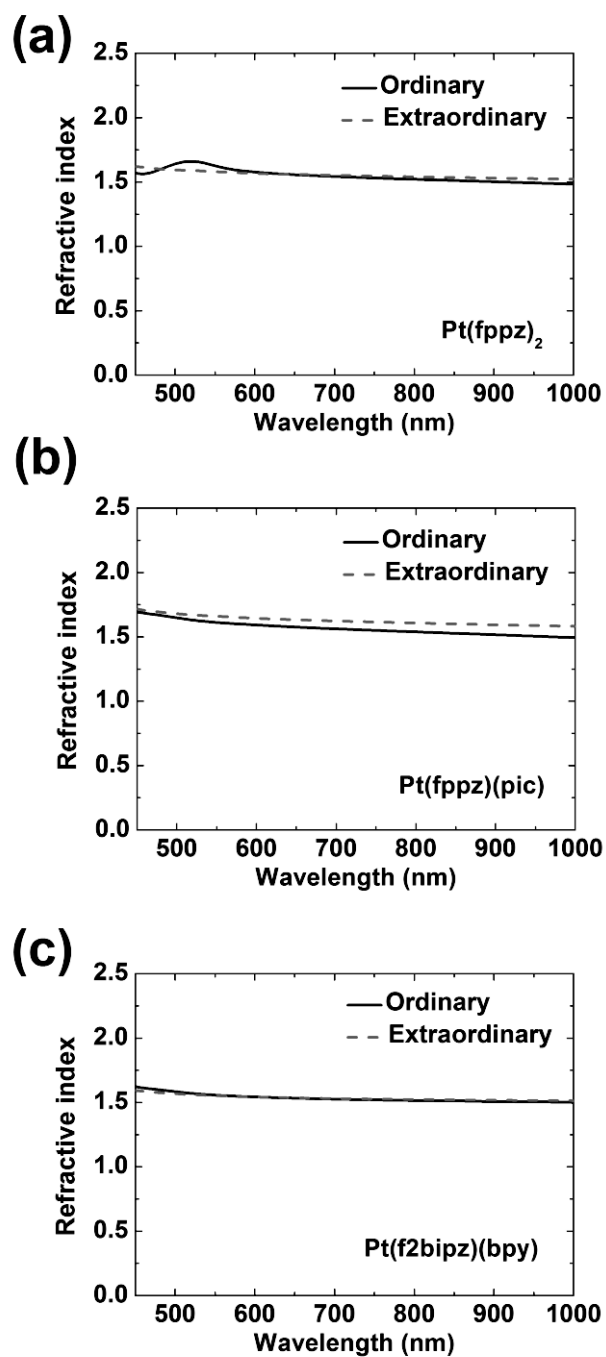


Figure 8.15 Refractive indices of 30 nm thick (a) Pt(fppz)₂, (b) Pt(f2bipz)(bpy) and (c) Pt(fppz)(pic) films.

8.4 Conclusion

In summary, we realized OLED with an extremely high maximum EQE of 38.8% using the Pt-based thin-film emitting layer with PLQY of 96% and Θ of 93%, versus the theoretical EQE limit of 45% for the highest possible PLQY and Θ of 100%. The emitting dipole orientation of the crystal emitting layers was largely affected not only by the crystallinity of the emitting layer but also by the molecular arrangement in the crystal, which are influenced by both the symmetry and position of the CF₃-substituted pyrazolate units in Pt complexes. These results demonstrate the potential that thin-film crystal based OLEDs can outperform amorphous thin-film-based OLEDs.

Chapter 9. Summary and Outlook

Organic light-emitting diodes (OLEDs) have become increasingly important as next-generation display because they have a high color gamut and are thin, flexible and transparent. Having recognized the market potential, Samsung and LG have worked on the development of OLED displays, and have recently released a high resolution and flexible display for mobile devices as well as a large area, curved display for televisions. Lighting is one of the greatest strengths of OLEDs, as compared to LEDs. The surface light source of OLEDs allow them to be thin, flexible, and transparent, permitting more freedom and creativity in product design. Several companies have released OLED lighting products into the market. Automobile companies have applied the technology to active backlighting. Light emission efficiency is one of the most important characteristics of OLED devices, as it is directly related to power consumption and influences the lifetime of the device. However, OLEDs still have lower power efficiency than LEDs, and greater efficiency is required for these devices to gain widespread popularity in lighting and displays.

This thesis presents exciplex dynamics and emitting dipole orientation of emitters for highly efficient OLEDs. Based on these observations, record-breaking efficiencies of fluorescent and phosphorescent OLEDs are demonstrated.

In chapters 2 and 3, exciplex dynamics influencing triplet harvest were analyzed quantitatively. Our results show that not only efficient reverse intersystem crossing (RISC) but also low nonradiative loss in both singlet and triplet exciplexes

is required for efficient exciplex-based OLEDs. Even though a high efficiency, approaching the 25.2% external quantum efficiency (EQE), was obtained at a low temperature, these results clearly demonstrate that OLEDs with 100% internal quantum efficiency (IQE) harvesting all triplets are possible using an exciplex, if the exciplex system is designed to have almost zero nonradiative triplet exciplex processes through smart molecular design. Furthermore, an exciplex was used as a host for a conventional fluorescent dopant (DCJTB) to improve the fraction of radiative excitons over 25%. Our analysis indicated that an extra 10.1% of singlet excitons were formed by the RISC of the triplet exciplex to the singlet exciplex, followed by the energy transfer to DCJTB. As a result, a red fluorescent OLED with an unprecedented high EQE of 10.6% was demonstrated using DCJTB as an emitter doped in an exciplex forming host.

In chapters 4-7, the emitting dipole orientation of Ir complexes and their nature are described. We investigated the relationship between molecular structures and emitting dipole orientation of Ir complexes, and the origin of the preferred orientation of emitting dipoles for heteroleptic Ir complexes. Unprecedented, high-efficiency phosphorescent OLEDs were demonstrated using horizontally-oriented emitters. This study shows that intermolecular interactions are important in the orientation of the emitting dipoles, and high values of the ratio of horizontal emitting dipoles (Θ) are expected for HICs if the emitting dipole vectors are perpendicular to the C_2 axes in the molecules, and the doubly degenerated TDMs are parallel to the substrate. Based on these observations, new heteroleptic Ir complexes with horizontal emitting dipoles were designed and synthesized. These complexes

showed an improved Θ s from 74% to 86.5% and demonstrated an unprecedented, high EQE of 38.1% for Ir based phosphorescent OLEDs.

Emitter molecules in the emitting layer can have a preferred molecular orientation with some distributions; however, the molecular orientation is not perfect due to the amorphous nature of typical emitting layers. Thus, it will be difficult to obtain an even higher Θ using Ir complexes. In this regard, organic crystals would be better emitters because of their orientational and positional ordering. In chapter 8, perfectly oriented Pt based thin film emitting layers were designed, with a Θ of 93% and a photoluminescence quantum yield of 96%. A crystal OLED with an unprecedented, high EQE of 38.8% was demonstrated using a crystal emitting layer. This study shows the structural property relationships between molecular structures, crystal structures and the emitting dipole orientation of Pt complexes. These results demonstrate the potential for thin film crystal-based OLEDs to outperform amorphous thin-film-based OLEDs.

The reported origin of the preferred orientation dipoles of the phosphorescent dyes, and the high efficiency of 38.8%, change the conceptual understanding of the isotropic orientation of phosphorescent dyes and break the efficiency limit set in OLED studies to date. A method for improving Θ using a crystal-emitting layer and the design of Ir complexes with high Θ are demonstrated here, which provide new pathways to the development of high performance OLEDs that are practically applicable in OLED industries. Hence, we believe that the present work will be of interest to engineers and scientists in the OLED research and display industries, and

will promote the goal of increasing the EQE further.

Bibliography

- [1] M. Pope, H. P. Kallmann, P. Magnante, *J. Chem. Phys.* **1963**, 38, 2042.
- [2] C. W. Tang, S. A. VanSlyke, *Appl. Phys. Lett.* **1987**, 51, 913.
- [3] C. W. Tang, S. A. VanSlyke, C. H. Chen, *J. Appl. Phys.* **1989**, 65, 3610.
- [4] M. A. Baldo, D. F. O'Brien, Y. You, A. Shoustikov, S. Sibley, M. E. Thompson, S. R. Forrest, *Nature* **1998**, 395, 151.
- [5] H. Uoyama, K. Goushi, K. Shizu, H. Nomura, C. Adachi, *Nature* **2012**, 492, 234.
- [6] K. Goushi, K. Yoshida, K. Sato, C. Adachi, *Nat. photon.* **2012**, 6, 253.
- [7] S.-Y. Kim, W.-I. Jeong, C. Mayr, Y.-S. Park, K.-H. Kim, J.-H. Lee, C.-K. Moon, W. Brütting, J.-J. Kim, *Adv. Funct. Mater.* **2013**, 23, 3896.
- [8] C. K. Chiang, C. R. Fincher, Jr., Y. W. Park, A. J. Heeger, H. Shirakawa, E. J. Louis, S. C. Gau, A. G. MacDiarmid, *Phys. Rev. Lett.* **1977**, 39, 1098.
- [9] J.-H. Lee, J.-J. Kim, *Phys. Status Solidi A* **2012**, 209, 1399.
- [10] I. D. Parker, *J. Appl. Phys.* **1993**, 75, 1656.
- [11] S.-Y. Kim, J.-J. Kim, *Org. Electron.* **2010**, 11, 1010.
- [12] H. Becker, S. E. Burns, R. H. Friend, *Phys. Rev. B.* **1997**, 56, 1893.
- [13] J.-S. Kim, P. K. H. Ho, N. C. Greenham, R. H. Friend, *J. Appl. Phys.* **2000**, 88, 1073.
- [14] P. K. H. Ho, J.-S. Kim, J. H. Burroughes, H. Becker, S. F. Y. Li, T. M. Brown, F. Cacialli, R. H. Friend, *Nature* **2000**, 404, 481.
- [15] H.-W. Lin, C.-L. Lin, H.-H. Chang, Y.-T. Lin, C.-C. Wu, Y.-M. Chen, R.-T. Chen, Y.-Y. Chien, K.-T. Wong, *J. Appl. Phys.* **2004**, 95, 881.

- [16] D. Yokoyama, *J. Mater. Chem.* **2011**, 21, 19187.
- [17] J. Frischeisen, D. Yokoyama, C. Adachi, W. Brütting, *Appl. Phys. Lett.* **2010**, 96, 073302.
- [18] F. Michael, J. Frischeisen, D. S. Setz, D. Michaelis, B. C. Krummacher, T. D. Schmidt, W. Brütting, N. Danz, *Org. Electron.* **2011**, 12, 1663.
- [19] P. Liehm, C. Murawski, M. Furno, B. Lüsse, K. Leo, M. C. Gather, *Appl. Phys. Lett.* **2012**, 101, 253304.
- [20] L. Penninck, F. Steinbacher, R. Krausec, K. Neyts, *Org. Electron.* **2012**, 13, 3079.
- [21] J. A. Woollam, B. Johs, C. M. Herzinger, J. Hilfiker, R. Synowicki, C. L. Bungay, *Proc. SPIE* **1999**, CR72, 3.
- [22] D. Yokoyama, A. Sakaguchi, M. Suzuki, C. Adachi, *Org. Electron.* **2009**, 10, 127.
- [23] H. Shin, J.-H. Lee, C.-K. Moon, J.-S. Huh, B. Sim, J.-J. Kim, *Adv. Mater.* **2016**, DOI: 10.1002/adma.201506065
- [24] R. R. Chance, A. Prock, R. Silbey, *Advances in Chemical Physics*, Wiley, New York, USA **1978**, 37.
- [25] S. H. Garrett, J. A. E. Wasey, W.L. Barnes, *J. Mod. Opt.* **2004**, 51, 2287.
- [26] M. Kreiter, M. Prummer, B. Hecht, U.P. Wild, *J. Chem. Phys.* **2002**, 117, 9430.
- [27] N. J. Turro, *Modern Molecular Photochemistry*, University Science Books, Mill Vally, U.S.A, **1991**.
- [28] H. Beens, H. Knibbe, A. J. Weller, *Chem. Phys.* **1967**, 47, 1182

- [29] W. Baumann, H. Bischof, J. C. Frohling, *J. Lumin.* **1981**, 24/25, 555.
- [30] Y.-S. Park, S. Lee, K.-H. Kim, S.-Y. Kim, J.-H. Lee, J.-J. Kim, *Adv. Funct. Mater.* **2013**, 23, 4914.
- [31] S. Lee, K.-H. Kim, D. Limbach, Y.-S. Park, J.-J. Kim, *Adv. Funct. Mater.* **2013**, 23, 4105.
- [32] K.-H. Kim, C.-K. Moon, J.-H. Lee, S.-Y. Kim, J.-J. Kim, *Adv. Mater.* **2014**, 26, 3844.
- [33] K.-H. Kim, S. Lee, C.-K. Moon, S.-Y. Kim, Y.-S. Park, J.-H. Lee, J. W. Lee, J. Huh, Y. You, J.-J. Kim, *Nat. Commun.* **2014**, 5, 4769.
- [34] H. Shin, S. Lee, K.-H. Kim, C.-K. Moon, S.-J. Yoo, J.-H. Lee, J.-J. Kim, *Adv. Mater.* **2014**, 26, 4730.
- [35] J.-H. Lee, S. Lee, S.-J. Yoo, K.-H. Kim, J.-J. Kim, *Adv. Funct. Mater.* **2014**, 24, 4681.
- [36] Y.-S. Park, K.-H. Kim, J.-J. Kim, *Appl. Phys. Lett.* **2013**, 102, 153306.
- [37] K. Goushi, C. Adachi, *Appl. Phys. Lett.* **2012**, 101, 023306.
- [38] W.-Y. Hung, G.-C. Fang, Y.-C. Chang, T.-Y. Kuo, P.-T. Chou, S.-W. Lin, K.-T. Wong, *ACS Appl. Mater. Interfaces* **2013**, 5, 6826.
- [39] J. Li, H. Nomura, H. Miyazaki, C. Adachi, *Chem. Commun.* **2014**, 50, 6174.
- [40] W.-Y. Hung, G.-C. Fang, S.-W. Lin, S.-H. Cheng, K.-T. Wong, T.-Y. Kuo, P.-T. Chou, *Sci. Rep.* 2014, 4, 5161.
- [41] T. Zhang, B. Chu, W. Li, Z. Su, Q. M. Peng, B. Zhao, Y. Luo, F. Jin, X. Yan, Y. Gao, H. Wu, F. Zhang, D. Fan, J. Wang, *ACS Appl. Mater. Interfaces* **2014**, 6, 11907.

- [42] X.-K. Liu, Z. Chen, C.-J. Zheng, C.-L. Liu, C.-S. Lee, F. Li, X.-M. Ou, X.-H. Zhang, *Adv. Mater.* **2015**, *27*, 2378.
- [43] T. Zhang, B. Zhao, B. Chu, W. Li, Z. Su, X. Yan, C. Liu, H. Wu, Y. Gao, F. Jin, F. Hou, *Sci. Rep.* **2015**, *5*, 10234.
- [44] Q. Zhang, J. Li, K. Shizu, S. Huang, S. Hirata, H. Miyazaki, C. Adachi, *J. Am. Chem. Soc.* **2012**, *134*, 14706.
- [45] G. Mehes, H. Nomura, Q. Zhang, T. Nakagawa, C. Adachi, *Angew. Chem.* **2012**, *51*, 11311.
- [46] J. Li, T. Nakagawa, J. Macdonald, Q. Zhang, H. Nomura, H. Miyazaki, C. Adachi, *Adv. Mater.* **2013**, *25*, 3319.
- [47] F. B. Dias, K. N. Bourdakos, V. Jankus, K. C. Moss, K. T. Kamtekar, V. Bhalla, J. Santos, M. R. Bryce, A. P. Monkman, *Adv. Mater.* **2013**, *25*, 3707.
- [48] Q. Zhang, B. Li, S. Huang, H. Nomura, H. Tanaka, C. Adachi, *Nat. Photon.* **2014**, *8*, 326.
- [49] Y. J. Cho, K. S. Yook, J. Y. Lee, *Adv. Mater.* **2014**, *26*, 4050.
- [50] J. W. Sun, J.-H. Lee, C.-K Moon, K.-H. Kim, H. Shin, J.-J. Kim, *Adv. Mater.* **2014**, *26*, 5684.
- [51] V. Jankus, P. Data, D. Graves, C. McGuinness, J. Santos, M. R. Bryce, F. B. Dias, A. P. Monkman, *Adv. Funct. Mater.* **2013**, *24*, 6178.
- [52] D. Zhang, L. Duan, Y. Li, D. Zhang, Y. Qiu, *J. Mater. Chem. C* **2014**, *2*, 8191.
- [53] M. Kim, S. K. Jeon, S.-H. Hwang, J. Y. Lee, *Adv. Mater.* **2015**, *27*, 2515
- [54] D. R. Lee, B. S. Kim, C. W. Lee, Y. Im, K. S. Yook, S.-H. Hwang, J. Y. Lee,

ACS Appl. Mater. Interfaces **2015**, 7, 9625.

[55] K.-H. Kim, C.-K. Moon, J. W. Sun, B. Sim, J.-J. Kim, *Adv. Optical Mater.* **2015**, 3, 846.

[56] X.-K. Liu, Z. Chen, C.-J. Zheng, M. Chen, W. Liu, X.-H. Zhang, C.-S. Lee, *Adv. Mater.* **2015**, 27, 2025.

[57] B. Zhao, T. Zhang, B. Chu, W. Li, Z. Su, H. Wu, X. Yan, F. Jin, Y. Gao, C. Liu, *Sci. Rep.* **2015**, 5, 10697.

[58] H. Sasabe, D. Tanaka, D. Yokoyama, T. Chiba, Y.-J. Pu, K. Nakayama, M. Yokoyama, J. Kido, *Adv. Funct. Mater.* **2011**, 21, 336.

[59] J. A. E. Wasey, W. L. Barnes, *J. Mod. Optic* **2000**, 47, 725.

[60] D. Y. Kondakov, *J. Appl. Phys.* **2007**, 102, 114504.

[61] D. Y. Kondakov, T. D. Pawlik, T. K. Hatwar, J. P. Spindler, *J. Appl. Phys.* **2009**, 106, 124510.

[62] D. Zhang, L. Duan, C. Li, Y. Li, H. Li, D. Zhang, Y. Qiu, *Adv. Mater.* **2014**, 26, 5050.

[63] H. Nakanotani, T. Higuchi, T. Furukawa, K. Masui, K. Morimoto, M. Numata, H. Tanaka, Y. Sagara, T. Yasuda, C. Adachi, *Nat. Commun.* **2014**, 5, 4016.

[64] M. J. Frisch, G. W. Trucks, H. B. Schlegel, G. E. Scuseria, M. A. Robb, J. R. Cheeseman, G. Scalmani, V. Barone, B. Mennucci, G. A. Petersson, H. Nakatsuji, M. Caricato, X. Li, H. P. Hratchian, A. F. Izmaylov, J. Bloino, G. Zheng, J. L. Sonnenberg, M. Hada, M. Ehara, K. Toyota, R. Fukuda, J. Hasegawa, M. Ishida, T. Nakajima, Y. Honda, O. Kitao, H. Nakai, T. Vreven, J. A.

- Montgomery Jr., J. E. Peralta, F. Ogliaro, M. Bearpark, J. J. Heyd, E. Brothers ,
K. N. Kudin, V. N. Staroverov, R. Kobayashi, J. Normand, K. Raghavachari, A.
Rendell, J. C. Burant, S. S. Iyengar, J. Tomasi, M. Cossi, N. Rega, J. M. Millam,
M. Klene, J. E. Knox, J. B. Cross, V. Bakken, C. Adamo, J. Jaramillo, R.
Gomperts, R. E. Stratmann, O. Yazyev, A. J. Austin, R. Cammi, C. Pomelli, J.
W. Ochterski, R. L. Martin, K. Morokuma, V. G. Zakrzewski, G. A. Voth, P.
Salvador, J. J. Dannenberg, S. Dapprich, A. D. Daniels, O. Farkas, J. B. Foresman,
J. V. Ortiz, J. Cioslowski, D. J. Fox, Gaussian, Inc ., Wallingford CT, **2009**.
- [65] J. Chen, D. Ma, *J. Lumin.* **2007**, 122–123, 636.
- [66] V. V. Jarikov, K. P. Klubek, L.-S. Liao, C. T. Brown, *Appl. Phys. Lett.* **2008**,
104, 074914.
- [67] Y. J. Chang, T. J. Chow, *J. Mater. Chem.* **2011**, 21, 3091.
- [68] V. V. Jarikov, J. R. Vargas, D. Y. Kondakov, R. H. Young, K. P. Klubek,
L.-S. Liao, C.-T. Brown, *SID Symp. Dig. Tech. Pap.* **2012**, 38, 1188.
- [69] D. Z. Garbuzov, V. Bulović, P. E. Burrows, S. R. Forrest, *Chem. Phys. Lett.*
1996, 249, 433.
- [70] T. Förster, *Discuss. Faraday Soc.* **1959**, 27, 7.
- [71] C. H. Chen, C. W. Tang, J. Shi, K. P. Klubek, *Macromol. Symp.* **1997**, 125,
49.
- [72] P. Chen, Z. Xiong, Q. Peng, J. Bai, S. Zhang, F. Li, *Adv. Opt. Mater.* **2014**,
2, 142.
- [73] S. Lamansky, P. Djurovich, D. Murphy, F. Abdel-Razzaq, H.-E. Lee, C.
Adachi, P. E. Burrows, S. R. Forrest, M. E. Thompson, *J. Am. Chem. Soc.* **2001**,

123, 4304.

[74] Y. Kawamura, J. Brooks, J. J. Brown, H. Sasabe, C. Adachi, *Phys. Rev. L.* **2006**, 96, 017404.

[75] D. Tanaka, H. Sasabe, Y.-J. Li, S.-J. Su, T. Takeda, J. Kido, *Jpn. J. Appl. Phys.* **2007**, 46, L10.

[76] M. G. Helander, Z. B. Wang, J. Qiu, M. T. Greiner, D. P. Puzzo, Z. W. Liu, Z. H. Lu, *Science* **2011**, 332, 9.

[77] C. W. Lee, J. Y. Lee, *Adv. Mater.* **2013**, 25, 5450.

[78] K. Saito, N. Matsusue, H. Kanno, Y. Hamada, H. Takahashi, T. Matsumura, *Jpn J. Appl. Phys.* **2004**, 43, 2733.

[79] D. H. Kim, N. S. Cho, H.-Y. Oh, J. W. Yang, W. S. Jeon, J. S. Park, M. C. Suh, J. H. Kwon, *Adv. Mater.* **2011**, 23, 2721.

[80] J.-P. Duan, P.-P. Sun, C.-H. Cheng, *Adv. Mater.* **2003**, 15, 224.

[81] J. A. E. Wasey, A. Safnov, I. D. W. Samuel, W. L. Barnes, *Opt. Comm.* **2000**, 183, 109.

[82] Palik, E. D. & Ghosh, G. Handbook of optical constants of solids (Academic Press, 1998).

[83] R. A. Synowicki, *Thin Solid Films* **1998**, 313, 394.

[84] A. D. Becke, *J. Chem. Phys.* **1988**, 88, 2547.

[85] A. D. Becke, *J. Chem. Phys.* **1993**, 98, 5648.

[86] A. D. Becke, *Phys. Rev. A* **1988**, 38, 3098.

[87] DALTON, a molecular electronic structure program, Release Dalton 2011, <http://daltonprogram.org/> (**2011**).

- [88] U. C. Singh, P. A. Kollman, *J. Comput. Chem.* **1984**, 5, 129.
- [89] J. P. Perfew, K. Burke, M. Ernzerhof, *Phys. Rev. Lett.* **1996**, 77, 3865.
- [90] B. Delley, *J. Chem. Phys.* **1990**, 92, 508
- [91] B. Delley, *J. Chem. Phys.* **2000**, 113, 7756.
- [92] J. Olsen, P. Jørgensen, *J. Chem. Phys.* **1985**, 82, 3235.
- [93] D. Yokoyama, H. Sasabe, Y. Furukawa, C. Adachi, J. Kido, *Adv. Funct. Mater.* **2011**, 21, 1375.
- [94] Y.-L. Chang, Z. B. Wang, M. G. Helander, J. Qiu, D. P. Puzzo, Z. H. Lu, *Org. Electron.* **2012**, 13, 925.
- [95] C. H. Fan, P. Sun, T. H. Su, C. H. Cheng, *Adv. Mater.* **2011**, 23, 2981.
- [96] C. Mayr, M. Taneda, C. Adachi, W. Brütting, *Org. Electron.* **2014**, 15, 3031.
- [97] W. Brütting, J. Frischeisen, T. D. Schmidt, B. J. Scholz, C. Mayr, *Phys. Status Solidi A* **2013**, 210, 44.
- [98] K. Aidas, C. Angeli, K. L. Bak, V. Bakken, R. Bast, L. Boman, O. Christiansen, R. Cimiraglia, S. Coriani, P. Dahle, E. K. Dalskov, U. Ekström, T. Enevoldsen, J. J. Eriksen, P. Ettenhuber, B. Fernández, L. Ferrighi, H. Fliegl, L. Frediani, K. Hald, A. Halkier, C. Hättig, H. Heiberg, T. Helgaker, A. C. Hennum, H. Hettema, E. Hjertenæs, S. Høst, I.-M. Høyvik, M. F. Iozzi, B. Jansik, H. J. Aa. Jensen, D. Jonsson, P. Jørgensen, J. Kauczor, S. Kirpekar, T. Kjærgaard, W. Klopper, S. Knecht, R. Kobayashi, H. Koch, J. Kongsted, A. Krapp, K. Kristensen, A. Ligabue, O. B. Lutnæs, J. I. Melo, K. V. Mikkelsen, R. H. Myhre, C. Neiss, C. B. Nielsen, P. Norman, J. Olsen, J. M. H. Olsen, A. Osted, M. J. Packer, F. Pawłowski, T. B. Pedersen, P. F. Provasi, S. Reine, Z. Rinkevicius, T.

A. Ruden, K. Ruud, V. Rybkin, P. Salek, C. C. M. Samson, A. Sánchez de Merás, T. Saue, S. P. A. Sauer, B. Schimmelpfennig, K. Sneskov, A. H. Steindal, K. O. Sylvester-Hvid, P. R. Taylor, A. M. Teale, E. I. Tellgren, D. P. Tew, A. J. Thorvaldsen, L. Thøgersen, O. Vahtras, M. A. Watson, D. J. D. Wilson, M. Ziolkowski, and H. Ågren, H. The Dalton quantum chemistry program system, *WIREs Comput. Mol. Sci.* **2014**, 4, 269.

[99] Dalton, a molecular electronic structure program, Release DALTON2013 (2013), see <http://daltonprogram.org>.

[100] C.-K. Moon, S.-Y. Kim, J.-H. Lee, J.-J. Kim, *Opt. Express* **2015**, 23, A279.

[101] C.-K. Moon, K.-H. Kim, J. W. Lee, J.-J. Kim, *Chem. Mater.* **2015**, 27, 2767.

[102] K.-H. Kim, J.-Y. Ma, C.-K. Moon, J.-H. Lee, J.-Y. Baek, Y.-H. Kim, J.-J. Kim, *Adv. Optical Mater.* **2015**, 3, 1191.

[103] K.-H. Kim, J.-L. Liao, S. W. Lee, B. Sim, C.-K. Moon, G.-H. Lee, H. J. Kim, Y. Chi, J.-J. Kim, *Adv. Mater.* **2016**, 28, 2526.

[104] C.-Y. Kuei, W.-L. Tsai, B. Tong, M. Jiao, W.-K. Lee, Y. Chi, C.-C. Wu, S.-H. Liu, G.-H. Lee, P.-T. Chou, *Adv. Mater.* **2016**, 28, 2795.

[105] M. J. Jurow, C. Mayr, T. D. Schmidt, T. Lampe, P. I. Djurovich, W. Brütting, M. E. Thompson, *Nat. Mater.* **2016**, 15, 85.

[106] Jaguar, version 9.1, Schrödinger, LLC, New York, NY, **2016**.

[107] A. D. Bochevarov, E. Harder, T. F. Hughes, J. R. Greenwood, D. A. Braden, D. M. Philipp, D. Rinaldo, M. D. Halls, J. Zhang, R. A. Friesner, *Int. J. Quantum Chem.*, **2013**, 113, 2110.

[108] Materials Science Suite Version 2.1, Schrodinger, LLC, New York, NY,

2016.

- [109] R. Wang, D. Liu, H. Ren, T. Zhang, H. Yin, G. Liu, J. Li, *Adv. Mater.* **2011**, 23, 2823.
- [110] H. Sirringhaus, P. J. Brown, R. H. Friend, M. M. Nielsen, K. Bechgaard, B. M. W. Langeveld-Voss, A. J. H. Spiering, R. A. J. Janssen, E. W. Meijer, P. Herwig, D. M. de Leeuw, *Nature* **1999**, 401, 685.
- [111] Y.-Y. Noh, J.-J. Kim, Y. Yoshida, K. Yase, *Adv. Mater.* **2003**, 15, 699.
- [112] T. Sakurai, R. Fukasawa, K. Saito, K. Akimoto, *Org. Electron.* **2007**, 8, 702.
- [113] P. Sullivan, T. S. Jones, A. J. Ferguson, S. Heutz, *Appl. Phys. Lett.* **2007**, 91, 233114.
- [114] H.-W. Lin, L.-Y. Lin, Y.-H. Chen, C.-W. Chen, Y.-T. Lin, S.-W. Chiu, K.-T. Wong, *Chem. Commun.* **2011**, 47, 7872.
- [115] H.-J. Kim, H.-S. Shim, J.-H. Kim, H.-H. Lee, J.-J. Kim, *Appl. Phys. Lett.* **2012**, 100, 263303.
- [116] J. W. Kim, H. J. Kim, T.-M. Kim, T. G. Kim, J.-H. Lee, J. W. Kim, J.-J. Kim, *Curr. Appl. Phys.* **2013**, 13, 7.
- [117] M. A. Loi, E. da Como, F. Dinelli, M. Murgia, R. Zamboni, F. Biscarini, M. Muccini, *Nat. Mater.* **2005**, 4, 81.
- [118] Y. Wu, P. Liu, B. S. Ong, T. Srikumar, N. Zhao, G. Botton, S. Zhu, *Appl. Phys. Lett.* **2005**, 86, 142102.
- [119] J. Kang, N. Shin, D. Y. Jang, V. M. Prabhu, D. Y. Yoon, *J. Am. Soc. Chem.* **2008**, 130, 12273.

- [120] K. Krogmann, *Angew. Chem. Int., Ed. Engl.* **1969**, 8, 35.
- [121] J. J. Novoa, G. Aullón, P. Alemany, S. Alvarez, *J. Am. Chem. Soc.* **1995**, 117, 7169.
- [122] S.-Y. Chang, J. Kavitha, S.-W. Li, C.-S. Hsu, Y. Chi, Y.-S. Yeh, P.-T. Chou, G.-H. Lee, A. J. Carty, Y.-T. Tao, C.-H. Chien, *Inorg. Chem.* **2006**, 45, 137.
- [123] L.-M. Huang, G.-M. Tu, Y. Chi, W.-Y. Hung, Y.-C. Song, M.-R. Tseng, P.-T. Chou, G.-H. Lee, K.-T. Wong, S.-H. Cheng, W.-S. Tsai, *J. Mater. Chem. C* **2013**, 1, 7582.
- [124] C.-W. Hsu, Y. Zhao, H.-H. Yeh, C.-W. Lu, C. Fan, Y. Hu, N. Roberston, G.-H. Lee, X. W. Sun, Y. Chi, *J. Mater. Chem. C* **2015**, 3, 10837.
- [125] P. Brulatti, V. Fattori, S. Muzzioli, S. Stagni, P. P. Mazzeo, D. Braga, L. Maini, S. Milita, M. Cocchi, *J. Mater. Chem. C* **2013**, 1, 1823.
- [126] S.-L. Lai, W.-Y. Tong, S. C. F. Kui, M.-Y. Chan, C.-C. Kwok, C.-M. Che, *Adv. Funct. Mater.* **2013**, 23, 5168.
- [127] X.-C. Hang, T. Fleetham, E. Turner, J. Brooks, J. Li, *Angew. Chem. Int. Ed.* **2013**, 52, 6753.
- [128] G. Li, T. Fleetham, J. Li, *Adv. Mater.* **2014**, 26, 2931.
- [129] Y. L. Chang, S. Gong, X. Wang, R. White, C. Yang, S. Wang, Z. H. Lu, *Appl. Phys. Lett.* **2014**, 104, 173303.
- [130] Q. Wang, L. W. H. Oswald, X. Yang, G. Zhou, H. Jia, Q. Qiao, Y. Chen, J. H. Halbert, B. E. Gnade, *Adv. Mater.* **2014**, 26, 8107.
- [131] A. Y. Fadeev, T. J. McCarthy, *Langmuir* **2000**, 16, 7268.
- [132] D. Janssen, R. D. Palma, S. Verlaak, P. Heremans, W. Dehaen, *Thin Solid*

Films **2006**, 515, 1433.

[133] V. M. Miskowski, V. H. Houlding, *Inorg. Chem.* **1991**, 30, 4446.

[134] S.-W. Lai, C.-M. Che, *Top. Curr. Chem.* **2004**, 241, 27.

[135] W. Lu, M.-C. Chan, N. Zhu, C.-M. Che, C. Li, Z. Hui, *J. Am. Chem. Soc.* **2004**, 126, 7639.

초 록

유기발광소자는 최근 차세대 디스플레이 및 조명으로 각광 받고 있다. 그러나 아직까지 다른 광원들에 비해 낮은 전력효율로 인해 유기발광 소자의 대중화를 위해서는 소자 효율이 더 향상되어야 한다. 최근 발광 쌍극자 배향이 무작위적일 때의 이론한계효율에 다다른 외부양자효율 29~30%인 인광 유기발광소자가 보고 되었다. 하지만 여태껏 수평으로 배향된 발광 쌍극자가 무작위적으로 배향된 발광 쌍극자 보다 높은 외부양자효율 30% 이상의 소자를 구현할 수 있음에도 불구하고 인광발광체인 이리듬 화합물의 수평배향에 대해서는 고려하지 않았다. 이는 이리듬 발광체가 정팔면체의 둥근형태를 지니고 있어서, 발광층 안에서 특정 배향을 가질 원동력이 없을 거라고 생각했기 때문이다. 최근 이리듬 발광체의 발광 쌍극자가 수평배향을 가진다는 보고가 있었지만, 이리듬 발광체의 발광 쌍극자가 특정 배향을 가지는 원인과 수평배향의 발광 쌍극자를 갖는 이리듬 발광체 설계에 대한 보고가 없었다. 뿐만 아니라 수평배향을 갖는 이리듬 발광체를 이용하여 기존 이론 한계효율인 외부양자효율 30%가 넘는 소자도 보고된 적이 없었다.

최근 전하이동 복합체의 역향간 교차를 이용하여 삼중항 여기자를 수확한 연구가 많이 보고 되었다. 분자내 전하이동 복합체인

열활성화지연형광 (TADF) 발광체는 삼중항-일중항 에너지 차이를 줄여 삼중항 여기자를 발광 가능한 단일항 여기자로 수확하여 내부양자효율 100%, 외부양자효율 30%를 달성하였다. 들뜬상태 분자간 전하이동 복합체인 엑시플렉스도 삼중항-일중항 에너지 차이가 작아서 역항간 교차를 이용하여 효율적인 삼중항 수확을 할 수 있다. 그러나 엑시플렉스 발광을 이용한 형광 유기발광소자가 단일 분자 열활성화지연형광 발광체를 이용한 형광 유기발광소자보다 낮은 효율을 보이고 엑시플렉스 발광을 이용한 형광 유기발광소자의 효율을 증가시키기 위한 방안도 보고된 적이 없다.

이 논문은 두가지 연구 주제로 구성되어 있다. (1) 형광 유기발광소자의 효율적인 삼중항 수확을 위한 엑시플렉스 동역학 분석과 (2) 인광 유기발광소자의 발광쌍극자 배향 분석으로 구성 되어있다.

2장에서는 형광 유기발광소자의 내부양자효율에 영향을 주는 엑시플렉스 동역학을 온도별 트랜지언트 광발광 측정과 전기발광 측정을 통해 정량적으로 분석하였다. 지금까지, 많은 선행 연구들은 삼중항 단일항 에너지 차이를 줄여 역항간 교차 속도를 증가시켜서 삼중항 여기자를 효율적으로 수확하는데 집중하였다. 하지만 본 연구는 발광체가 높은 비발광성 전이 속도를 가진 다면 역항간 교차 속도가 빠르더라도 삼중항 엑시플렉스를 효율적으로 수확하지 못한다는 결과를 보여준다. 효율적인 삼중항 수확을 위해서는 높은 역항간교차 속도뿐만

아니라 낮은 삼중항과 일중항의 비발광성 전이속도를 가져야 한다. 본 연구에서는 엑시플렉스 발광의 비발광성 전이 속도를 낮추기 위해 낮은 비발광성 전이 속도를 갖는 물질을 이용하고, 더 나아가서 엑시플렉스 온도를 낮추었다. 그 결과, 엑시플렉스 발광을 이용하여 외부양자효율 11%, 내부양자효율 48.3%의 형광 유기발광 소자를 구현하였고, 온도를 150 K로 낮춰 비발광성 전이를 더 억제하여 외부양자효율 25.2%, 내부양자효율 100%의 형광 유기발광 소자를 구현하였다.

열활성화지연형광과 엑시플렉스 기반의 형광 유기발광소자는 기존 형광 유기발광소자보다 넓은 발광 스펙트럼과 낮은 소자 안정성을 갖는 단점이 있다. 3장에서는 엑시플렉스를 지연형광 특성이 없는 기존 형광 도펀트의 호스트로 사용하여 기존 형광 발광체의 삼중항을 수확하였다. 역항간 교차로 수확된 삼중항 엑시플렉스가 Förster 에너지 전이를 통해 엑시플렉스 호스트로부터 기존 형광 도펀트로 전달 될 수 있다. 그 결과, 기존 형광 발광체를 이용하여 외부양자효율 10.6%의 고효율 형광 유기발광소자를 구현하였고, 엑시플렉스를 호스트로 사용하였을 때 발광가능한 여기자 비율이 35% 이상으로 해당 시스템이 10% 이상의 삼중항을 수확하였다.

4-8장에서는 고효율 인광 유기발광소자를 위한 발광쌍극자 배향에 대해 연구하였다. 인광 발광쌍극자의 수평배향의 원인, 인광발광체의 분자구조와 발광 쌍극자 배향의 관계에 대해서 분석하고,

수평배향된 발광쌍극자를 이용하여 세계 최고효율의 인광 유기발광소자를 구현하였다. 이리듬 복합체의 발광 쌍극자 배향은 보조리간드 구조 (4장) 뿐만 아니라 주리간드 구조 (5장) 에 크게 영향을 받는다. 동종리간드 이리듬 화합물은 무작위적인 발광쌍극자를 갖는 반면 이종리간드 이리듬 화합물은 정팔면체의 등근구조를 가지고 있음에도 불구하고 특정 배향의 발광 쌍극자를 갖는다. 비정질 호스트층 안에서 이종리간드 이리듬 화합물의 특정 발광 쌍극자 배향은 이종리간드 이리듬 화합물이 특정방향의 전이쌍극자 모멘트와 호스트와 이리듬 화합물간의 강한 결합에너지로부터 기인한다. 이종리간드 이리듬 화합물의 C₂축이 기판에 대해서 어느정도 분포를 가지면서 수직하게 서있고 이종리간드 이리듬 화합물의 삼중항 전이쌍극자 모멘트 방향이 이리듬으로부터 질소 이중원자고리로 향하고 있어서, 이종리간드 이리듬 화합물의 발광쌍극자가 비정질 발광층안에서 수평배향을 하게 된다. 더 나아가서 수평배향된 이종리간드 이리듬 화합물을 이용하여 기존 이론한계효율 30%가 넘는 외부양자효율 35.6%의 적색발광소자, 32.3%의 녹색발광소자를 구현하였다.

이러한 발견을 기반으로, 이종리간드 이리듬 화합물의 주리간드를 치환하여 높은 발광 쌍극자 수평배향을 (θ) 을 갖는 새로운 이종리간드 이리듬 화합물을 설계하고 합성하였다. 새로운 이리듬 화합물 설계 전략은 치환기를 이용하여 (1) 이종리간드 이리듬 화합물의 삼중항 발광

쌍극자 모멘트 방향을 C₂축과 수직한 방향으로 향하게 하며 (6장) (2) 발광체 내에서 2가지 상태로 축퇴된 발광 쌍극자 모멘트가 기판에 대해 평행하게 배열한다 (7장). 먼저 삼중항 발광쌍극자 모멘트 방향을 조절하기 위해서 메틸 치환기를 이종리간드 이리듐 화합물의 주리간드에 체계적으로 치환하였다. 메틸치환기는 치환된 위치에 따라 다른 발광쌍극자 모멘트 방향을 가졌고, C₂축과 발광쌍극자 모멘트사이의 각도 (Φ) 가 클수록 발광체의 Θ 가 커지는 상관관계를 발견하였다. 그 결과 메틸 치환기가 없는 발광체 보다 Θ 가 6% 향상된 80%의 Θ 를 갖는 새로운 인광발광체를 개발하였고, 이를 이용하여 외부양자효율 34%의 녹색 인광 유기발광소자를 구현하였다.

7장에서는 다양한 기능을 가지는 치환기를 이종리간드 이리듐 화합물의 피리딘 고리 4번 자리에 치환하여 발광층 안에서 발광체의 분자 배향을 조절함으로써 Θ 를 향상시켰다. 이종리간드 이리듐 화합물의 비대칭성이 증가하거나 호스트와 이리듐 발광체의 공액 전자들 간의 강한인력이 존재하면 이리듐-질소 결합과 발광체의 발광 쌍극자 방향이 기판에 대해 수평하게 배열 된다. 새롭게 설계된 이리듐 화합물은 기준 발광체보다 1 ~ 7.5% 향상된 80 ~ 86.5%의 Θ 를 보였다. 그 결과 외부양자효율 38%의 노란색 유기발광소자, 36%의 녹색 유기발광소자를 구현하였고, 이리듐 복합체를 이용한 인광 유기발광소자 중 세계 최고효율을 달성하였다.

비정질 발광층은 액정처럼 배향적 배열을 가질 수 있지만 분자의 배향이 완벽하게 배열되지 못하고 평균 배향을 기준으로 어느정도의 분포를 가지고 있다. 그래서 비정질 박막의 Θ 를 향상시키기 쉽지 않은 실정이다. 이러한 측면에서 위치적, 배향적 배열이 있는 유기결정이 높은 Θ 를 구현하기에 더 적합한 발광체이다. 그러나 유기 결정은 농도소광 효과로 인한 낮은 발광 효율과 거친 표면으로 인한 낮은 소자 안정성으로 인해 유기발광소자에 거의 사용되지 않는다. 8장에서는 완벽하게 배향된 백금 화합물을 이용한 결정질 발광층을 이용하여 93%의 높은 Θ 와 외부양자효율 39%의 세계최고효율의 유기발광소자를 구현하였다. X선 회절 분석과 양자계산을 이용하여 백금 화합물 박막의 결정 특성과 발광 쌍극자 배향의 관계를 규명하였다. 결정질 발광층의 발광 쌍극자 배향은 발광층의 결정도뿐만 아니라 결정 안에서 분자배열의 영향을 받는다. 결정 안에서의 분자배열은 백금화합물의 CF_3 치환기 위치와 대칭성에 의해 결정된다.

주요어: 유기발광소자, 엑시플렉스, 지연형광, 삼중항 수확, 발광 쌍극자 배향, 결정질 발광층, 이리듐 화합물, 백금 화합물

학번: 2011-20621